

Wearable Sweat Sensors for Disease Monitoring and Management

Thesis by
Jiaobing Tu

In Partial Fulfillment of the Requirements for the
Degree of
Doctor of Philosophy

The logo for the California Institute of Technology (Caltech), featuring the word "Caltech" in a bold, orange, sans-serif font.

CALIFORNIA INSTITUTE OF TECHNOLOGY
Pasadena, California

2024
(Defended October 27, 2023)

© 2023

Jiaobing Tu

ORCID: 0000-0002-7653-6640

ACKNOWLEDGEMENTS

I would like to express my deepest gratitude and appreciation to all those who have contributed to the completion of this thesis. This journey would not have been possible without the support, guidance, and encouragement of many individuals and organizations.

First and foremost, I am immensely thankful to my thesis advisor, Wei Gao, for his unwavering support, invaluable mentorship, and boundless patience throughout this research endeavor. His expertise and dedication have been instrumental in shaping the direction of this work.

I would like to extend my heartfelt gratitude to the members of my thesis committee, Prof. Mikhail Shapiro, Prof. Azita Emami, and Prof. John Dabiri for their constructive feedback, insightful suggestions, and for dedicating their time to the evaluation of this research.

I owe a debt of gratitude to my family for their unending love and encouragement. Their belief in my abilities and their constant support provided me with the strength to persevere through the challenges of this academic journey.

My sincere thanks go to my friends and colleagues who offered both academic and emotional support, making this journey more enjoyable and less daunting.

I would also like to acknowledge the invaluable resources and facilities provided by Caltech which were crucial for conducting this research. I extend my appreciation to the participants of this study, without whom this research would not have been possible. Their willingness to share their time and experiences contributed significantly to the quality of this work.

Lastly, I would like to acknowledge the financial support (NSS-PhD) provided by A*STA Graduate Academy.

ABSTRACT

With the emphasis of healthcare shifting towards prevention and early detection of diseases and monitoring of chronic conditions, there is a growing need for hassle-free telemedicine sensor technologies that can be seamlessly integrated into daily life. While significant progress has been made in the development of wearable sweat and salivary biosensors to meet this need for rapid, real-time collection of physiological information, the majority of current epidermal sensing systems are unable to detect trace-level disease-relevant biomarkers accurately in biofluids and cannot be mass produced. To meet this demand for low-cost, mass-producible mHealth devices for at-home settings, we developed several fully integrated laser-engraved graphene-based biosensors for the detection of low-concentration sweat and saliva analytes including hormones (cortisol) and proteins (C-reactive protein). Several graphene surface engineering strategies are investigated for the sensitive and selective detection of targets. System-level engineering and microfluidic designs are explored to achieve on-demand sweat induction and harvesting under sedentary settings and automated sweat and reagent routing and in situ signal correction and analysis for facile operation on the skin. The utility of these fully integrated flexible mHealth systems is evaluated through multiple human studies involving healthy and various patient subgroups towards stress assessment, as well as the monitoring and management of various chronic conditions including chronic obstructive pulmonary disease, heart failure, and inflammatory bowel diseases. These fully integrated mHealth devices demonstrate a technology that can be easily adapted to monitor a broad spectrum of disease-specific proteins, cytokines, and hormones, thus advancing future applications in personalized disease diagnosis, management, and prevention.

PUBLISHED CONTENT AND CONTRIBUTIONS

1. Tu, J., Min, J., Song, Y., Xu, C., Li, J., Moore, J., Hansan, J., Hu, E., Primon, T., Wang, T., Davoodi, E., Chou, T., Chen, P., Hsu, J., Rossiter, H., & Gao, W. A wireless patch for the monitoring of C-reactive protein in sweat. *Nature Biomedical Engineering* 7, 1293–1306 (2023) doi: 10.1038/s41551-023-01059-5

W.G. and J.T. initiated the concept and designed the overall studies. W.G. supervised the work. J.T., J. Min and Y.S. led the experiments and collected the overall data. C.X., J.L., T.-Y.W., E.D. and T.-F.C. contributed to sensor characterization and validation. J. Moore, J.H., E.H., T.P., P.C., J.J.H. and H.B.R. contributed to the design of the human trials and to the system's evaluation in the participants. All authors contributed to data analysis and provided feedback on the paper.

2. Min, J.; Tu, J.; Xu, C.; Lukas, H.; Shin, S.; Yang, Y.; Solomon, S.; Mukasa, D.; Gao, W. Skin-interfaced wearable sweat sensors for precision medicine. *Chemical Reviews* 123, 5049-5138 (2023) doi: 10.1021/acs.chemrev.2c00823

All authors prepared the figures and the manuscript.

3. Tu, J., & Gao, W. Ethical considerations of wearable technologies in human research. *Advanced Healthcare Materials* 10, 2100127 (2021) doi:10.1002/adhm.202100127

J.T. and W.G. prepared the manuscript and the figures.

4. Torrente-Rodríguez R. M.; Tu, J.; Yang, Y.; Min, J.; Wang, M.; Song, Y.; Yu, Y.; Xu, C.; Ye, C.; IsHak, W. W.; Gao, W. Investigation of cortisol dynamics in human sweat using a graphene-based wireless mHealth system. *Matter* 2, 927-937 (2020) doi:10.1016/j.matt.2020.01.021

W.G., R.M.T.-R., and J.T. initiated the concept; W.G., R.M.T.-R., J.T., and W.W.I. designed the experiments; R.M.T.-R. and J.T. led the experiments and collected the overall data; Y.Y. performed electrode fabrication and characterization; J.M. performed the circuit design and test; C.X., C.Y., M.W., Y.S., and Y.Y. contributed to sensor characterization; W.G., R.M.T.-R., and J.T. contributed the data analysis and co-wrote the paper. All authors provided feedback on the manuscript.

5. Tu, J.; Torrente-Rodríguez, R. M.; Wang, M; Gao, W. The era of digital health: A review of portable and wearable affinity biosensors. *Advanced Functional Materials* 30, 1906713 (2019) doi:1002/adfm.201906713

All authors prepared the figures and the manuscript.

TABLE OF CONTENTS

Acknowledgements.....	iii
Abstract	iv
Published Content and Contributions.....	v
Table of Contents.....	vi
List of Illustrations and/or Tables.....	viii
Abbreviations.....	xiv
Chapter 1: Introduction.....	1
1.1 Wearable Sweat Sensors	2
1.2 Bioaffinity Sensors	3
1.2.1 Antibody-based Sensors.....	6
1.2.2 Nucleic Acid-based Sensors.....	9
1.2.3 MIP-based Sensors	11
1.2.2 Bioaffinity Sensor Design Considerations	13
Bibliography of Chapter 1.....	14
Chapter 2: A mHealth Sensor for Stress Monitoring	19
2.1 Introduction	20
2.2 Laser-Engraved Graphene-Based Cortisol Sensor	23
2.2.1 Materials and Methodology	23
2.2.2 Results and Discussion.....	25
2.3 System Engineering of GS ₄	35
2.3.1 Materials and Methodology	35
2.3.2 Results and Discussion.....	36
2.4 Investigation of The Circadian Rhythm And Stress Responses of Sweat Cortisol.....	41
2.4.1 Materials and Methodology	41
2.4.2 Results and Discussion.....	43
2.5 Conclusion.....	51
Bibliography of Chapter 2.....	52
Chapter 3: A Wearable Sweat Sensor for Systemic Inflammation Monitoring	59
3.1 Introduction	60
3.2 Design of The Wearable Microfluidic LEG-AuNPs Biosensor	62
3.2.1 Materials and Methodology	63
3.3. LEG-AuNPs Immunosensor for CRP Detection.....	65
3.3.1 Materials and Methodology	65
3.3.2 Results and Discussion.....	68
3.4 Evaluation of Sweat CRP For Non-Invasive Monitoring Of Systemic Inflammation.....	71
3.4.1 Materials and Methodology	71
3.4.2 Results and Discussion.....	74

3.5 Characterization of the Multiplexed Microfluidic Patch for Automatic Immunosensing	77
3.5.1 Materials and Methodology	77
3.5.2 Results and Discussion.....	78
3.6 System Integration and On-Body Evaluation of The Wearable Biosensor	81
3.7 Conclusion.....	84
Bibliography of Chapter 3.....	85
Appendix A.....	90
Bibliography of Appendix A.....	129
Chapter 4: Discussion and Outlook.....	130
4.1 Continuous Epidermal Sensing.....	132
4.2 Ethical Considerations of Wearable Technologies in Human Research.....	134
4.3 Conclusion and Outlook.....	145
Bibliography of Chapter 4	147

LIST OF ILLUSTRATIONS AND TABLES

<i>Figure Number</i>	<i>Page</i>
1-1. Major components of a bioaffinity sensor.....	6
2-1. An integrated wireless graphene-based sweat stress sensing system (GS4) for dynamic and non-invasive stress hormone analysis.....	22
2-2. Schematic of modification procedure of the graphene electrode for cortisol sensing.....	29
2-3. Schematic of the electrochemical detection of cortisol in human sweat.....	29
2-4. Scanning electron microscopy (SEM) images of the graphene electrode surface before and after PPA polymerization.....	30
2-5. Raman spectra of bare graphene electrode, and graphene electrodes modified with PPA (pPPA) and capture antibody (CAb).....	30
2-6. X-ray photoelectron spectra (XPS) of bare graphene electrode, and graphene electrodes modified with PPA (pPPA) and capture antibody (CAb).....	31
2-7. Nyquist plots of a graphene electrode in a 0.01 M PBS solution containing 2.0 mM of K ₄ Fe(CN) ₆ /K ₃ Fe(CN) ₆ (1:1) after each surface modification step.....	31
2-8. Characterization of the graphene sensor.....	31
2-9. Electrochemical cortisol sensor optimization.....	32
2-10. Amperometric signals of the flexible graphene-based biosensors for 0.0–10.0 ng/mL cortisol in 0.01 M PBST, pH 7.4.....	32
2-11. Sensor performance of laser-induced graphene electrode (LGE) vs. screen printed carbon electrode (SPCEs) and glassy carbon electrodes (GCEs).	33

2-12.	Full sigmoidal calibration curves constructed for cortisol in buffer, sweat and saliva.....	33
2-13.	Performance characterization of the graphene-based electrochemical sensors.	33
2-14.	Nyquist plots of a graphene electrode in a 0.01 M PBS solution containing 2.0 mM of K ₄ Fe(CN) ₆ /K ₃ Fe(CN) ₆ (1:1) after each surface modification step..	34
2-15.	Validation of the flexible graphene-based biosensors toward cortisol monitoring in real samples with enzyme-linked immunosorbent assay (ELISA).....	34
2-16.	Stability test of the graphene-based electrochemical sensors.	35
2-17.	Optimization of platform design. 3-channel amperometric signals obtained with two platform designs in 1,000,000X diluted HRP-cortisol, 2.0 mM HQ and 1.0 mM H ₂ O ₂ in 50 mM phosphate buffer (pH 6.0).	37
2-18.	Design of the flexible microfluidic three-working electrode (3WE) sensor array for cortisol detection and photograph of the printed circuit board (PCB) with the graphene sensor patch for signal processing and wireless communication.	38
2-19.	Block diagram of the GS ⁴	38
2-20.	Sensor readings obtained wirelessly with the GS ⁴	39
2-21.	Comparison of average signals and standard deviations obtained with 1, 2, and 3 working electrodes.....	39
2-22.	Proportional error evaluated for the GS ⁴ based on real sample recovery studies.	40
2-23.	The flexible microfluidic graphene sensor array on the skin and under mechanical deformations.	40
2-24.	The responses of the sensor arrays with cortisol recognition under mechanical deformation (with radii of bending curvatures of 2.3 and 3.8 cm in 1.0, 5.0, and 10.0 ng/mL cortisol).	41

2-25.	Thermal image of the sensor patch on human forearm	41
2-26.	Influence of temperature on sensor performance.....	42
2-27.	Conceptual illustration of the light/dark-cycle regulated cortisol circadian rhythm and the transport of circulating cortisol to sweat	46
2-28.	Iontophoresis based sweat sampling.....	47
2-29.	.Circadian rhythm of sweat cortisol constructed for a healthy subject in a period of 6 days.	47
2-30.	Cortisol levels found in serum, saliva and sweat sampled in the AM and in the PM from four healthy subjects	48
2-31.	Correlation of serum cortisol to sweat cortisol.....	48
2-32.	Correlation of salivary cortisol to sweat cortisol.....	49
2-33.	Dynamic monitoring of exercise stress response using the GS4	49
2-34.	Figure 2-34. Influence of time of exercise in cortisol variation.....	50
2-35.	Dynamic monitoring of acute stress response to cold pressor test using the GS4	50
2-36.	Salivary cortisol at several time points across the cold pressor test for four subjects (C1-C4) from the human study presented in Fig. 2-35 ..	51
3-1.	Wearable electrochemical nanobiosensor for automatic, non-invasive, and wireless inflammation monitoring.	61
3-2.	Materials and electrochemical characterizations of the LEG-AuNPs CRP sensor	70
3-3.	Evaluation of sweat CRP for non-invasive monitoring of systemic inflammation in healthy and patient populations.....	76
3-4.	Multiplexed microfluidic patch for automatic immunosensing.....	80
3-5.	On-body evaluation of the multiplexed wearable patch toward non-invasive automatic inflammation monitoring	80
A-1.	Fabrication process of the microfluidic multimodal sensor patch	91
A-2.	SEM images of the LEG electrodes.....	91
A-3.	The integrated wireless wearable electronics for CRP sensing.	92

A-4.	Surface functionalization process of the LEG-AuNPs working electrode of the CRP sensor.	92
A-5.	Influence of the self-assembled monolayer (SAM) modification on electrode performance.	92
A-6.	Electrochemical performance of the LEG CRP sensors prepared by different functionalization methods	93
A-7.	Characterization of the CRP sensor functionalization using XPS	93
A-8.	Electrochemical impedance spectroscopy (EIS) for the LEG-AuNPs CRP sensor after each surface modification step.	94
A-9.	Batch to batch variations in electrochemical performance of the LEG electrodes and LEG-AuNPs electrodes.....	95
A-10.	Conjugation process of the dAb-conjugated AuNPs complex for signal amplification.	96
A-11.	Comparison of the electrochemical performances of redox probe conjugated dAb and dAb-conjugated AuNPs.....	97
A-12.	UV-Vis absorbance of the dAb-AuNP conjugate after each modification step.....	98
A-13.	The reproducibility of the CRP sensor.	99
A-14.	Selectivity of the CRP sensor to potential interferences in sweat	100
A-15.	The influence of incubation pH, time, temperature, sample volume, and detection ionic strength on the CRP sensor responses.	101
A-16.	SWV voltammograms of the CRP sensors in CRP solutions with varying Cl ⁻ concentrations.	102
A-17.	The stability of the CRP sensor	103
A-18.	Representative mass spectra of CRP derived peptides and chromatograms.	103
A-19.	CRP levels in serum, sweat, saliva, and urine.....	104
A-20.	Box-and-whisker plot of sweat electrolyte and pH levels between iontophoresis and exercise sweat.	104
A-21.	The influence of electrolyte concentration and pH on the antigen	

	capturing measured with ELISA.	105
A-22.	Sweat rate of current and former smokers with and without COPD after 5 minutes of iontophoretic sweat induction.	106
A-23.	Influence of the high flow rates on microfluidic automatic CRP sensing.	107
A-24.	Influence of the interferent molecules on microfluidic automatic CRP sensing.	108
A-25.	Flow test characterization of the multimodal sensor patch in response to different initial pHs.	109
A-26.	Detailed circuit schematic of the InflaStat.	110
A-27.	LEG-based sensor calibration plots obtained with the InflaStat CRP sensing.	111
A-28.	Performance of the CRP, pH, and temperature sensors under mechanical deformation.	112
A-29.	On-body evaluation of the wearable sensor on healthy never smokers.	113
A-30.	On-body evaluation of the wearable sensor on healthy smokers.	114
A-31.	On-body evaluation of the wearable sensor on post-COVID subjects	115
A-32.	Time-lapse images showing the automatic microfluidic reagent routing and washing.	116
A-33.	Influence of solution pH in peak potential and current of the redox molecule thionine.	117
A-34.	Influence of the pH, ionic strength, and temperature on the CRP sensor reading.	118
A-35.	Box-and-whisker plot of CRP levels in sweat and serum samples from post-COVID subjects with mild and moderate symptoms.	119
A-36.	Evaluation of system reproducibility via dynamic monitoring of sweat and blood CRP.	120
A-37.	Evaluation of sweat CRP levels across anatomic locations.	121
4-1.	Ethical considerations and challenges of using new wearable	

	technologies in human research..	137
<i>Table Number</i>		<i>Page</i>
A-1.	Commercial CRP kits and laboratory tests that can perform ng-level CRP detection.....	121
A-2.	Commercial point-of-care CRP monitors.	122
A-3.	Inclusion list of precursor ions used for targeted CRP protein	123
A-4.	Patient information for the COPD study	124
A-5.	Patient information for the heart failure study.....	125
A-6.	Patient information for the active infection study.	126
A-7.	The currently reported microfluidic wearable sweat sensors.....	126
A-8.	Patient information for the post-COVID-19 infection study.	127
4-1.	Key Characteristics of an ideal wearable bioaffinity sensor.....	148

ABBREVIATIONS

POC - Point-of-Care
mHealth - Mobile Health
BGM - Blood Glucose Monitoring
CGM - Continuous Glucose Monitoring
EIS - Electrochemical Impedance Spectroscopy
FET - Field Effect Transistor
SPR - Surface Plasmon Resonance
CV - Cyclic Voltammetry
LC - Lateral Flow Assay
ECL - Electrochemiluminescence
MIP - Molecularly Imprinted Polymer
AuNPs - Gold Nanoparticles
CNT - Carbon Nanotubes
AuNT - Gold Nanotubes
PVA - Polyvinyl Alcohol
OEET - Organic Electrochemical Transistor
MSM - Molecularly Selective Membrane
TENG - Triboelectric Sensor
PVDF - Polyvinylidene Fluoride
PTSD - Posttraumatic Stress Disorder
MDD - Major Depressive Disorder
HPA - Hypothalamic-Pituitary-Adrenal
CVD - Cardiovascular Diseases
ESM - Experience Sampling Methods
GS4 - Graphene-based Sweat Stress Sensing System
PI - Polyimide
PPA - Pyrrole Propionic Acid
EDC - 1-Ethyl-3-(3-Dimethylamoniopropyl)carbodiimide
Sulfo-NHS - N-Hydroxysulfosuccinimide
BSA - Bovine Serum Albumin
HQ - Hydroquinone

MES - 2-(N-Morpholino)ethanesulfonic Acid
CV - Cyclic Voltammetry
TEM - Transmission Electron Microscopy
SEM - Scanning Electron Microscopy
XPS - X-ray Photoelectron Spectroscopy
OCP-EIS - Open Circuit Potential-Electrochemical Impedance Spectroscopy
DPV - Differential Pulse Voltammetry
LGEs - Laser-Induced Graphene Electrodes
GCEs - Glassy Carbon Electrodes
SPCEs - Screen-Printed Carbon Electrodes
TMB - 3,3',5,5'-Tetramethylbenzidine
LOD - Limit of Detection
ELISA - Enzyme-Linked Immunosorbent Assay
PCB - Printed Circuit Board
MCU - Microcontroller Unit
ADC - Analog-to-Digital Converter
DAC - Digital-to-Analog Converter
RE - Reference Electrode
CE - Counter Electrode
LPF - Low Pass Filter
BLE - Bluetooth Low Energy
HRP - Horseradish Peroxidase
SD - Standard Deviation
IRB - Institutional Review Board
HPA - Hypothalamic-Pituitary-Adrenal axis
CPT - Cold Pressor Test
CRP - C-reactive protein
InflaStat - Name of the wearable nanobiosensor
LEG - Laser-Engraved Graphene
TH - Thionine
dAb - Detector Antibody
HF - Heart Failure

CO₂ - Carbon Dioxide

FPCB - Flexible Printed Circuit Board

IP - Iontophoresis UV-Vis - Ultraviolet-visible Spectroscopy

DPV - Differential Pulse Voltammetry

EIS - Electrochemical Impedance Spectroscopy

TEM - Transmission Electron Microscopy

DLS - Dynamic Light Scattering

SWV - Square Wave Voltammetry

ELISA - Enzyme-Linked Immunosorbent Assay

Chapter 1

INTRODUCTION

Materials from this chapter appear in “Tu, J.; Torrente-Rodríguez, R. M.; Wang, M; Gao, W. The era of digital health: A review of portable and wearable affinity biosensors. *Advanced Functional Materials* 30, 1906713 (2019) doi:1002/adfm.201906713” and “Min, J.; Tu, J.; Xu, C.; Lukas, H.; Shin, S.; Yang, Y.; Solomon, S.; Mukasa, D.; Gao, W. Skin-interfaced wearable sweat sensors for precision medicine. *Chemical Reviews* 123, 5049-5138 (2023) doi: 10.1021/acs.chemrev.2c00823.”

1.1 Wearable Sweat Sensors

The evolution of point-of-care (POC) testing biosensors has ushered in a new era in the realm of health management, promising the potential to revolutionize the way we monitor health, diagnose diseases rapidly, and make precise predictions^{1,2}. This transformation has been driven by the creative integration of sensor technologies with mobile devices, giving rise to a field known as digital health or mobile health (mHealth). In the ever-expanding landscape of healthcare, mHealth offers opportunities to enhance at-home diagnosis, patient management, and communication between healthcare providers and patients. Propelled by advancements in sensor technologies and big data analytics, the future of digital health envisions the creation of a learning health system that not only reshapes the paradigm of disease management but also holds the potential to transform clinical treatment³. Long-term health monitoring, enabled by smartphones and wearable technologies operating at both micro and macro scales, can promote healthy lifestyles, reduce health-related problems, facilitate patient-centric management of chronic conditions, decrease the frequency of clinical visits, and deliver personalized, on-demand interventions at the point of care.⁴

As the healthcare industry pivots toward a focus on disease prevention, early detection, and continuous monitoring of chronic conditions, there is a growing demand for patient-centered sensor technologies that are both seamless and hassle-free.⁵ Portable devices have already demonstrated their value in various disease diagnosis and monitoring scenarios, with classic examples including commercial blood glucose monitoring (BGM) and colorimetric pregnancy test devices. On the other hand, wearable biosensors, equipped with the ability to provide continuous monitoring, have evolved from tracking generic physical biomarkers, such as temperature^{6,7} and pressure⁸, to more disease-specific applications, like diabetes management⁹. Devices like the Apple Watch and Fitbit, designed for tracking physical activity, have become increasingly prevalent among the general public. Additionally, the market has witnessed the emergence of various continuous glucose monitoring (CGM) devices, such as the Guardian® REAL-Time by Medtronic and the FreeStyle® Libre by Abbott.

Current state-of-the-art commercialized wearable devices primarily focus on monitoring biophysical signals (temperature, heart rate) that indicate the physical manifestations of an

underlying health state or condition which constrain the application of these devices within well-being services. Owing to the complexity and multidimensional nature of various diseases, deeper, multiplexed information acquired at the molecular level is needed before wearable sensors can be adopted for disease monitoring. From smart watches to e-skins, innovations in wearable sweat sensors promise to address this technological gap by expanding the biometrics accessible non-invasively through the skin.

Sweat contains a wealth of biochemical information that can be noninvasively and readily accessed on-demand or even continuously.¹⁰⁻¹² Compared with the complexities and discomforts associated with the sampling of other biofluids like blood, interstitial fluid, tear, saliva, and urine, sweat sampling can be conveniently and unobtrusively achieved by placing a sensor patch on accessible locations of the skin. Molecular biomarkers unveiled by wearable sweat sensors through continuous and non-invasive monitoring can provide a more detailed understanding of the biochemical processes that govern our health, enabling precision medicine through personalized monitoring of an individual's fitness and health conditions, as well as disease diagnosis and prognosis. Furthermore, the large amounts of biochemical profiles collected by sweat sensors from patients and healthy populations during daily activities can be processed through predictive algorithms to realize personalized therapeutics and preventative care. At the same time, large datasets collected at the population level can improve real-time epidemiological surveillance and enhance the precision of public health responses.

Given the low concentrations of disease-relevant biomarkers in sweat (nM or lower), the performance of ion-selective and enzymatic sensors may be limited in interrogating trace-level targets like hormones and proteins. In this regard, the design of ultra-sensitive bioaffinity sensors which are specific to various disease biomarkers is a cornerstone of the development of wearable sweat biosensors for non-invasive health and disease monitoring.

1.2 Bioaffinity Sensors

Bioaffinity sensors typically consist of a bioreceptor layer for specific molecule recognition and a signal transducer which converts the recognition event between a target and a receptor into a measurable signal (**Fig. 1-1**).

The journey of bioaffinity sensors from their conception, as exemplified by the surface plasmon resonance (SPR) detection of biospecific interactions^{13,14}, is marked by a transformation from complex and bulky laboratory-based equipment to miniaturized, portable systems that cater to decentralized or at-home analysis of disease biomarkers. While portable bioaffinity sensing technologies have made significant strides in recent decades, marked by advancements in biological sample processing, rapid analysis in miniaturized fluidic devices, and smartphone-enabled data extraction¹⁵, technologies specific to wearable bioaffinity sensing platforms did not come to the forefront until the 2010s. Nonetheless, many engineering principles originally devised for point-of-care disease management and continuous wearable sensing are readily adaptable for the incorporation of bioaffinity elements.

General classes of receptors employed for wearable sweat biosensor construction include antibodies, receptor proteins, nucleic acids, and biomimetic materials like molecularly imprinted polymers (MIP). Selective binding of functional groups such as the polyol-boronic acid pair has also been explored in the construction of affinity-based sweat sensors. The intrinsic properties of the bioreceptors, in essence, determine several operational characteristics of a biosensor, including selectivity, sensitivity, stability, and reversibility.

On the other hand, the architecture and design of transduction interfaces govern the physical characteristics (size, portability, type of instrumentation), costs, as well as the limit of detection for the target. In recent years, affinity-based formats have been coupled with various types of transducer interfaces such as electrochemical, optical, and piezoelectric sensors. Electrochemical sensors are versatile tools that can be easily integrated with epidermal systems with high innate sensitivity, scalability, and low instrumentation costs. Electrochemical impedance spectroscopy (EIS) probes the impedance of an electrode-solution interface by applying a small amplitude (typically 5-10 mV peak-to-peak) sinusoidal perturbation while registering the current response. In non-faradaic EIS, the binding event between biomarkers and receptors immobilized on the transducer interface leads to a change in the double-layer capacitance (C_{dl}) in the Randles circuit and consequently the impedance (Z) of the system due to the dielectric properties of the biomarkers based on the Gouy-Chapman-Stern model. In contrast, faradaic EIS requires the presence of redox-active species. The association of biomarkers presents an electrostatic and/or steric barrier to the

redox probes at the interface and modulates the charge transfer resistance (R_{ct}) and the impedance of the system. Other techniques that monitor the faradaic response of targets with direct electrochemical properties or the faradaic response of electrochemical tracers include amperometry and voltammetry (square wave voltammetry, differential pulse voltammetry, and cyclic voltammetry). Bioreceptors, especially aptamers, have also been integrated with various field effect transistors (FET) on the skin. The modulation of charge distribution at the semiconducting interface (gate electrodes) upon target binding translates into a measurable change in the current that flows between the source and drain electrodes. Surface-charged species distribution and electrolyte concentration in the detection media play an important role in the transduction mechanisms of most electrochemical sensors. Unlike conventional biofluids like serum and saliva, sweat electrolyte and pH content vary hugely with different subjects and different collection methods. Therefore, the influence of such variations should be carefully addressed in the design and implementation of electrochemical sensors for *in situ* sweat analysis.

Optical transduction mechanisms can be further categorized into colorimetry, fluorescence, chemiluminescence, and plasmonic. The simplest format of colorimetric bioaffinity sensor used for wearable sweat analysis is lateral flow assay. The association of biomarkers with bioreceptor-immobilized metal nanoparticles leads to a visible change in the absorbance wavelength and/or intensity due to the aggregation or accumulation of nanoparticles within the test zone. Plasmonic affinity sensors require the excitation of noble metal films or nanoparticles with an incident laser and measure the change of surface plasmon resonance (SPR) or the modulation of Raman scattering (SERS) from the interface in response to target binding. Smartphone-enabled wearable sensing and signal processing technologies are less influenced by the electrolyte content of sweat samples as compared with electrochemical biosensors; however, these technologies need to account for variations in ambient lighting. The size and portability of optical systems are not comparable with integrated electrochemical systems.

Often, many targets of interest do not possess optical or electrochemical properties that can be directly detected by a transducer. As a result, the addition of a signaling tracer that either competes with the analyte (competitive format) or binds to a secondary binding site on the target where a target is ‘sandwiched’ between a surface-immobilized receptor and receptor-based tracer

(sandwich format) is necessary to produce a measurable signal. Enzymatic tracers are sometimes incorporated in a sensing format to amplify the signals of a system and achieve a lower detection limit. As some formats are complex and multistep, epidermal microfluidic modules that can be programmed to manipulate reagents may be necessary to achieve miniaturization and automation. Together, the features of bioreceptors, transducers, and sensing formats determine the operational characteristics of a wearable sweat biosensor.

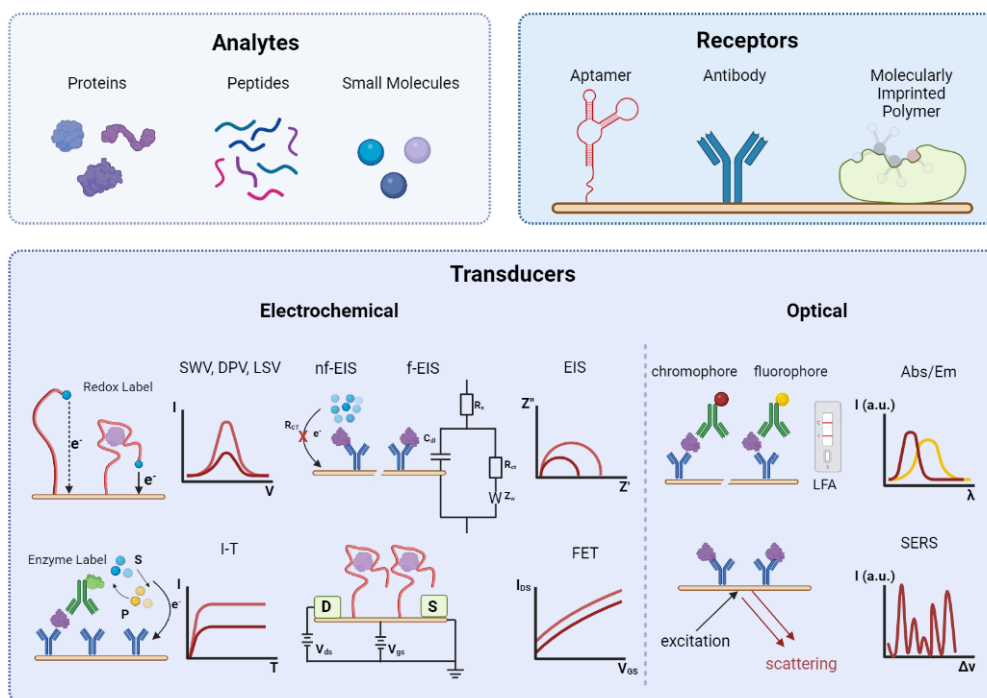


Figure 1-1. Major components of a bioaffinity sensor. Bioaffinity detects analytes including proteins, nucleic acids and small molecules. A bioaffinity sensor recognizes an analyte via affinity interactions with a receptor (aptamer, antibody or molecularly imprinted polymer) and converts the interactions into measurable signals via a transducer. Transducers employed for epidermal sweat sensing are either electrochemical or optical. SWV, square wave voltammetry; DPV, differential pulse voltammetry; LSV, linear sweep voltammetry; I , current; V , potential; R_{CT} , charge transfer resistance; C_{dl} , double layer capacitance; R_s , solution resistance; Z_w , Warburg element; Z' , real impedance; Z'' , imaginary impedance; nf-EIS, non-faradaic electrochemical impedance spectroscopy. f-EIS, faradaic impedance spectroscopy; S, substrate; P, product; I-T, chronoamperometry; D, drain; S, source; V_{ds} , drain-source voltage; V_{gs} , gate-source voltage; FET,

field effect transistor; Abs, absorbance; Em, emission; I (a.u.), intensity; λ , wavelength; LFA, lateral flow assay; $\Delta\nu$, Raman shift. Created with BioRender.com.

1.2.1 Antibody-based sensors

Antibodies are the most widely used bioreceptors in bioaffinity sensors due to their superior affinity and specificity to targets, versatility, and commercial availability. Depending on whether an electrochemical or optical tracer is used, antibody-based sensors are classified into labeled (with tracers) and label-free immunosensors. In label-free immunosensors, the association of an antigen with an antibody is directly transduced into electrical or optical signals. Non-faradaic EIS is the most commonly used technique in constructing label-free sweat immunosensors. A non-faradaic EIS sensor was developed for ethyl glucuronide, a metabolite of ethanol, in spiked human sweat¹⁶. Impedance across two co-planar gold or zinc oxide (ZnO) electrodes functionalized with monoclonal anti-EtG antibodies was measured. The paper reports a working range of 0.001-100 $\mu\text{g/L}$ on both glass and polyimide substrates and demonstrates that ZnO electrode has better detection sensitivity than gold electrodes. Based on a similar concept, the same group reported a non-Faradaic EIS sensor using Room Temperature Ionic Liquid (RTIL) with nanoporous ZnO electrodes on flexible polymer membranes to enhance the stability of the bioreceptor, antibodies, for the detection of IL-6 and cortisol in spiked human sweat¹⁷. The IL-6 sensors demonstrated distinguishable signals above the specific signal threshold after 168 hours of storage and a 10-hour continuous detection from 0.2 to 200 pg/mL IL-6 in spiked human sweat. A printed two-electrode system functionalized with anti-c-reactive Protein (CRP) antibodies or anti-interleukin-1 β (IL-1 β) was fabricated for non-faradaic EIS detection¹⁸. In addition to cortisol, CRP, and IL-1 β , the same device was modified with other antibodies for IL-6, IL-8, IL-10, tumor necrosis factor α (TNF- α), IL-31, interferon γ (IFN- γ), dehydroepiandrosterone (DHEA), neuropeptide Y (NPY) in collected eccrine sweat¹⁹⁻²⁹.

Although the need for redox species in faradaic EIS immunosensor complicates its execution on the skin as compared with non-faradaic EIS, a stretchable microfluidic module was designed to deliver a pre-deposited redox mediator solution, potassium ferricyanide, to the antibody immobilized 3D nanostructured gold working electrode while washing away the unbound cortisol

and sweat¹⁵. Charge transfer resistance (R_{ct}) in the presence of redox mediator increases with increasing concentration of cortisol from 1 pg/mL to 1 μ g/mL. ATi3C2Tx MXene-loaded laser-induced graphene (LIG) sensor was reported for noninvasive point-of-care cortisol. The introduction of MXene improves the sensitivity of the LIG electrode after transfer onto PDMS. R_{ct} of the sensor increases by approximately 1000 ohms from 10 pM to 100 nM cortisol³⁰. On a similar basis, a thread-based immunosensor was developed by immobilizing anti-cortisol on L-cysteine-gold nanoparticles-MXene modified electrode via EDC/NHS coupling³¹. The change in charge transfer resistance caused by cortisol binding is monitored by amperometry in the presence of potassium ferricyanide and the sensor reports a linearity of 5–180 ng/mL for sweat cortisol detection. In addition to increasing the charge transfer resistance of redox species in solution, antigen association with immobilized antibody may also hinder the kinetics of electron transfer between redox species immobilized below the antibody layer and electrolytes in the solution. Conductive carbon yarn (CCY) deposited with redox-active Fe_2O_3 nanostructure was functionalized with anti-cortisol antibodies for cortisol detection³². Using CV, the magnitude of the redox peak currents decreases with increasing cortisol due to the insulating behavior of cortisol binding. The sensor exhibited a working range of 1 fg/mL to 1 μ g/mL. The same group reported a Zinc Oxide (ZnO) nanorod integrated CCY for cortisol detection.³³ Charge transfer resistance of potassium ferricyanide was monitored using CV and DPV. The change in oxidation peak current as a function of cortisol concentration was found to be linear between 1 fg/mL to 1 μ g/mL. Screen-printed carbon electrode electrodeposited with gold nanoparticles was functionalized with thiol-PEG-carboxylic acid for subsequent anti-cortisol immobilization³⁴. Differential pulse voltammetry in the presence of ferrocenyl methanol was applied to the electrode after cortisol binding and the change in charge transfer resistance was recorded.

Immunosensors are also frequently coupled with direct signals for labeled detection of antigens. The addition of signal labels is believed to amplify analytical signals³⁵. Common labels used for immunosensors include enzymes (peroxidase, alkaline phosphatase, luciferase), fluorescent labels (fluorescein, rhodamine, Cy5), and redox molecules (methylene blue, ferrocene, thionine). However, the requirement of label addition and washing steps impedes labeled immunosensors' practical implementation on the skin. For example, a flexible, wireless sweat cortisol

immunosensor was constructed on laser-engraved graphene electrodes by electropolymerization of carboxyl-rich pyrrole derivative and antibody immobilization with EDC/NHS chemistry.³⁶ Sweat cortisol competes with horseradish peroxidase (HRP) labeled cortisol for binding with immobilized antibodies. The concentration of cortisol has an inverse relation to the cathodic current generated by the enzymatic reduction of hydrogen peroxide in the presence of the mediator, hydroquinone. The sensor was only designed as a point-of-care system as it requires additional washing and substrate steps of the skin. HRP-labeled antigen has also been used as an optical tag for sweat biomarker detection. A labeled competitive immunosensor on capillary arrays was modified with various drug antibodies and drug-HRP (methadone, methamphetamine, amphetamine, and tetrahydrocannabinol)³⁷. Drugs in artificial sweat are detected by adding a chemiluminescent substrate to the array and recording the chemiluminescence image with a CMOS camera. However, the form factors of this technology (rigid capillary array, bulky CMOS camera) make it difficult to integrate with epidermal systems. A skin-interfaced soft microfluidic system was combined with lateral flow immunoassay for sweat collection and cortisol analysis.³⁸ Colorimetric quantitation of sweat cortisol is carried out by capturing the images with a smartphone and correcting for ambient lighting conditions after 5 minutes of incubation on the skin.

Despite the cost of production stability issues and potential batch-to-batch variation, antibodies are still a staple component of current biosensing technologies due to their exceptional sensitivity and selectivity for biomarkers. Future research into the production of nanobodies, a more heat-stable alternative, could potentially resolve issues associated with the storage and implementation of the current generation of immunosensors.³⁹ The production of non-animal-derived antibodies may also provide greater versatility and reproducibility and reduce relevant ethical concerns at the same time.⁴⁰ Although such opportunities exist for antibody manufacturers and researchers, significant effort is needed to produce and investigate the performance of these alternatives before their eventual integration into epidermal sweat sensing systems.

1.2.2 Nucleic acid-based sensors

Aptamers are a new class of bioreceptors produced by *in vitro* selection of single-stranded nucleotides with desired binding affinities. To date, various aptamers are produced to bind to a broad spectrum of targets like metal ions, small molecules, proteins, and whole cells via their 3D stem and/or loop structures.⁴¹ Compared with antibodies, advantages of aptamers include facile and low-cost preparation, low batch-to-batch variability, non-immunogenic properties, easy modification with functional groups, and stability.^{42,43} The unique properties of aptamers make them compatible with many sensing modalities for point-of-care applications.

For example, cortisol aptamers were immobilized with a thiol group termination at the 5' prime end to the ZnO nanoporous electrode previously reported for cortisol immunosensor using non-faradaic EIS⁴⁴. Instead of measuring impedance, the authors performed chronoamperometry by applying a step potential input of 0.35V (0.35 to -0.35) for the 60s. Steady-state current change reveals the change in the non-faradaic capacitive double layer with increasing cortisol concentration. The same group also reported a platform for the simultaneous detection of cortisol and NPY using aptasensors on porous gold electrodes⁴⁵. Non-faradaic EIS is used to monitor the dose-response of both targets and the platform reports detection ranges of 1ng/mL-256 ng/mL (cortisol) and 1pg/mL-256 pg/mL (NPY). Based on the concept of non-faradaic impedance, a tuning circuit-inspired wireless serotonin aptasensor was developed on gold electrode⁴⁶ (Figure 3a). The binding of serotonin to the aptamer induces a conformational change which modulates the surface potential within the electrical double layer. The sensing interface is coupled with a pair of varactor diodes and a coil to form an inductor-capacitor (LC) resonance circuit. Therefore, the change in surface potential of the aptasensor serves as a reverse bias that drives the varactors for battery-free wireless signal transduction. Further validation of this sensing system with other relevant trace-level sweat biomarkers is necessary to demonstrate its feasibility in wearable sweat sensing.

Aptamer's ease of chemical modification has also inspired various tracer-labeled sensing formats. For instance, cortisol aptamer modified with a thiol end and a methylene-blue redox molecule on the opposite side was immobilized on gold electrodes for cortisol sensing⁴⁷. Upon binding, the

aptamers undergo conformation changes by folding. Therefore the distance between the redox molecule and the electrode surface decreases, leading to an increase in the electron transfer rate and redox peak current measured by SWV. A similar concept was implemented to construct an integrated aptasensor array for drugs⁴⁸. Two aptamer sequences (Apt1 and Apt2) which demonstrate different binding affinities to bioamine drugs were modified with methylene blue signal reporter. Gold electrode sensor arrays were either modified with one type of aptamer (Apt1 or Apt2) or both types of aptamer (Apt + Apt2). After variable feature extraction from the electrochemical signals of the aptasensor array, sixteen drug analytes present distinct fingerprints that can be identified in both artificial and human sweat samples.

FET is another popular transducer system that has been interfaced with aptamers for sweat biomolecule sensing. A newly identified cortisol aptamer sequence was immobilized on flexible thin In_2O_3 FET⁴⁹. The conformational change of the aptamer strand after target association leads to the rearrangement of the negatively charged aptamer backbone that modulates the surface charge of the FET, which translates into quantitative changes in gate voltage (V_{GS}) and source-drain current (I_{DS}). An integrated system with an onboard multichannel source measurement unit was developed for on-body applications. Similarly, cortisol aptamer was immobilized on electrospun conducting polyacrylonitrile (PAN) nanofibers deposited with carboxylated poly(3,4-ethylenedioxythiophene) (PEDOT) in a liquid-ion gated FET system on PET⁵⁰. The aptasensor showed high selectivity and sensitivity (LOD = 10 pM) for cortisol detection in human sweat. Although FETs boast high sensitivity and label-free detection mechanisms, their application in real body fluids is limited by the high ionic strength of biofluids, which lowers the signals and deteriorates FET biosensors' sensitivity. The compact structure of aptamers enables target capturing and aptamer folding within the electrical double layer, allowing electrical signal generation.

Aptamers can also be coupled with optical transducers for the POC detection of sweat biomarkers. For instance, an aptamer-based LFA strip was designed for sweat cortisol detection⁵¹. Cortisol aptamers were physically adsorbed to gold nanoparticles (AuNPs). Upon cortisol binding, the aptamers dissociate from AuNP, allowing free AuNPs to be captured by cysteamine immobilized test zone and visual detection of cortisol higher than 1 ng/mL.

Although many believe that aptamers are stable and cheaper alternatives to antibodies, it should be noted that nucleic acids are still susceptible to endogenous nucleases in *in vivo* applications⁵². Mass production of nucleic acids is still costly. The enzymatic stability issue could potentially be addressed by replacing DNA/RNAs with peptide nucleic acid (PNA) and xeno nucleic acids (XNA)^{53,54}. Despite increasing research on the design and selection of sensitive and selective aptamers against various targets, only a limited number of targets have been extensively investigated (e.g., thrombin, cortisol, serotonin).

1.2.3 MIP-based sensors

Molecularly imprinted polymers (MIPs) are synthetic biomimetic bioreceptors whose affinities are generated by self-assembling monomers with a template through covalent or non-covalent interactions and subsequent polymerization to form a cast-like shell⁵⁵. The removal of the template from the polymer generates binding sites for the selective recognition of targets. MIPs are a cheap, mass-producible, robust alternative to conventional bioreceptors like antibodies, enzymes, and aptamers. As MIPs generally do not possess signaling or catalytic properties, the design of signaling mechanisms that respond to the interaction between MIPs and templates is essential to the construction of MIP-based sensors.

In electrochemical MIP sensors, recognition events typically trigger a change in the dielectric properties of the electrode interface and signals are registered in the presence of electroactive species. For example, a flexible electrochemical platform was constructed for sweat urea detection using potassium ferricyanide as redox mediators⁵⁶. Binding of urea with recognition sites on urea imprinted PEDOT on carbon nanotubes (CNT) network and gold nanotubes (AuNT) network hinders the electron transfer of potassium ferricyanide probe, translating into a measurable change in DPV signal. The MIP sensor demonstrates good linear response and selectivity toward physiologically relevant urea levels. The same group reported a flexible electrochemiluminescence (ECL) sensor by imprinting urea and urea on Ru(ii)-PEI@SiO₂ immobilized AuNTs networks⁵⁷. The porous MIP membrane provides electron transfer paths for the electrochemical oxidation of Ru(ii)-PEI@SiO₂ and its ECL emission. As the pores, which are also the binding sites, are occupied by target molecules, the electron transfer channels are gradually blocked, leading to

reduced ECL signals. The ECL platform demonstrated on-body sampling and detection of sweat urea and lactate with high stability. Similarly, MIP-coated Ag Nanowires (AgNWs) on screen-printed lactate electrode was reported for sweat lactate monitoring. The oxidation current of Ag decreases as lactate molecules occupy the imprinted cavities on MIP⁵⁸. Prussian blue (PB) was embedded with cortisol-imprinted electropolymerized polypyrrole MIP as a redox reporter on screen-printed carbon electrodes. The electrodes are coated with porous polyvinyl alcohol (PVA) hydrogel to allow diffusion of cortisol from the accumulated finger sweat to the MIP electrode upon touch. The binding of the cortisol template impedes the electron transfer process of the embedded PB. Using amperometry, the oxidation current of PB decreases as a function of increasing cortisol concentration⁵⁹. To allow continuous sensing, The *in situ* regeneration of electrolymerized MIP can be achieved with amperometry⁶⁰. The authors demonstrated a generic strategy for electroactive species by electropolymerizing with the template on laser-engraved graphene electrodes and conducting detection with DPV. To detect non-electroactive targets, the MIP membrane is prepared on top of the electrodeposited PB layer, and binding events are monitored by linear sweeping voltammetry. The authors demonstrated the sensing of a broad range of small molecule targets including amino acids, metabolites, and nutrients.

A MIP-based, wearable PEDOT:PSS-based organic electrochemical transistor (OECT) was developed for non-invasive cortisol sensing⁶¹. MIP particles are entrapped in an inert plasticized poly(vinyl chloride) matrix to form the molecularly selective membrane (MSM). The binding of cortisol to the MSM modulates the ion transport to the PEDOT:PSS channel, which modulates the drain current. Hence, the OECT transducer allows the detection of non-electroactive targets without the need for a redox reporter. A MIP-based self-powered triboelectric sensor also demonstrated label-free detection of non-electroactive target⁶². Lactate binding on lactate-imprinted MIP on PVDF/graphene electrode lowers the energy barrier and electrical potential of the TENG.

MIP sensors have demonstrated immense potential in the development of wearable and continuous epidermal biosensing technologies. However, several challenges will need to be addressed before the broad adoption and integration of MIP as bioreceptors for on-body biomarker detection. Current research into MIPs primarily focuses on the detection of small molecules and the sensitive

recognition of larger molecules like proteins is rarely explored. Non-specific binding of targets with similar structures and functional groups is a common challenge faced by all MIPs⁶³. This is particularly harder to address for large molecules due to the heterogeneous nature of interactions at the binding sites⁶⁴.

1.2.4 Bioaffinity Sensor Design Considerations

There are countless biosensor configurations with the selection and combination of different bioreceptors and signal transducers. Understanding the unique advantages and disadvantages of different bioreceptors and transducers and thoughtful selection is a critical step to the successful implementation of bioaffinity sensing technologies for wearable sweat analysis. It is nearly impossible to achieve the best sensitivity, selectivity, reproducibility, reusability, and stability at the same time. Therefore, it is crucial to identify and achieve certain critical biosensor characteristics and inevitably to compromise others based on different application scenarios. For instance, if molecules with similar structural and functional groups exist at similar concentrations as a target analyte, it is important to select receptors with better selectivity such as antibodies and aptamers. On the other hand, if the reusability of a sensor is critical for more frequent or continuous sampling, MIPs with limited sensitivity but can be regenerated should be selected. Hence, understanding the nature of a specific target and its analog in sweat and the intended application scenario such as sampling frequency is important before designing bioaffinity sensors.

Bibliography of Chapter 1

1. Kim, J., Campbell, A. S., de Ávila, B. E.-F. & Wang, J. Wearable biosensors for healthcare monitoring. *Nature Biotechnology* **37**, 389–406 (2019).
2. Quesada-González, D. & Merkoçi, A. Mobile phone-based biosensing: An emerging “diagnostic and communication” technology. *Biosensors and Bioelectronics* **92**, 549–562 (2017).
3. Steinhubl, S. R., Muse, E. D. & Topol, E. J. The emerging field of mobile health. *Science Translational Medicine* **7**, 283rv3 (2015).
4. Kumar, S. *et al.* Mobile health technology evaluation: the mHealth evidence workshop. *American Journal of Preventive Medicine* **45**, 228–236 (2013).
5. Vashist, S. K., Luppa, P. B., Yeo, L. Y., Ozcan, A. & Luong, J. H. T. Emerging Technologies for Next-Generation Point-of-Care Testing. *Trends in Biotechnology* **33**, 692–705 (2015).
6. Miyamoto, A. *et al.* Inflammation-free, gas-permeable, lightweight, stretchable on-skin electronics with nanomeshes. *Nature Nanotechnology* **12**, 907–913 (2017).
7. Salvatore, G. A. *et al.* Biodegradable and Highly Deformable Temperature Sensors for the Internet of Things. *Advanced Functional Materials* **27**, 1702390 (2017).
8. Pang, C. *et al.* Highly skin-conformal microhairy sensor for pulse signal amplification. *Advanced Materials* **27**, 634–640 (2015).
9. Piwek, L., Ellis, D. A., Andrews, S. & Joinson, A. The Rise of Consumer Health Wearables: Promises and Barriers. *PLOS Medicine* **13**, e1001953 (2016).
10. Yang, Y. & Gao, W. Wearable and flexible electronics for continuous molecular monitoring. *Chemical Society Reviews* **48**, 1465–1491 (2019).
11. Tu, J., Torrente-Rodríguez, R. M., Wang, M. & Gao, W. The Era of Digital Health: A Review of Portable and Wearable Affinity Biosensors. *Advanced Functional Materials* **30**, 1906713 (2020).
12. Min, J. *et al.* Skin-Interfaced Wearable Sweat Sensors for Precision Medicine. *Chemical Reviews* (2023) doi:10.1021/acs.chemrev.2c00823.
13. Liedberg, B., Nylander, C. & Lundström, I. Biosensing with surface plasmon resonance — how it all started. *Biosensors and Bioelectronics* **10**, i–ix (1995).

14. Malmqvist, M. Biospecific interaction analysis using biosensor technology. *Nature* **361**, 186–187 (1993).
15. Dincer, C. *et al.* Disposable Sensors in Diagnostics, Food, and Environmental Monitoring. *Advanced Material* **31**, e1806739 (2019).
16. Panneer Selvam, A., Muthukumar, S., Kamakoti, V. & Prasad, S. A wearable biochemical sensor for monitoring alcohol consumption lifestyle through Ethyl glucuronide (EtG) detection in human sweat. *Scientific Reports* **6**, 23111 (2016).
17. Munje, R. D., Muthukumar, S., Jagannath, B. & Prasad, S. A new paradigm in sweat based wearable diagnostics biosensors using Room Temperature Ionic Liquids (RTILs). *Scientific Reports* **7**, 1950 (2017).
18. Jagannath, B. *et al.* A Sweat-based Wearable Enabling Technology for Real-time Monitoring of IL-1 β and CRP as Potential Markers for Inflammatory Bowel Disease. *Inflammatory Bowel Diseases* **26**, 1533–1542 (2020).
19. Jagannath, B. *et al.* Temporal profiling of cytokines in passively expressed sweat for detection of infection using wearable device. *Bioengineering & Translational Medicine* **6**, e10220 (2021).
20. Tuning SLOCK toward Chronic Disease Diagnostics and Management: Label-free Sweat Interleukin-31 Detection. *ACS Omega* **6**, 20422-20432
21. Upasham, S. & Prasad, S. SLOCK (sensor for circadian clock): passive sweat-based chronobiology tracker. *Lab Chip* **20**, 1947–1960 (2020).
22. Kothari, A., Jagannath, B., Muthukumar, S. & Prasad, S. An observational study for detection and quantification of interferon- γ in sweat toward inflammation monitoring. *Biosensors and Bioelectronics: X* **10**, 100122 (2022).
23. Upasham, S., Osborne, O. & Prasad, S. Demonstration of sweat-based circadian diagnostic capability of SLOCK using electrochemical detection modalities. *RSC Advances* **11**, 7750–7765 (2021).
24. Churcher, N. K. M., Upasham, S., Rice, P., Bhadsavle, S. & Prasad, S. Development of a flexible, sweat-based neuropeptide Y detection platform. *RSC Advances* **10**, 23173–23186 (2020).

25. Upasham, S., Thai, K., Muthyala, R. & Prasad, S. Flexible, low volume detection of chronobiology biomarkers from human sweat. *Analyst* **145**, 784–796 (2020).
26. Upasham, S., Rice, P., Pali, M. & Prasad, S. FLOCK -flare clock: Passive sweat-based eczematous flare detection system. *Biosensors and Bioelectronics: X* **10**, 100120 (2022).
27. Upasham, S., Rice, P., Shahub, S., Dhamu, V. N. & Prasad, S. Passive Sweat-Based Pruritic Cytokine Detection and Monitoring System. *ECS Sensors Plus* **1**, 031602 (2022).
28. Upasham, S., Bhide, A., Lin, K.-C. & Prasad, S. Point-of-use sweat biosensor to track the endocrine–inflammation relationship for chronic disease monitoring. *Future Science OA* **7**, FSO628.
29. Kinnamon, D., Ghanta, R., Lin, K.-C., Muthukumar, S. & Prasad, S. Portable biosensor for monitoring cortisol in low-volume perspired human sweat. *Scientific Reports* **7**, 13312 (2017).
30. Nah, J. S. *et al.* A wearable microfluidics-integrated impedimetric immunosensor based on Ti3C2Tx MXene incorporated laser-burned graphene for noninvasive sweat cortisol detection. *Sensors and Actuators B: Chemical* **329**, 129206 (2021).
31. Laochai, T. *et al.* Non-invasive electrochemical immunosensor for sweat cortisol based on L-cys/AuNPs/ MXene modified thread electrode. *Biosensors and Bioelectronics* **203**, 114039 (2022).
32. Sekar, M., Pandiaraj, M., Bhansali, S., Ponpandian, N. & Viswanathan, C. Carbon fiber based electrochemical sensor for sweat cortisol measurement. *Scientific Reports* **9**, 403 (2019).
33. Madhu, S. *et al.* ZnO Nanorod Integrated Flexible Carbon Fibers for Sweat Cortisol Detection. *ACS Applied Electronic Materials* **2**, 499–509 (2020).
34. Cheng, C. *et al.* Battery-free, wireless, and flexible electrochemical patch for in situ analysis of sweat cortisol via near field communication. *Biosensors and Bioelectronics* **172**, 112782 (2021).
35. Aizawa, M. *et al.* Immunosensors. *Philosophical Transactions of the Royal Society of London. B, Biological Sciences* **316**, 121–134 (1987).

36. Torrente-Rodríguez, R. M. *et al.* Investigation of Cortisol Dynamics in Human Sweat Using a Graphene-Based Wireless mHealth System. *Matter* **2**, 921–937 (2020).
37. Xue, W. *et al.* Rapid and sensitive detection of drugs of abuse in sweat by multiplexed capillary based immuno-biosensors. *Analyst* **145**, 1346–1354 (2020).
38. Kim, S. *et al.* Soft, skin-interfaced microfluidic systems with integrated immunoassays, fluorometric sensors, and impedance measurement capabilities. *Proceedings of the National Academy of Sciences* **117**, 27906–27915 (2020).
39. De Meyer, T., Muyldermans, S. & Depicker, A. Nanobody-based products as research and diagnostic tools. *Trends in Biotechnology* **32**, 263–270 (2014).
40. Gray, A. *et al.* Animal-free alternatives and the antibody iceberg. *Nature Biotechnology* **38**, 1234–1239 (2020).
41. Zheng, J. *et al.* Rationally designed molecular beacons for bioanalytical and biomedical applications. *Chemical Society Reviews* **44**, 3036–3055 (2015).
42. Rusconi, C. P. *et al.* RNA aptamers as reversible antagonists of coagulation factor IXa. *Nature* **419**, 90–94 (2002).
43. Song, S., Wang, L., Li, J., Fan, C. & Zhao, J. Aptamer-based biosensors. *TrAC Trends in Analytical Chemistry* **27**, 108–117 (2008).
44. Pali, M. *et al.* CATCH (Cortisol Apta WATCH): ‘Bio-mimic alarm’ to track Anxiety, Stress, Immunity in human sweat. *Electrochimica Acta* **390**, 138834 (2021).
45. Churcher, N. K. M. *et al.* AptaStrensor (aptamer-based sensor for stress monitoring): The interrelationship between NPY and cortisol towards chronic disease monitoring. *Biosensors and Bioelectronics: X* **10**, 100145 (2022).
46. Liu, T.-L. *et al.* Battery-free, tuning circuit–inspired wireless sensor systems for detection of multiple biomarkers in bodily fluids. *Science Advances* **8**, eabo7049 (2022).
47. Yuan, Y. *et al.* Oil-Membrane Protection of Electrochemical Sensors for Fouling- and pH-Insensitive Detection of Lipophilic Analytes. *ACS Applied Materials & Interfaces* **13**, 53553–53563 (2021).
48. Zhang, X. *et al.* Integrated Aptasensor Array for Sweat Drug Analysis. *Analytical Chemistry* **94**, 7936–7943 (2022).

49. Wang, B. *et al.* Wearable aptamer-field-effect transistor sensing system for noninvasive cortisol monitoring. *Science Advances* **8**, eabk0967 (2022).
50. An, J. E. *et al.* Wearable Cortisol Aptasensor for Simple and Rapid Real-Time Monitoring. *ACS Sensors* **7**, 99–108 (2022).
51. Dalirirad, S. & Steckl, A. J. Aptamer-based lateral flow assay for point of care cortisol detection in sweat. *Sensors and Actuators B: Chemical* **283**, 79–86 (2019).
52. Liu, L. S., Wang, F., Ge, Y. & Lo, P. K. Recent Developments in Aptasensors for Diagnostic Applications. *ACS Applied Materials & Interfaces* **13**, 9329–9358 (2021).
53. Minagawa, H. *et al.* Selection, Characterization and Application of Artificial DNA Aptamer Containing Appended Bases with Sub-nanomolar Affinity for a Salivary Biomarker. *Scientific Reports* **7**, 42716 (2017).
54. Wang, F. *et al.* Synthetic α -l-Threose Nucleic Acids Targeting Bcl-2 Show Gene Silencing and in Vivo Antitumor Activity for Cancer Therapy. *ACS Applied Materials & Interfaces* **11**, 38510–38518 (2019).
55. Selvolini, G. & Marrazza, G. MIP-Based Sensors: Promising New Tools for Cancer Biomarker Determination. *Sensors (Basel)* **17**, 718 (2017).
56. Liu, Y.-L. *et al.* Flexible Electrochemical Urea Sensor Based on Surface Molecularly Imprinted Nanotubes for Detection of Human Sweat. *Analytical Chemistry* **90**, 13081–13087 (2018).
57. Chen, M.-M. *et al.* Construction of a flexible electrochemiluminescence platform for sweat detection. *Chemical Science* **10**, 6295–6303 (2019).
58. Zhang, Q. *et al.* Wearable electrochemical biosensor based on molecularly imprinted Ag nanowires for noninvasive monitoring lactate in human sweat. *Sensors and Actuators B: Chemical* **320**, 128325 (2020).
59. Tang, W. *et al.* Touch-Based Stressless Cortisol Sensing. *Advanced Materials* **33**, 2008465 (2021).
60. Wang, M. *et al.* A wearable electrochemical biosensor for the monitoring of metabolites and nutrients. *Nature Biomedical Engineering* 1–11 (2022) doi:10.1038/s41551-022-00916-z.

61. Parlak, O., Keene, S. T., Marais, A., Curto, V. F. & Salleo, A. Molecularly selective nanoporous membrane-based wearable organic electrochemical device for noninvasive cortisol sensing. *Science Advances* **4**, eaar2904 (2018).
62. Kanokpaka, P. *et al.* Self-powered molecular imprinted polymers-based triboelectric sensor for noninvasive monitoring lactate levels in human sweat. *Nano Energy* **100**, 107464 (2022).
63. Morales, M. A. & Mark Halpern, J. Guide to Selecting a Biorecognition Element for Biosensors. *Bioconjugate Chemistry* **29**, 3231–3239 (2018).
64. Verheyen, E. *et al.* Challenges for the effective molecular imprinting of proteins. *Biomaterials* **32**, 3008–3020 (2011).

Chapter 2

A MHEALTH SENSOR FOR STRESS MONITORING

Materials from this chapter appear in “Torrente-Rodríguez R. M.; Tu, J.; Yang, Y.; Min, J.; Wang, M.; Song, Y.; Yu, Y.; Xu, C.; Ye, C.; IsHak, W. W.; Gao, W. Investigation of cortisol dynamics in human sweat using a graphene-based wireless mHealth system. *Matter* 2, 927-937 (2020) doi:10.1016/j.matt.2020.01.021.”

2.1 Introduction

The exponential increase in the pace of life in the 21st century constantly demands intense and prolonged mental as well as physical efforts from individuals,¹ both of which are potential triggers of stress. Chronic stress has been associated with higher risks of anxiety, depression, suicide, weakening immune response as well as cardiovascular diseases (CVD).² The need for measurable stress indicators has never been more than apparent, be it in the contexts of posttraumatic stress disorder (PTSD) screening and depression evaluation, or a more general mental and somatic health monitoring setting. Although psychosocial and physiological stresses are induced by distinct stimuli, they share similar neuroendocrine and behavioral responses regulated by the hypothalamic-pituitary-adrenal (HPA) axis.³ Activation of the HPA axis stimulates the secretion of glucocorticoids (e.g., cortisol), a group of hormones that mobilize energy in the body to cope with stress (**Fig. 2-1a**).⁴ While short-term alterations in the HPA axis are deemed as normal and adaptive responses of the body, chronic dysregulation of the HPA axis, an energetically costly state, is associated with various pathological processes. As such, stress and individuals' stress-coping responses are perceived as dynamic processes; absolute quantification of stress level provides much richer information and greater diagnostic value in the context of time and environment.⁵

Experience sampling methods (ESM) such as questionnaires and diary studies play a pivotal role in establishing the situational contexts of stressors in relevant longitudinal stress-response studies; however, their inherent idiosyncrasy imposed by subjective interpretations challenges the accuracy of "stress level" assessment.^{6,7} Quantification of stress hormones in biological fluids provides measurable physiological indicators for mental distress. For example, the disturbances in circadian patterns of a key stress hormone, cortisol, are linked to PTSD and major depressive disorder (MDD) (**Fig. 2-1b**).^{8,9} In addition, the cortisol dynamics in stress response plays a crucial role in human performance (**Fig. 2-1c**).¹⁰ Other than the direct assessment of stress, stress hormones are also important in the understanding of pain and fear neural circuits,^{11,12} both of which are subjective sensation or emotion that are hard to quantify. Blood test, albeit being the most well-studied hormone assessment method, is afflicted by its invasive nature and potential role as a stress

stimulus. Saliva and sweat analyses, on the other hand, offer an attractive alternative for non-invasive stress hormones dynamics studies.

Recent advances in wearable and mobile health (mHealth) sensing systems have opened up a window of opportunities for hassle-free, real-time, personalized physiological data collection.¹³⁻²¹ Substantial progress in the realm of wearable physical sensing platform has been made with systems capable of documenting physical and kinematic data such as temperature,²² pulse rate²³ and ECG²⁴ in real time. Although human sweat contains rich health information and could allow non-invasive molecular monitoring, the majority of the wearable or portable systems available for sweat chemical biomarker dynamics studies are still limited to high concentration (usually at mM level) analytes like pH, sodium, chloride, and glucose.²⁵⁻³⁰ To date, the reported sweat hormone sensors were generally characterized in either buffer or artificial sweat samples,^{31,32} and the dynamics of the sweat stress hormones has not yet been well studied.

In this chapter we investigate the dynamics of the sweat stress hormone using an integrated wireless mHealth device — graphene-based sweat stress sensing system (GS⁴) (**Fig. 2-1a**). As a proof-of-concept, cortisol is selected as the model stress hormone for dynamic profiling. Highly sensitive, selective, and efficient cortisol sensing in human sweat and saliva is achieved through a unique approach that combines the laser-induced graphene and competitive immunosensing. We report here, for the first time, the cortisol diurnal cycle and the dynamic stress response profile constructed from sweat using an integrated sensing device (**Fig. 2-1a**). A strong correlation between sweat and serum cortisol levels are obtained from a small-scale pilot study. Such a wearable and point-of-care device-enabled non-invasive sweat analysis would add another dimension to stress monitoring since it offers minimal disturbance of daily routines and could provide instantaneous and continuous assessments on subjects' psychological state.

The key component of our GS⁴ platform is a flexible five-electrode graphene sensor patch fabricated on a polyimide (PI) substrate via laser engraving as illustrated in **Fig. 2-1d-f**. It boasts the advantage of rapid, scalable, and low-cost production (**Fig. 2-1e**), and does not require elaborate lithography equipment or fabrication masks as compared with screen-printed electrodes. The flexible sensor patch consists of three graphene working electrodes (WEs), one Ag/AgCl

reference electrode (RE), and one graphene counter electrode (CE) as it is depicted in **Fig. 2-1f**. Detection of cortisol in human sweat is achieved through the combination of carboxylate-rich pyrrole-derivative grafting and subsequent modification on graphene surface and a competitive sensing strategy. The large surface area and fast electron mobility of graphene offers superior performance in electrochemical sensing (**Fig. 2-1g**),³³ while competitive immunosensing strategies offer major advances in highly selective small hormone molecule detection.³⁴

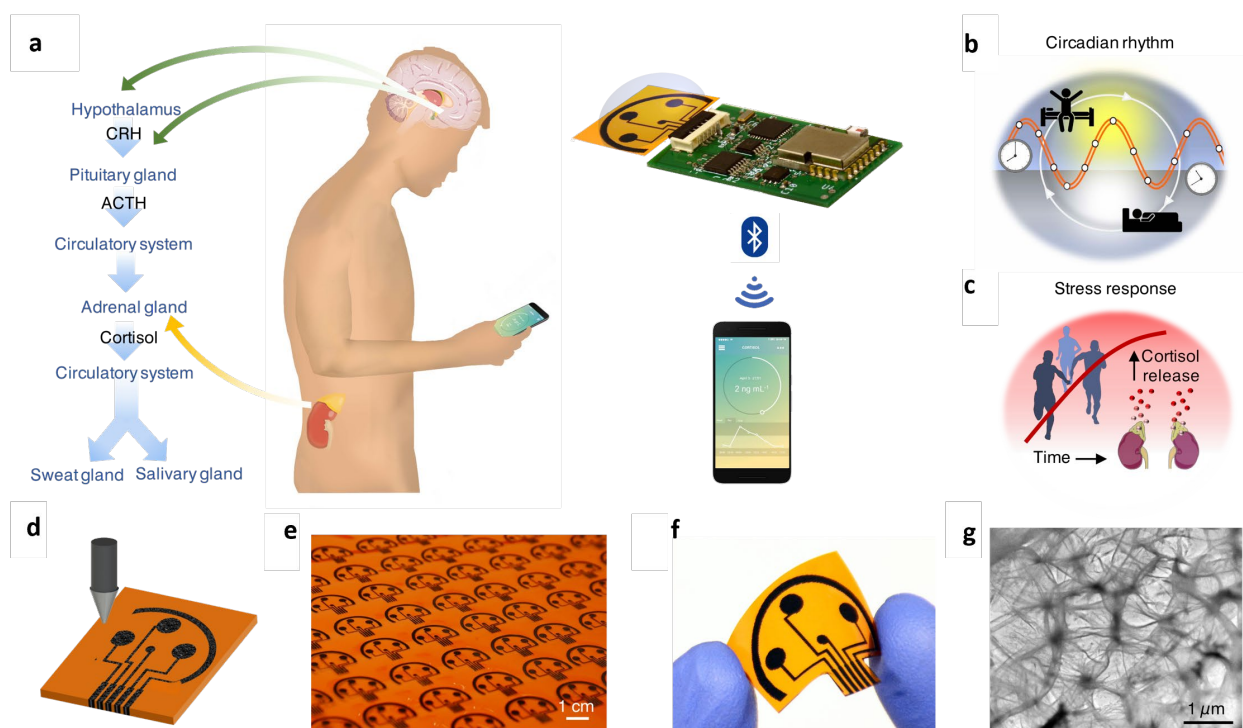


Figure 2-1. An integrated wireless graphene-based sweat stress sensing system (GS4) for dynamic and non-invasive stress hormone analysis. **a**, Schematic illustration of the origin of cortisol in sweat and saliva and the use of the GS4 to track the circulating cortisol level. CRH, corticotrophin-releasing hormone; ACTH, adrenocorticotrophic hormone. **b**, Conceptual illustration of cortisol dynamics regulated by circadian rhythm. **c**, Conceptual illustration of cortisol dynamics and triggered by physiological and psychological stress. **d**, Illustration of the laser engraving process of a graphene platform. **e**, Graphene sensor arrays mass-produced on a

polyimide (PI) substrate. **f**, Image of a disposable flexible graphene sensor array. **g**, Transmission electron microscopy (TEM) image of the graphene electrode surface.

2.2 Laser-engraved graphene-based cortisol sensor

2.2.1 Materials and Methodology

Materials

1-H pyrrole propionic acid (PPA, 97%), 1-ethyl-3-(3-dimethylammonopropyl)carbodiimide (EDC), N-hydroxysulfosuccinimide (Sulfo-NHS), bovine serum albumin (BSA), hydroquinone (HQ), 2-(N-morpholino)ethanesulfonic acid (MES), Tween® 20, hydrocortisone, cortisone, progesterone, β -estradiol, sodium thiosulfate, sodium bisulfite and potassium ferrocyanide (II) were purchased from Sigma Aldrich. Sodium dihydrogen phosphate, potassium hydrogen phosphate, potassium chloride, hydrogen peroxide (30% w/v) and sulfuric acid were purchased from Fischer Scientific. Potassium ferricyanide (III) and silver nitrate, iron (III) chloride and 0.1 M PBS (pH 7.4) were purchased from Across Organics and Alfa Aesar, respectively. Anti-cortisol murine monoclonal antibody and HRP-labeled cortisol were purchased from EastCoastBio. Cortisol competitive human ELISA kit (Catalog. No. EIAHCOR) was purchased from Thermo Fisher. Polyimide film (PI, 75 μ m thick) was purchased from DuPont.

Fabrication of three-channel laser-engraved graphene sensors

For three-channel graphene sensor fabrication, a PI film was attached onto a supporting substrate in a 50 W CO₂ laser cutter (Universal Laser System). Selected laser-cutting parameters were: Power 5.0%, Speed 6%, Points Per Inch (PPI) 1000, in raster mode and at focused height. Ag/AgCl reference electrodes (RE) were fabricated by electrodeposition in 20 μ L of a mixture solution containing silver nitrate, sodium thiosulfate, and sodium bisulfite (final concentrations 250 mM, 750 mM and 500 mM, respectively) for 100 seconds at -0.2 mA, followed by drop casting 10 μ L-aliquot of FeCl₃ for 1 minute.

Modification of sensing platform and electrochemical detection

PPA electropolymerization was conducted by CV from 0.0 to 0.85 V (vs. Ag/AgCl) for 20 cycles at a scan rate of 0.1 V/s in a fresh solution containing 5.0 mM carboxyl-functionalized pyrrole

monomer and 0.5 M KCl. After rinsing with deionized (DI) water and drying under air flow, electrodes were incubated with 10 μ L of a mixture solution containing 0.4 M EDC and 0.1 M Sulfo-NHS in 0.025 M MES, pH 5.0, for 35 minutes at room temperature under humid ambient conditions. Covalent attachment of specific antibody onto activated surface was carried out by drop casting 10 μ L of anti-cortisol antibody solution (100 μ g/mL in MES buffer, pH 5.0) and incubated at room temperature for 90 minutes, followed by a 1 hour blocking step with 1.0% BSA prepared in 0.01 M phosphate buffered saline with Tween® 20 (PBST) of pH 7.4. After one washing step with same buffered solution, 10 μ L-aliquots of cortisol standards (or the biofluid to be analyzed properly diluted) and HRP-cortisol (1/200 dilution) prepared in PBST, pH 7.4, were drop casted onto the working electrode, allowing competition between labeled and circulating free cortisol contained in the sample for the available free sites of the immobilized affinity receptor to take place for 15 minutes. Amperometric readings were registered at -0.2 V (vs. Ag/AgCl) in 50 mM sodium phosphate buffer of pH 6.0 containing 2.0 mM HQ. The readout signal was obtained after a 30 μ L-aliquot of 10 mM H₂O₂ was injected to the system.

Characterization of the biosensing platform

The morphology and material properties of the graphene sensing electrodes before and after surface modification were characterized by TEM, SEM, Raman and XPS. The SEM images of graphene electrodes were obtained by focused ion beam SEM (FIB-SEM, FEI Nova 600 NanoLab). TEM images were obtained by transmission electron microscope (TecnaiTF-20). The surface properties of the laser-induced graphene were characterized by X-ray photoelectron spectroscopy (Escalab 250xi, Thermo Scientific). Raman spectrum of the graphene was recorded using a 532.8 nm laser with an inVia Reflex (Renishaw, UK).

Amperometry, open circuit potential-electrochemical impedance spectroscopy (OCP-EIS), cyclic voltammetry (CV), and differential pulse voltammetry (DPV) were carried out on a CHI820 electrochemical station by means of an electrochemical setup comprising laser-induced graphene electrodes (LGEs) as the working electrodes (WEs), a platinum wire as the counter electrode (CE), and a commercial Ag/AgCl electrode as the reference electrode (RE).

In order to characterize surface modification after each step electrochemically, DPV and OCP-EIS readings were carried out in 0.01 M PBS, pH 7.4, containing 2.0 mM of K₄Fe(CN)₆/K₃Fe(CN)₆ (1:1) at detailed conditions: potential range, -0.3 and 0.6 V; pulse width, 0.2 s; incremental potential, 4 mV; amplitude, 50 mV; frequency range, 0.1–106 Hz; amplitude, 5 mV. Performances of LGEs, glassy carbon electrodes (GCEs) and commercial screen-printed carbon electrodes (SPCEs) were compared through current densities (nA/mm²) obtained after developing the proposed competitive-based assay on both carbon surfaces for target cortisol determination at 1.0 and 5.0 ng/mL levels under optimized conditions. Dilution of HRP labeled cortisol was optimized by comparing amperometric responses obtained for 1/100, 1/200 and 1/300 diluted enzymatic tracer for 0.0 and 10.0 ng/mL cortisol standards. Performance of our device was evaluated for different pHs and salt contents ranging from 7.1 to 4.1 and from 0.1 M PBST to 0.001 M PBST, respectively. Selectivity test was conducted in the presence of mixture solutions of 1/200 HRP-cortisol enzymatic tracer containing 5.0 ng/mL cortisone, progesterone or β -estradiol, in the absence or in the presence of target hormone at the same concentration level. Stability study was conducted for target cortisol determination at 5.0 ng/mL levels under optimized conditions. The electrodes for stability study were modified on the same day and stored at 4 °C for 0 to 35 days before carrying out the competitive assay.

Enzyme-linked immunosorbent assay for human sample analysis validation

ELISA tests for cortisol were performed in an accuSkan™ FC Filter-Based Microplate Photometer at a detection wavelength of 450 nm, according to the manufacturer's instructions. Briefly, standards (or properly diluted samples), HRP-cortisol conjugate and cortisol antibody were added to IgG coated microtiter plate wells and incubated during 1 hour at room temperature. After four washing steps with wash buffer, 100 μ L of 3,3',5,5'-Tetramethylbenzidine (TMB) substrate was incubated for 30 minutes and absorbance values were measured immediately after addition of 50 μ L of 1M H₂SO₄ in each well.

2.2.2 Results and Discussion

Figure 2-2 illustrates the sequential surface modification of graphene electrodes for cortisol determination. Polymerization of pyrrole propionic acid (PPA) improves the strength and adhesion of polymeric films to transducer surfaces and facilitates subsequent surface modifications with carboxylate moieties for affinity-based sensor fabrication. In contrast to conventional graphene modification techniques such as acid reflux or monolayer formation of aryl hydrocarbon derivative, the electro-grafting of pyrrole-derivative is fast (~ 260 s), controlled, and scalable (by connecting electrodes in parallel). Upon electropolymerization of PPA, the graphene electrode is activated by 1-Ethyl-3-(3-dimethylaminopropyl)carbodiimide (EDC) and N-hydroxysulfosuccinimide (Sulfo-NHS) for covalent immobilization of anti-cortisol monoclonal antibody (mAb), followed by deactivation of unreacted sites with bovine serum albumin (BSA). This surface biomodification is universal to all bioaffinity receptors immobilization and could be adapted for other hormone antibodies. In the event of sweat analysis, sweat cortisol and horseradish peroxidase (HRP)-labeled cortisol compete for binding onto antibody-modified graphene electrode surface; enzymatic reduction of hydrogen peroxide mediated by hydroquinone (HQ) generates a cathodic current which is inversely proportional to the amount of cortisol in biofluids. The sensing mechanism is schematized in **Fig. 2-3**. After brief incubation of the sensor with sweat containing the enzymatic tracer (HRP-labeled cortisol), amperometric response at -0.2 V (vs. Ag/AgCl) in the presence of detection substrate (HQ/H₂O₂) is recorded.

To confirm the successful sensor modification, material properties of the graphene surface are characterized by scanning electron microscopy (SEM) (**Fig. 2-4**), Raman spectroscopy (**Fig. 2-5**) and X-ray photoelectron spectroscopy (XPS) (**Fig. 2-6**). The decrease in I_D/I_G value in the Raman spectrum after surface modification implies the improvement of defect concentration after a thin uniform layer of pyrrole derivative is deposited (**Fig. 2-5**). The significantly increased N1s and S2p peaks in XPS (**Fig. 2-6**) indicate the successful activation of the surface and the immobilization of the capture antibody (CAb) on the sensing electrode. Moreover, open circuit potential-electrochemical impedance spectroscopy (OCP-EIS) and differential pulse voltammetry (DPV) techniques are applied to electrochemically characterize the surface after each modification

step involved in the affinity-based assay. Nyquist plots for the graphene electrode exhibit increasing resistance after each modification step as a consequence of impeded interfacial electron transfer between the redox probe in solution and the functionalized transducer surface (**Fig. 2-7**). The successful polymer deposition and the effective affinity bioreceptor immobilization on the modified-graphene surface are also confirmed by DPV (**Fig. 2-8**). The effect of HRP-labeled cortisol concentration on amperometric responses is investigated. A dilution factor of 200 is chosen as it yields the largest ratio between currents for 0.0 ($I_{0.0}$) and 10.0 ng/mL ($I_{10.0}$) cortisol (**Fig. 2-9**).

The performance of the as-prepared sensor is evaluated by measuring amperometric readout in phosphate buffered (PB) solutions containing varied cortisol concentrations (**Fig. 2-10**). Sensors prepared with laser-induced graphene electrodes (LGEs) demonstrate a much higher sensitivity with six- and nearly two-folds reduction in current density between 0.0 and 1.0 ng/mL (3.72 vs. 0.68 and 3.72 vs. 2.41 nA/mm²) as compared with screen-printed carbon electrodes (SPCEs) and glassy carbon electrodes (GCE), respectively (**Fig. 2-11**). Amperometric signals (I) obtained with competitive strategies are best described by a sigmoidal curve using the four-parameter logistic (4-PL) model following the equation:³⁵

$$I = i_l + \frac{i_2 - i_l}{1 + 10^{(\log IC_{50} - x) * p}}$$

where i_2 and i_l indicate the maximum and minimum current values of the dose-response curve obtained; IC_{50} represents the level of cortisol at which amperometric signal decreases to 50% of the maximum current, x is the cortisol concentration in log scale, and p is the Hill slope at the inflection point of the sigmoid curve. Sigmoidal calibration plots of cathodic currents as a function of cortisol concentrations in buffer, sweat and saliva samples from a healthy subject are demonstrated in **Fig. 2-12**. No significant slope variations are observed between data obtained in human biospecimens and in buffered solutions. The limit of detection (LOD), calculated as the concentration of cortisol that produces 10% inhibition binding of HRP-labeled tracer to the immobilized affinity receptor (i.e., 10% signal reduction) is 0.08 ng/mL. The concentration range for 20%–80% inhibition binding of the enzymatic tracer is 0.43–50.2 ng/mL cortisol, covering the physiologically relevant range in sweat and saliva samples reported in previous studies.³⁶⁻³⁸

Considering that human sweat exhibits huge interpersonal variations in pH and salt content, the performance of the sensors under various pH levels and ionic strength conditions is evaluated (**Fig. 2-13**). The consistent sensor signals indicate the universality of the sigmoidal calibration curve constructed. In addition, the selectivity of our cortisol sensor is investigated by comparing the sensor responses in the presence of other non-target hormones. As illustrated in **Fig. 2-13**, no cross-reactivity is observed for β -estradiol, progesterone, and cortisone.

Target binding is the rate determining factor in bioaffinity sensors. To ensure rapid analysis and to allow sufficient time for binding, a crucial criterion at the point-of-care – the effect of competition time on sensor responses is investigated. **Fig. 2-14** shows the amperometric responses obtained for 0.0 and 5.0 ng/mL cortisol with different incubation times (30 seconds, 1, 5, 15, and 60 minutes). 15-minute recognition time is employed for real sample analysis presented in this work in order to ensure accurate quantitation of ultra-low levels of cortisol in biofluids with a high contrast-to-noise ratio. Here, the incubation time selected is based on the experimental observation of the optimum competition rate rather than the time for binding equilibrium, as the equilibrium time is long for a heterogeneous system. Nonetheless, significant competition (47%) is observed for 5.0 ng/mL cortisol with even 1-minute incubation, indicating that our sensor is capable of close to real-time analysis of sweat cortisol at ng/mL level (much faster compared to recent published sensing methodologies).^{31, 38} One potential strategy to further shorten the incubation time is through enhanced mixing to promote the availability of unbound cortisol to antibodies on the graphene surface.

Endogenous circulating cortisol levels in human body fluids measured with the proposed methodology in human sweat samples (as well as saliva samples, collected from eight healthy participants) are validated with the gold standard enzyme-linked immunosorbent assay (ELISA). A high correlation between the results from the ELISA and the sensors ($r = 0.973$) is obtained (**Fig. 2-15**), endorsing the accuracy of rapid cortisol quantification with our device. In addition, the sensors retained good amperometric responses (> 90%) after storing at 4 °C for 7 days (**Fig. 2-16**).

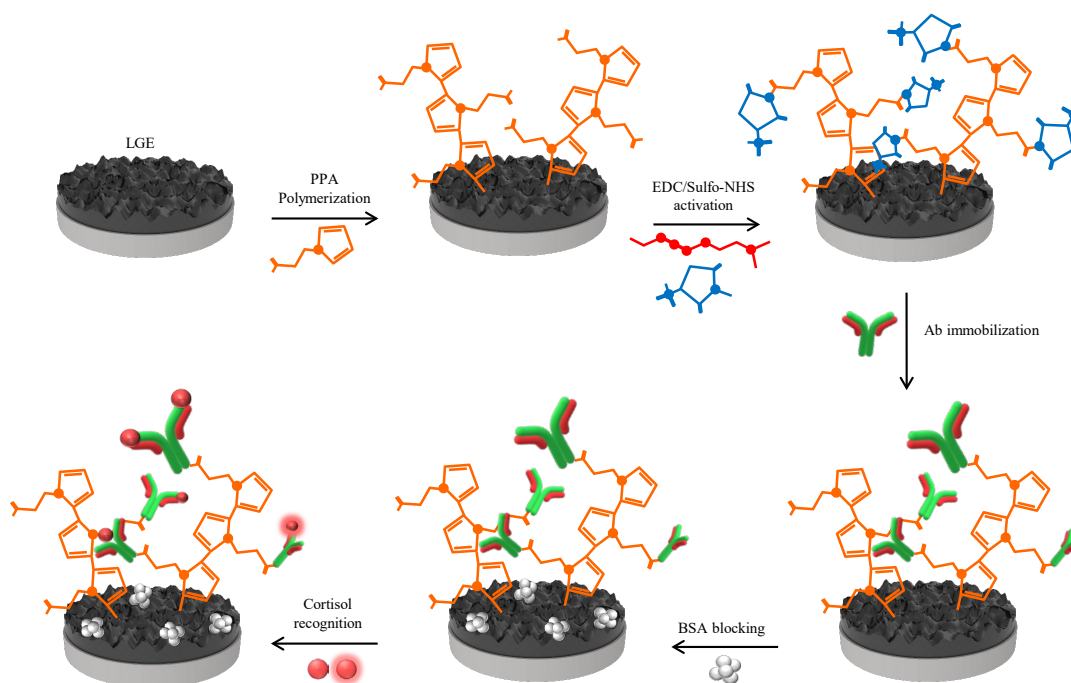


Figure 2-2. Schematic of modification procedure of the graphene electrode for cortisol sensing.

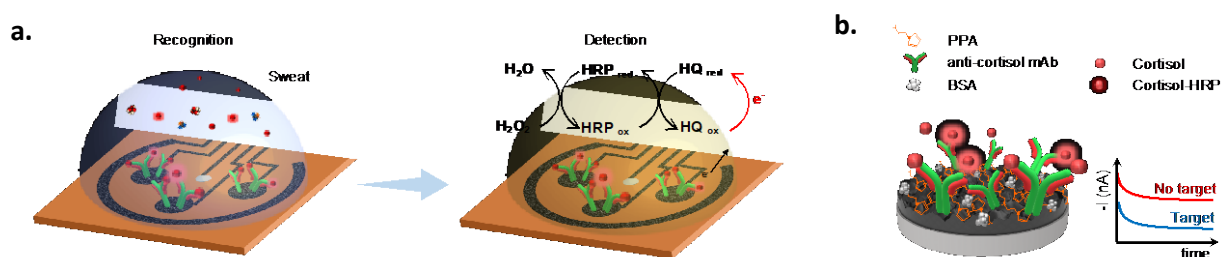


Figure 2-3. Schematic of the electrochemical detection of cortisol in human sweat. a, Representation of the affinity-based electrochemical cortisol sensor recognition and detection mechanisms. **b,** Illustration of the cortisol sensing electrode surface and representative amperometric signals in the presence and absence of cortisol. HRP, horseradish peroxidase; HQ,

hydroquinone; PPA, pyrrole propionic acid; BSA, bovine serum albumin; mAb, monoclonal antibody.

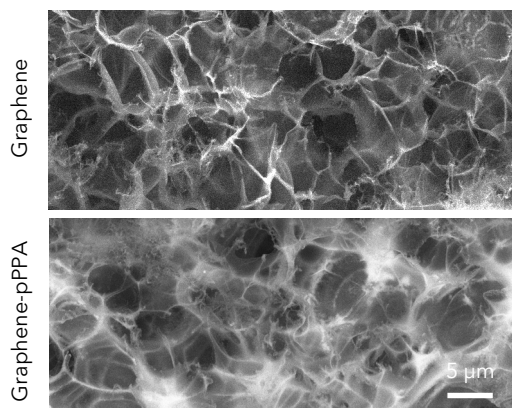


Figure 2-4. Scanning electron microscopy (SEM) images of the graphene electrode surface before and after PPA polymerization.

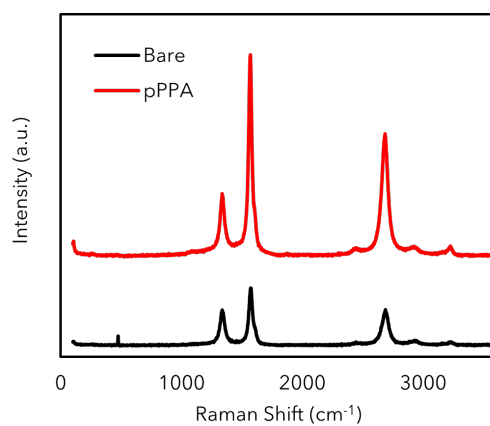


Figure 2-5. Raman spectra of bare graphene electrode, and graphene electrodes modified with PPA (pPPA) and capture antibody (CAb).

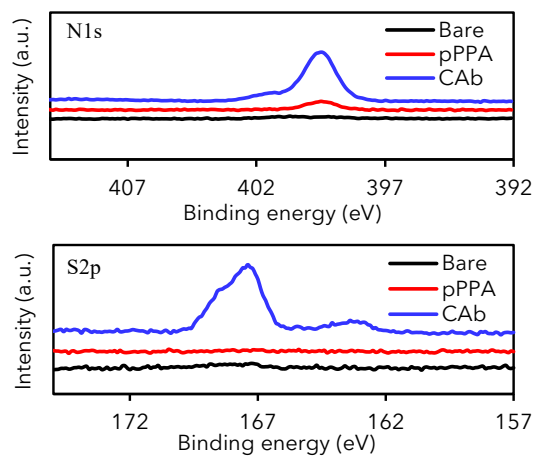


Figure 2-6. X-ray photoelectron spectra (XPS) of bare graphene electrode, and graphene electrodes modified with PPA (pPPA) and capture antibody (CAb).

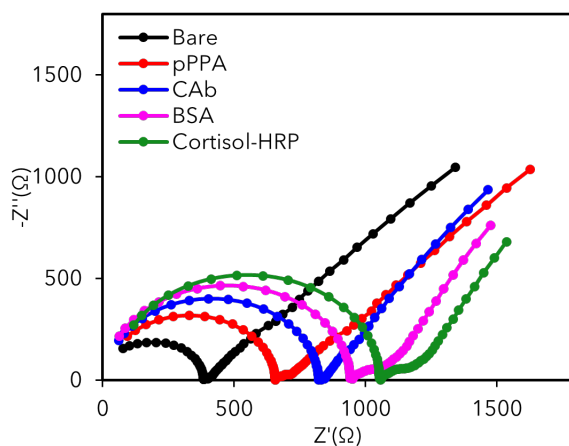


Figure 2-7. Nyquist plots of a graphene electrode in a 0.01 M PBS solution containing 2.0 mM of $K_4Fe(CN)_6/K_3Fe(CN)_6$ (1:1) after each surface modification step. bare graphene, electropolymerization of PPA (pPPA), capture antibody immobilization (CAb), blocking with BSA and incubation with enzyme-tagged cortisol (cortisol-HRP).

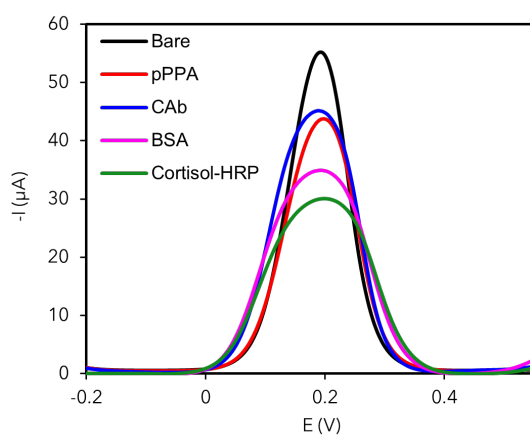


Figure 2-8. Characterization of the graphene sensor. Differential pulse voltammetry (DPV) in 2.0 mM of $K_4Fe(CN)_6/K_3Fe(CN)_6$ (1:1) after each modification step.

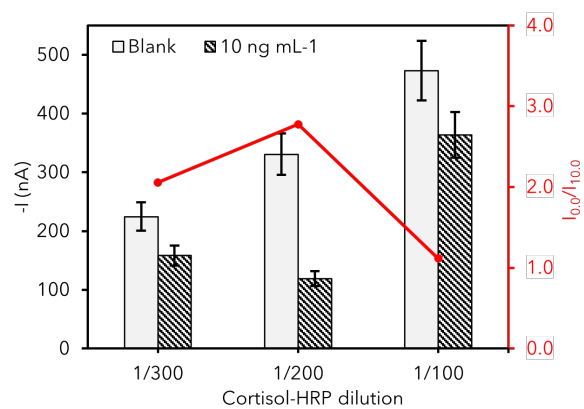


Figure 2-9. Electrochemical cortisol sensor optimization. Effect of cortisol-HRP dilution factor on amperometric signals. Data are represented as mean \pm SD (n = 3).

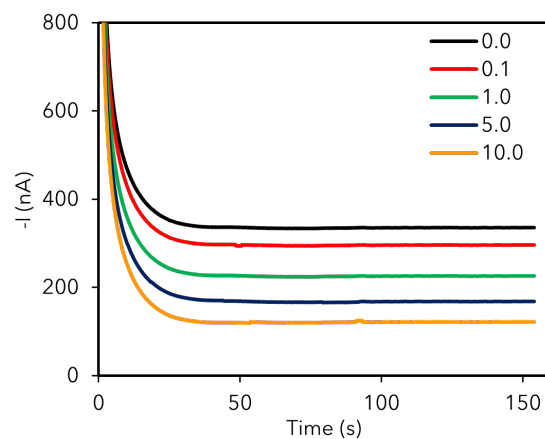


Figure 2-10. Amperometric signals of the flexible graphene-based biosensors for 0.0–10.0 ng/mL cortisol in 0.01 M PBST, pH 7.4.

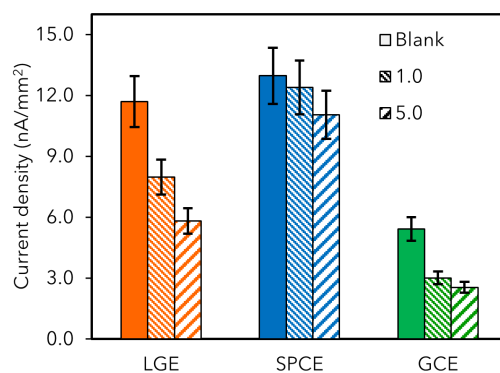


Figure 2-11. Sensor performance of laser-induced graphene electrode (LGE) vs. screen printed carbon electrode (SPCEs) and glassy carbon electrodes (GCEs). Current densities were obtained from 0.0, 1.0, and 5.0 ng/mL cortisol solutions. Data are presented as mean \pm standard deviation (SD) ($n = 3$).

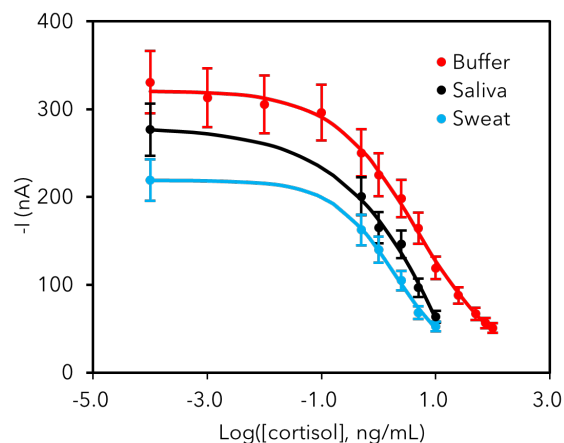


Figure 2-12. Full sigmoidal calibration curves constructed for cortisol in buffer, sweat and saliva. The sweat and saliva samples were collected from a healthy subject. Data are presented as mean \pm SD ($n = 3$).

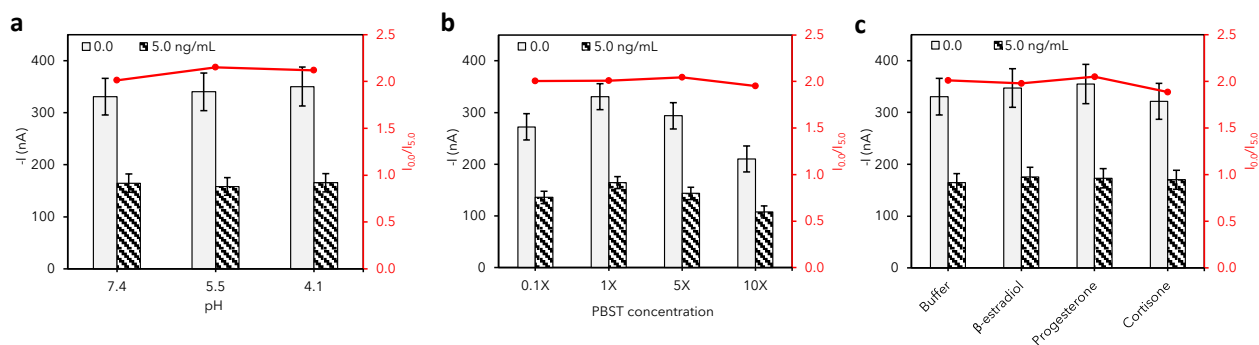


Figure 2-13. Performance characterization of the graphene-based electrochemical sensors. Effect of various pHs (a), ionic strengths (b), and presence of interferential molecules (5.0 ng/mL) (c). PBST, phosphate buffered saline with Tween[®] 20. Data are represented as mean \pm SD ($n = 3$).

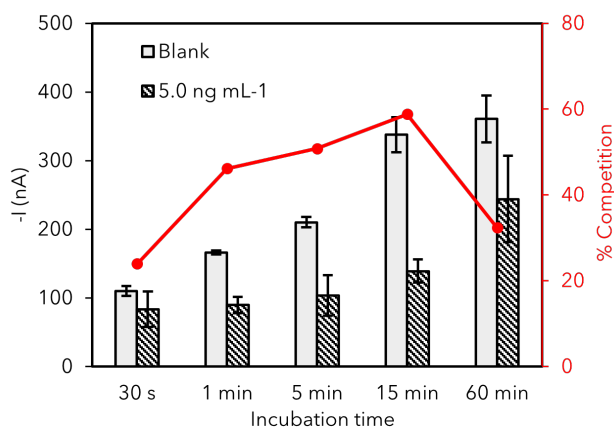


Figure 2-14. Amperometric responses and percentage competition observed for 0.0 and 5.0 ng/mL cortisol with 30-second, 1-, 5-, 15-, and 60-minute incubation. Data are presented as mean \pm SD (n = 3).

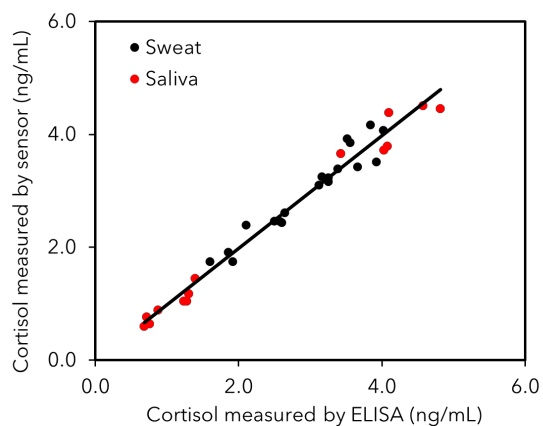


Figure 2-15. Validation of the flexible graphene-based biosensors toward cortisol monitoring in real samples with enzyme-linked immunosorbent assay (ELISA).

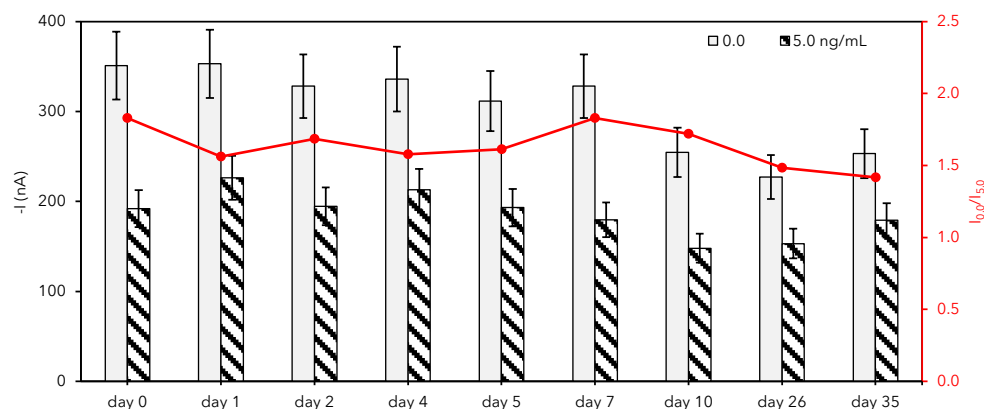


Figure 2-16. Stability test of the graphene-based electrochemical sensors. Variation of amperometric responses for 0.0 and 5.0 ng/mL cortisol with time. Data are represented as mean \pm SD (n = 3)

2.3 System Engineering of GS₄

2.2.1 Materials and Methodology

Methods

The electronic system for the integrated three-channel electrochemical analyzer was designed to be compact and efficient. A two-layer printed circuit board (PCB) (20 mm \times 35 mm \times 0.6 mm) had all the components on the top layer such that a 150 mAh 3.7 V lithium-ion polymer battery (19.75 mm \times 26 mm \times 3.8 mm) could sit comfortably underneath the PCB. The entire device is 20 mm \times 35 mm \times 7.3 mm, comparable to a USB thumb drive.

The small size, low power consumption, and rich analog peripherals of the STM32L432 ultra-low-power Arm Cortex-M4 32-bit microcontroller (MCU) enabled the compact size of the overall electronic system. The MCU had a built-in 12-bit analog-to-digital converter (ADC) and two built-in 12-bit digital-to-analog converters (DAC). When a user initiates an electrochemical measurement over Bluetooth, the built-in DACs generate a reference voltage (V_{ref}) and a working voltage (V_w) that set the potentials at the reference electrode and working electrodes through a potentiostat interface circuit. For the 3-channel amperometric measurements required for cortisol

analysis, the reference voltage was stabilized further by a low pass filter (LPF), and the three working electrodes were biased at -0.2 V relative to the reference electrode. The resultant currents flowing through each electrode were amplified and converted to voltage by transimpedance amplifiers (TIA). Three channels of the MCU's ADC were utilized to acquire concurrent amperometric measurements, and the data was transmitted to a user device over Bluetooth for further analysis.

To prepare the microfluidic module, a double-sided medical adhesive was attached to a substrate and cut through to make the channels and reservoir using a 50 W CO₂ laser cutter (Universal Laser System). Influence of mechanical deformation was investigated through incubating the sensor patch in the cortisol solutions for 15 minutes under mechanical deformation (with radii of bending curvature).

Thermal imaging of device and skin temperature

Thermal images of the sensor patch on human skin were taken by a long wave infrared thermal camera (FLIR A655sc).2.3 and 3.8 cm).

2.3.2 Results and discussion

In the GS⁴, a 3WE sensor array design with a Ag/AgCl RE and a graphene CE that provides simultaneous multichannel readings is employed. The multichannel design provides additional accuracy via signal averaging and could potentially be adapted as a hormone panel sensor for multiplexed detection of stress-related hormones. To minimize the variation of current readout due to the ohmic drop in a non-ideal electrochemical cell (**Fig. 2-17**), the reference and counter electrodes are positioned in equidistance from each working electrode with a suitable geometric design shown in **Fig. 2-18**. A microfluidic module is integrated into the flexible graphene sensor patch to enable the on-body sweat sampling and in situ cortisol recognition (**Fig. 2-18**). This design minimizes the errors caused from the sweat evaporation and skin contamination from the traditional sweat collection, leading to nearly real-time stress hormone monitoring. **Figure 2-19** illustrates block diagrams of functional units of the integrated electronic system that takes amperometric measurements from three channels concurrently, and wirelessly transmits the

acquired data to a user device over Bluetooth Low Energy (BLE). The compact device, including a 3.7 V lithium-ion polymer battery mounted underneath a printed circuit board (PCB), is 20 mm × 35 mm × 7.3 mm in dimension. Fully functioning GS⁴ drew 13.3 mA per second from a 150 mAh 3.7 V battery during an amperometric measurement, enabling 330-minute continuous amperometric measurements. The operation time can be significantly improved by incorporating the sleeping mode for the microcontroller and Bluetooth modules.

The flexible, disposable microfluidic sensor patch shows excellent mechanical flexibility and can conformally laminate on the skin (**Fig. 2-23**). To demonstrate the influence of the mechanical deformation during the on-body recognition on the cortisol determination, responses of the flexible graphene sensor patch in 1.0, 5.0, and 10.0 ng/mL cortisol solutions incubated under different bending curvatures are recorded and illustrated in **Fig. 2-24**. No apparent variations in the sensor readouts are observed with or without deformation, indicating the great mechanical and electrochemical stability toward on-body use. Considering that the actual temperature of the sensor patch during sweat collection could be significantly higher than the room temperature (**Fig. 2-25**), a temperature effect study was performed to evaluate the performance of the GS⁴. The sensors present no significant variation in the signals obtained for 0.0, 1.0 and 5.0 ng/mL cortisol under varied temperatures (25, 31, and 37 °C) (**Fig. 2-26**).

As compared to the current standard analytical methods for hormone analysis such as ELISA, the GS⁴ has distinct capabilities in multiplexed monitoring, miniaturization, short assay time (down to 1 minute vs. 80 minutes), and smaller required sample volume (<10 μL vs. 100 μL), making it an ideal platform for subsequent investigations on dynamic sweat cortisol variations and potential applications in personalized health management.

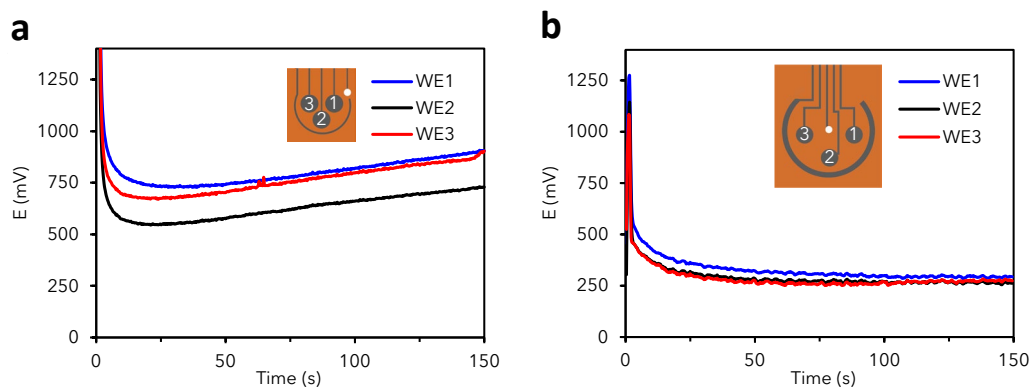


Figure 2-17. Optimization of platform design. 3-channel amperometric signals obtained with two platform designs in 1,000,000X diluted HRP-cortisol, 2.0 mM HQ and 1.0 mM H₂O₂ in 50 mM phosphate buffer (pH 6.0). The platform with asymmetric working-to-reference design (a) displays larger variations in signals obtained as compared with a symmetric design (b).

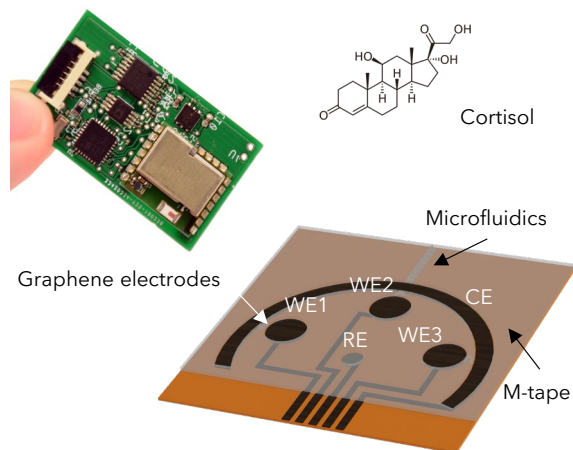


Figure 2-18. Design of the flexible microfluidic three-working electrode (3WE) sensor array for cortisol detection and photograph of the printed circuit board (PCB) with the graphene sensor patch for signal processing and wireless communication. WE, working electrode; CE, counter electrode; RE, reference electrode.

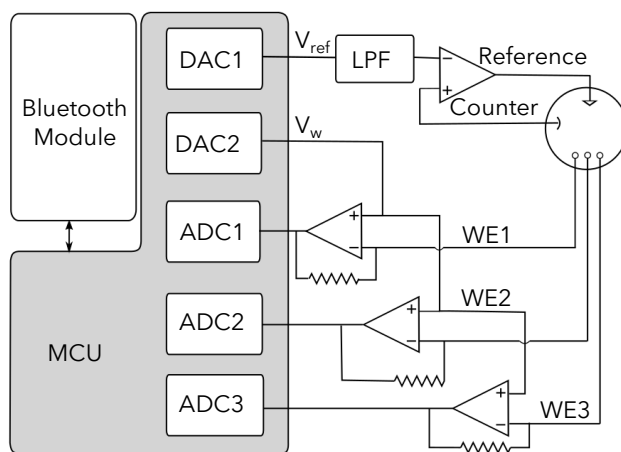


Figure 2-19. Block diagram of the GS⁴. MCU, microcontroller unit; LPF, low pass filter; DAC, digital-to-analog converter; ADC, analog-to-digital converter.

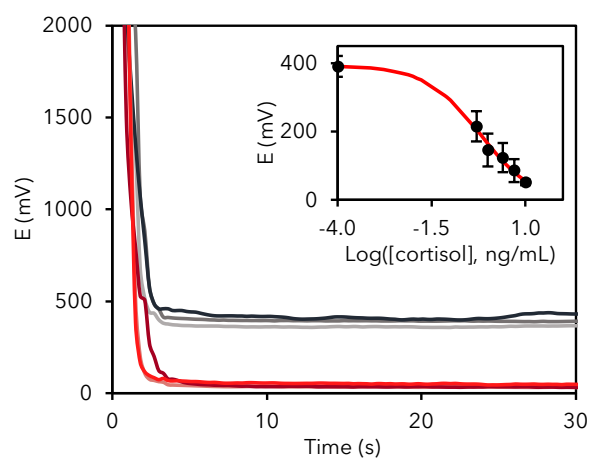


Figure 2-20. Sensor readings obtained wirelessly with the GS⁴. Data from inset are presented as mean \pm SD ($n = 3$).

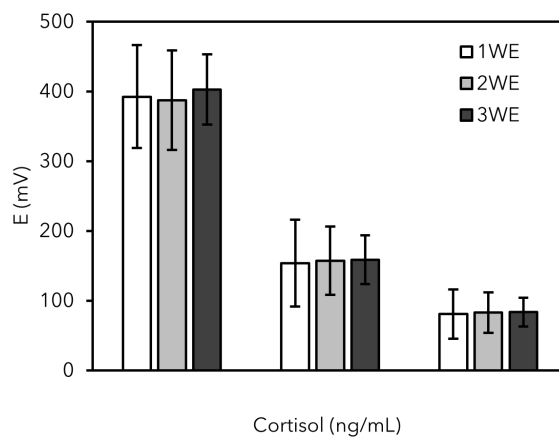


Figure 2-21. Comparison of average signals and standard deviations obtained with 1, 2, and 3 working electrodes. Data are presented as mean \pm SD (n = 8).

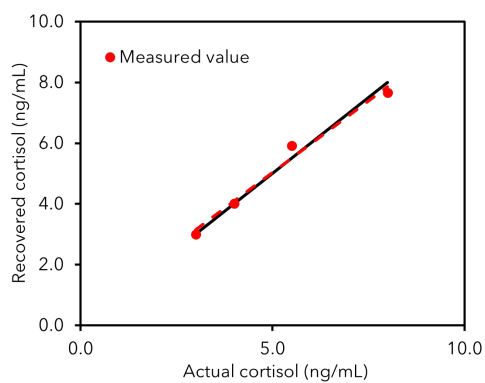


Figure 2-22. Proportional error evaluated for the GS4 based on real sample recovery studies.

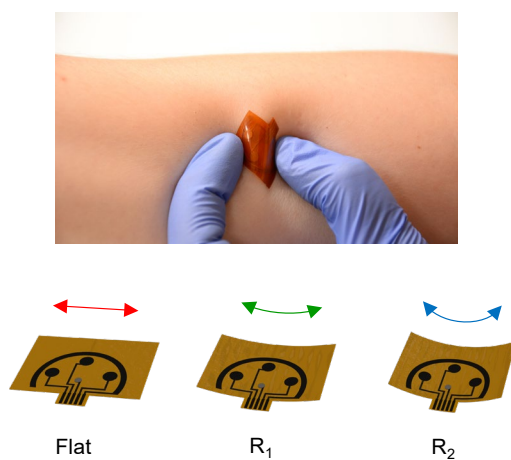


Figure 2-23. The flexible microfluidic graphene sensor array on the skin and under mechanical deformations.

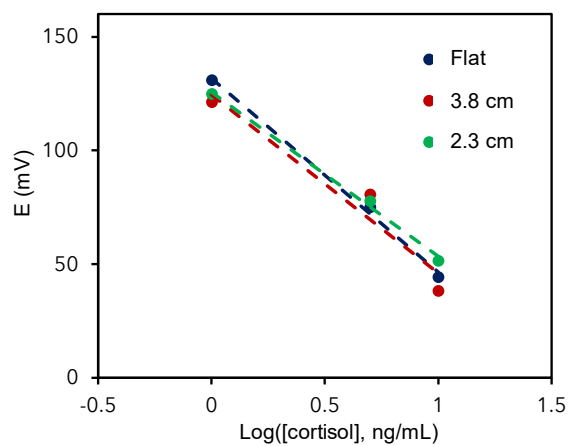


Figure 2-24. The responses of the sensor arrays with cortisol recognition under mechanical deformation (with radii of bending curvatures of 2.3 and 3.8 cm in 1.0, 5.0, and 10.0 ng/mL cortisol).

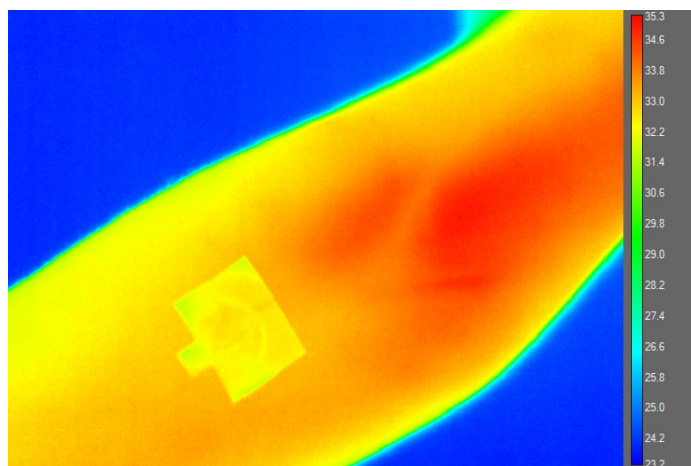


Figure 2-25. Thermal image of the sensor patch on human forearm.

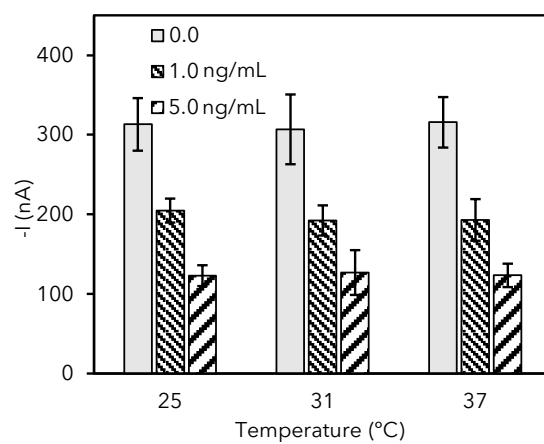


Figure 2-26. Influence of temperature on sensor performance. Amperometric responses for 0.0, 1.0 and 5.0 ng/mL cortisol incubated at room temperature (25 °C), 31 °C and 37 °C. Data are represented as mean \pm SD (n = 3).

2.4 Investigation of the circadian rhythm and stress responses of sweat cortisol

2.4.1 Methods

Subjects and procedures

The performance of the GS4 was evaluated in human sweat, saliva and sweat samples from the human subjects in compliance with the protocols that were approved by the institutional review board (IRB) (No. 19-0895 and No. 19-0892) at California Institute of Technology (Caltech). The participating subjects (twelve healthy subjects, age range 18–65) were recruited from Caltech campus and the neighboring communities through advertisement by posted notices, word of mouth, and email distribution. All subjects gave written, informed consent before participation in the study.

Circadian rhythm study

Four healthy subjects who reported regular sleep-wake rhythm and no sleep disturbances participated in this study. Subjects were informed to refrain from food intake at least 30 minutes before reporting to the laboratory. On experimental day, subjects reported to the laboratory at 8:00 AM and at 7:00 PM on the same day for sweat, saliva and capillary blood collection. Sweat stimulation was performed with a Model 3700 Macroduct[®] by placing two electrodes on the pre-cleaned forearm region of the subject. After their connection to the source, a 1.5 mA current was applied for 5 minutes and secreted sweat was sampled for a period of 40 minutes and then analyzed. During the sweat sampling and test, fresh capillary blood and saliva were collected from subject immediately after sweat stimulation following the protocol described in the sample processing section.

Physiological stress response — stationary biking study

Three untrained participants and one trained participant were involved in this study. The trained subject (an athlete from a Caltech sport team) exercised regularly for at least 9 hours per week while the untrained subjects had an average of 1 hour of exercise per week. Constant workload physical activity trials were performed in the morning (ranging from 8:00 to 10:00, denoted as AM)

or afternoon (from 5:00 to 7:00, denoted as PM) in an ergometer stationary bike (Kettler Axos Cycle M-LA). Subjects were informed to refrain from food intake at least 30 minutes before the exercise. Subjects were asked to bike for 50 minutes at a constant speed of 60 revolutions per minute (rpm) and sweat samples were collected every 10 minutes from the forehead. Before starting the aerobic trial, and after sweat sampling and analysis at each time interval, participants' foreheads were cleaned with alcohol swabs and gauze. Blood collection were performed before the stationary bike exercise and immediately after the exercise following the procedures described in sample processing protocol section.

Physiological stress response — cold pressor test

Four participants were exposed to standard CPT in the afternoon (between 5:00 to 7:00 PM) in order to control for the diurnal cortisol cycle. The experimental procedure was initiated by collecting sweat through iontophoresis for a period of 8 minutes. At the same time, saliva and capillary blood sample from each participant were collected with the purpose of determining baseline values. Subsequently, recruited volunteers immersed their non-dominant hand up to the wrist in a plastic tank containing cold-water (2 °C) for 3 minutes (CPT) and after the immersion time they were instructed to remove the hand from the ice-water. Sweat, saliva and capillary blood were collected following the detailed protocols at different resting periods after CPT test (8, 16, and 24 minutes).

Saliva and blood sample processing protocol

After rinsing mouth with water, volunteers deposited saliva in 1.5 mL Eppendorf tubes which were subsequently centrifuged (10000 rpm, 10 minutes) and analyzed. Fresh capillary blood samples were collected at same periods of time as saliva using a finger-prick approach. After cleaning the fingertip with alcohol wipe and allowing it to air dry, the skin was punctured with CareTouch lancing device. Samples were collected with 1.5 mL Eppendorf tubes after wiping off the first drop of blood with gauze. Once standardized clotting procedure finished, serum was separated by centrifuging at 3575 rpm for 15 minutes, and instantly stored at -20 °C.

2.4.2 Results and Discussion

Cortisol presents a distinct and robust diurnal pattern, which peaks shortly after awakening and declines throughout the day in plasma⁴⁰ and saliva.⁴¹ Early report shows that sweat contains cortisol level comparable to those reported in saliva;⁴² we postulate that, circulating cortisol molecules are transported to and stored in eccrine and apocrine glands, secreted into the sweat, and ultimately excreted through a sweat pore to the epidermal surface.⁴³ It is, therefore, reasonable to hypothesize that cortisol level in sweat might present similar circadian rhythm regulated by the internal clock and light/dark cycle (**Fig. 2-27**). Considering that circadian pattern of circulating cortisol is highly informative for a number of mental health conditions,^{8,9} the fluctuations of the ultra-low levels of sweat cortisol are investigated with the graphene platform through a pilot human study. Sweat was sampled with iontophoretic sweat stimulation as illustrated in **Fig. 2-28**.

Fig. 2-29 illustrates the reproducible patterns obtained from an exploratory study by monitoring the sweat cortisol variations of a healthy subject in a period of six days. High morning (AM) cortisol level and low afternoon (PM) level are observed each day; such rhythm resembles diurnal cycles of circulating cortisol in blood. In order to further characterize the correlation between sweat and circulating cortisol levels, sweat in the early AM and in the late PM from four healthy subjects are analyzed along with saliva and serum. A similar trend in AM/PM cortisol variations modulated by circadian rhythm are observed from all the samples (**Fig. 2-30**), with the ratios ranging from 1.35 to 2.00. Although several studies explored the correlation of cortisol found in various biofluids including blood, urine, and saliva,⁴⁴⁻⁴⁶ the relationship between sweat and circulating cortisol levels, to the best of our knowledge, has barely been explored. A positive correlation between sweat cortisol and serum cortisol (Pearson's correlation coefficient $r = 0.87$) (**Fig. 2-31**) is obtained based on data collected from eight healthy subjects. Similarly, the correlation coefficient between sweat cortisol and salivary cortisol is determined to be 0.78 (**Fig. 2-32**). Although the number of real samples analyzed is limited in this exploratory study, empirical evidence suggests strong correlation exists between sweat cortisol and serum cortisol.

Dynamic cortisol response to stress stimuli

In addition to long-term profiling of the diurnal cycles, cortisol response to acute stressors contains abundant information for psychoneurological investigations,^{47,48} and plays a critical role in human performance monitoring and management.¹ For instance, sensitization of the HPA axis to external stimuli is another critical factor that distinguishes PTSD from other psychiatric disorders.⁸ Next, we set out to investigate if sweat analysis of cortisol presents meaningful changes to acute stress of the human subjects induced by different stressors in a short time frame.

Aerobic exercises such as running and cycling are potent stimuli/stressor of cortisol secretion.⁴⁹ In this study, a 50-minute stationary cycling exercise at a constant workload is employed for sweat cortisol content analysis (**Fig. 2-33a**). Sweat sampling and analysis are performed with the GS⁴ sequentially at 10-minute intervals for the 50-minute constant-load exercise in a cycling ergometer from three physically untrained and one trained (athletic) subjects. In addition, serum cortisol levels before and immediately after the cycling exercise are analyzed to validate if sweat cortisol variation is in accordance with circulating cortisol levels. For all subjects under study, sweat cortisol increases progressively and reaches the highest level after 40 minutes of continuous biking. From this point, a slight decrease in cortisol level is detected near the end of the exercise in all participants and more significantly in subject 4 (athlete) (**Fig. 2-33b**). Cortisol contents in pre- and post-exercise serum samples present good correlation to the change in cortisol from the beginning of the perspiration (10 minutes) to the end of the exercise (50 minutes) (**Fig. 2-33c**). The dynamic sweat hormone profiles observed for untrained subjects are similar to reported trends of serum cortisol after high-intensity exercise,⁵⁰ indicating the activation of HPA by physical exercise. In contrast, the blunted cortisol response observed in the trained subject reflects exercise-induced adaptation. This is consistent with previous reports that trained individuals likely perceived the given workload as a smaller stressor and demonstrate a lower degree of HPA activation in response to physical stressors⁵¹ as well as psychosocial stimuli.⁵²

Noting that circadian patterns in sweat cortisol level give rise to different baseline before stress stimulation, cortisol variations in sweat for physical exercises conducted in the morning and in the afternoon for the same subjects are studied. Sweat cortisol levels are analyzed from two subjects in the beginning of the perspiration and in the end of the cycling (**Fig. 2-34**). Significantly

increased sweat cortisol levels are observed at 50 minutes as compared to that at 10 minutes, in response to the physiological stressor. Cortisol level for the first time point is higher in the AM than in the PM for both subjects; higher relative percentage change of cortisol is observed in the PM exercise. This relation is in agreement with the diurnal sweat cortisol variation we observed in the circadian rhythm study, similar to a previous report that shows the circadian rhythm of serum and salivary cortisol could confound the magnitude of cortisol responses.⁵³ These results reveal the importance of baseline construction in offsetting circadian baseline in the context of short-term dynamic sweat cortisol stress response. Point-of-care and wearable devices-enabled sweat analysis could conveniently facilitate personalized baseline construction as discussed for the circadian rhythm study.

To study the response time frame of sweat cortisol to acute stressors, an exploratory cold pressor test (CPT) was performed on four subjects. Subjects were asked to immerse their non-dominant hand in ice water for 3 minutes (**Fig. 2-35a**). CPT is a reliable acute physiological stressor that triggers immediate HPA axis activation and significant cortisol release.⁵⁴ Sweat was sampled at 8-minute interval with iontophoretic sweat stimulation as illustrated in Figure S10. Sweat dynamic cortisol profile was evaluated in each case and we observed that cortisol increased after completion of CPT, reaching the mean peak between 8 and 16 minutes after CPT (**Fig. 2-35b**). Similar trends were also observed for serum (**Fig. 2-35c**) and salivary cortisol (**Fig. 2-36**); the former collected and tested before starting the experiment (denoted as baseline), 8 and 24 minutes after CPT. These observations are consistent with previously reported CPT studies for cortisol and other hormones release evaluation in serum⁵⁵ and saliva.⁵⁶ The sweat cortisol profiles presented small to negligible time lag as compared with serum cortisol trends in literature,⁵⁷⁻⁵⁹ revealing the promptness of sweat cortisol as a quasi-real-time stress indicator. Furthermore, given the clinical applicability of CPT for pain tolerance evaluation,⁶⁰ sweat stress hormones sensors may serve as an attractive quantification approach in pain perception studies.

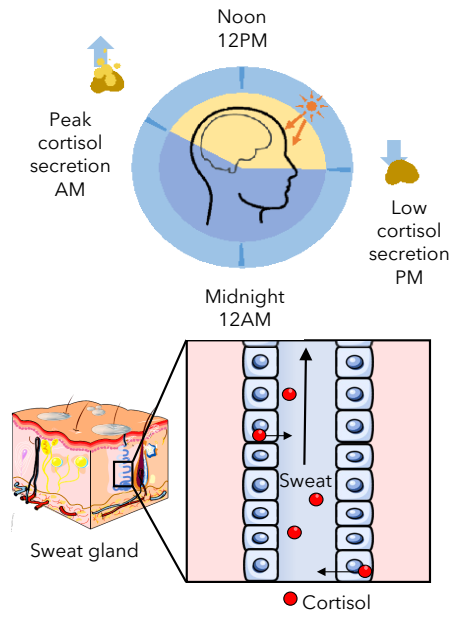


Figure 2-27. Conceptual illustration of the light/dark-cycle regulated cortisol circadian rhythm and the transport of circulating cortisol to sweat.

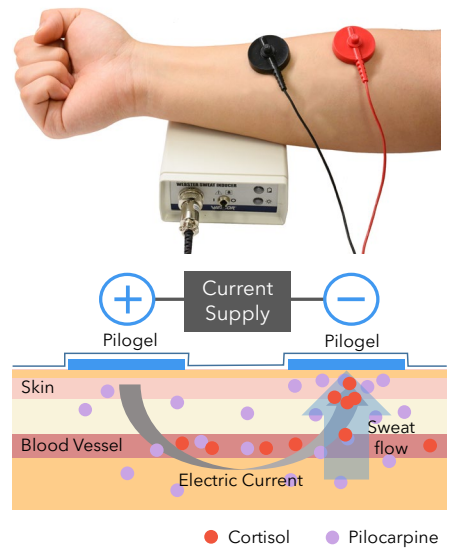


Figure 2-28. Iontophoresis based sweat sampling. Illustration of iontophoresis-assisted sweat stimulation on a subject's forearm, and principles of sweat stimulation and cortisol excretion in sweat.

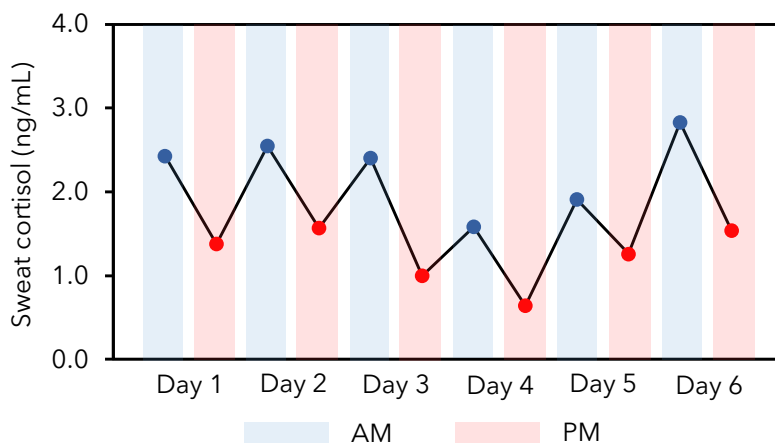


Figure 2-29. Circadian rhythm of sweat cortisol constructed for a healthy subject in a period of 6 days. Sweat was sampled and analyzed in the morning (AM) and in the afternoon (PM) each day.

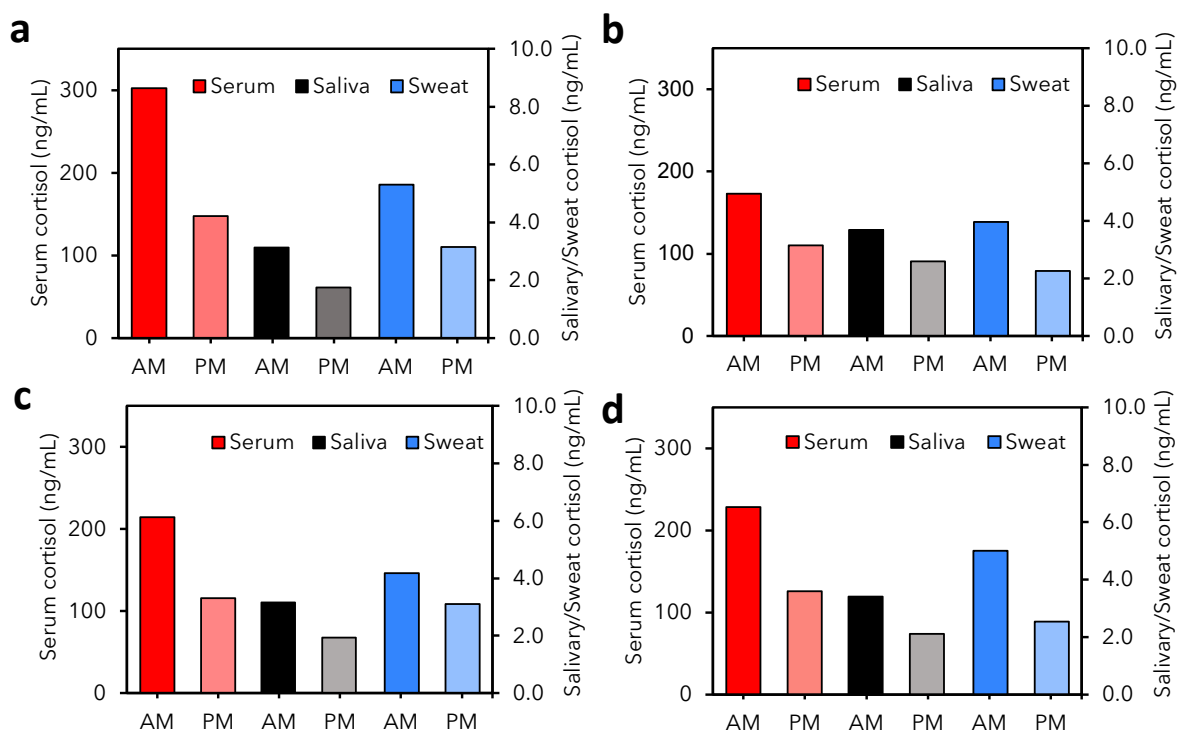


Figure 2-30. Cortisol levels found in serum, saliva and sweat sampled in the AM and in the PM from four healthy subjects.

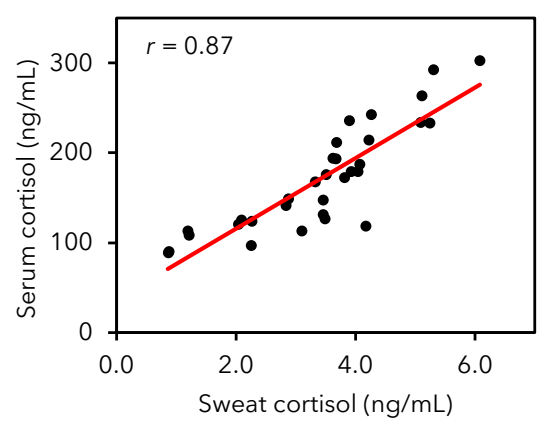


Figure 2-31. Correlation of serum cortisol to sweat cortisol. The correlation coefficient r was acquired through Pearson’s correlation analysis (eight subjects, $n = 4$ for each subject, $p < 0.001$).

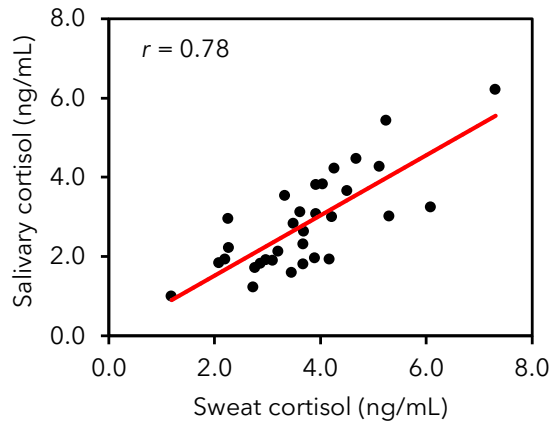


Figure 2-32. Correlation of salivary cortisol to sweat cortisol. The correlation coefficient r was acquired through Pearson’s correlation analysis (eight subjects, $n = 4$ for each subject, $p < 0.001$).

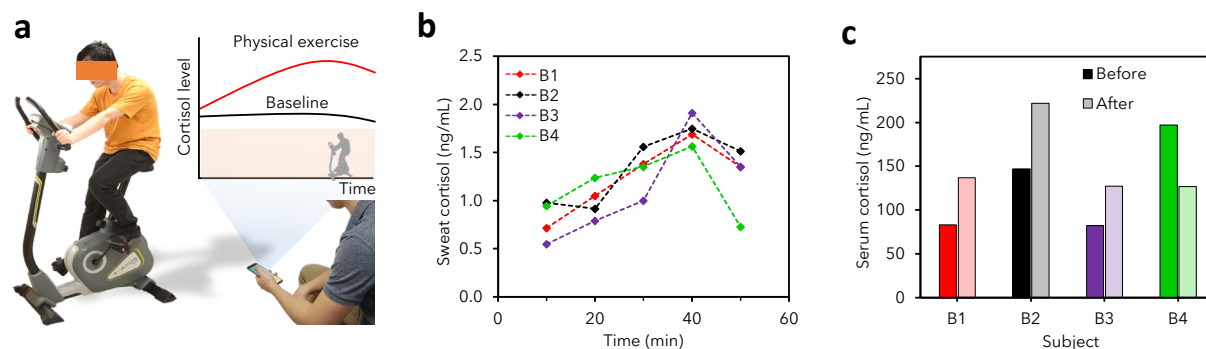


Figure 2-33. Dynamic monitoring of exercise stress response using the GS4. **a**, Conceptual illustration of stress response monitoring by tracking of a subject's cortisol level with data wirelessly transmitted to a cell phone via Bluetooth. Physical exercise is utilized as a stressor. **b**, Cortisol monitoring from three physically untrained subjects (B1-B3) and one trained subject (B4) in a constant load cycling exercise. **c**, Cortisol levels in serum sampled and analyzed before and after the cycling exercise for four subjects.

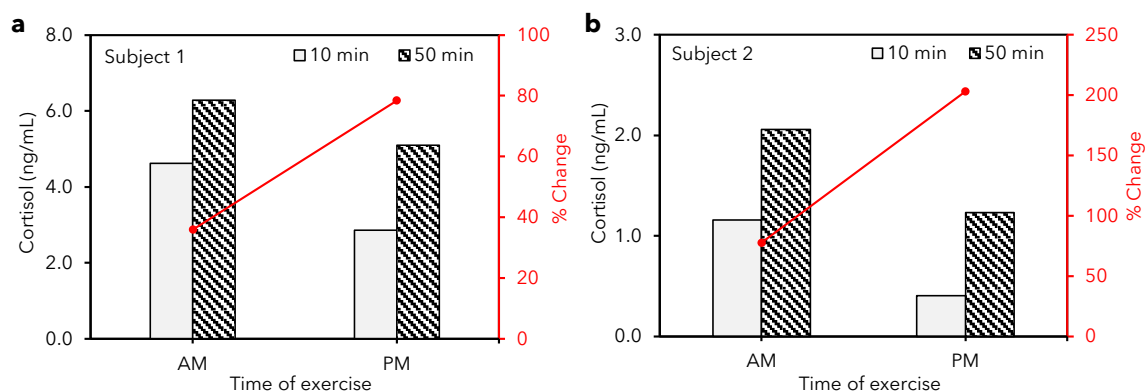


Figure 2-34. Influence of time of exercise in cortisol variation. Cortisol level evaluated in sweat and its relative percentage change of two healthy subjects before and after physical exercise conducted in the morning (AM) and in the afternoon (PM).

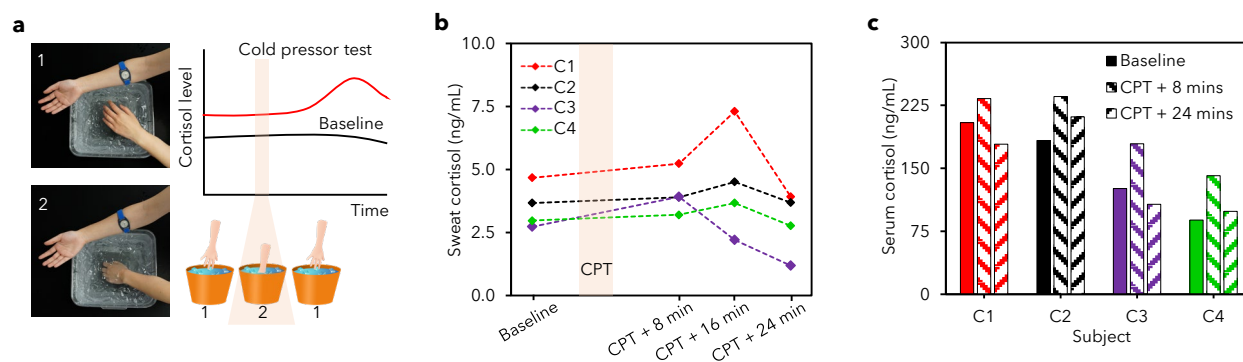


Figure 2-35. Dynamic monitoring of acute stress response to cold pressor test using the GS4.

a, Illustration of stress response in relation to the timeframe of cold pressor test (CPT) performed.

b, Cortisol monitoring from four subjects (C1-C4) undergoing CPT. Dynamic cortisol response was evaluated with iontophoresis sweat from forearm sampled and analyzed at 10-minute intervals.

c, Cortisol levels in serum sampled before, 8 minutes after, and at the end of the CPT experiment.

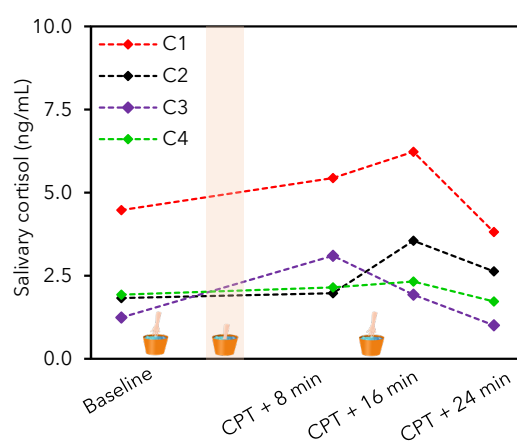


Figure 2-36. Salivary cortisol at several time points across the cold pressor test for four subjects (C1-C4) from the human study presented in Fig. 2-35.

2.5 Conclusion

This chapter demonstrates the potential of sweat hormone analysis enabled by an integrated portable system – the GS⁴. Highly sensitive, selective, and efficient stress hormone sensing was achieved through a unique combination of the laser-induced graphene and immunosensing. The

assay time could be as low as 1 minute. Using this graphene-based wireless sensing platform, we have demonstrated that relevant information crucial to stress response and adaptation analysis could be extracted from cortisol excreted in sweat. The low-cost and mass-produced graphene sensor arrays enabled us to conduct several meaningful stress-related physiological studies. To the best of our knowledge, the results we present here represent the first demonstration of cortisol diurnal cycle and the dynamic stress response profile constructed from human sweat. On a longer timescale, characteristic cortisol circadian rhythms could be monitored; in a short time frame, acute external stimuli triggered stress response could be analyzed.

Sweat's accessibility to wearable continuous monitoring devices and its minimal invasiveness enables the construction of long-term and comprehensive cortisol diurnal patterns. To date, many clinical studies on psychological disorders-triggered cortisol circadian rhythms variation rely heavily on data collected at sparsely spaced plasma or saliva cortisol sampling timing^{61,62} whereas those with narrow sampling intervals were achieved with intravenous catheters;⁶³ confirmation of cortisol circadian rhythms in sweat might revolutionize clinical research and mental health monitoring paradigm for both clinicians and patients in the near future.

The possibility of continuous dynamic stress response profiling with sweat sensors offers new opportunities for fundamental psychoneuroendocrinology studies and timely documentation of stress level for day-to-day mental health monitoring. Although only physical stress stimuli were investigated in the present study, given the fact that psychosocial stress stimuli trigger similar neuroendocrine and behavioral responses regulated by HPA axis,³ similar information may be extracted from sweat cortisol in response to psychosocial stresses. The good correlation with circulating hormones, the diurnal cycle, and dynamic stress response profile demonstrated in this study using our integrated sensing approach will lead the next wave of technological advancement in personalized human performance and mental health management.

Bibliography of Chapter 2

1. Mariotti, A. The effects of chronic stress on health: New insights into the molecular mechanisms of brain–body communication. *Future Science OA* **1**, FSO23 (2015).

2. Cohen, S., Janicki-Deverts, D., and Miller, G. E. Psychological stress and disease. *Journal of the American Medical Association* **298**, 1685–1687 (2007).
3. Kogler, L. *et al.* Psychosocial versus physiological stress — Meta-analyses on deactivations and activations of the neural correlates of stress reactions. *NeuroImage* **119**, 235–251 (2015).
4. Herman, J. P. *et al.* B. Regulation of the hypothalamic-pituitary-adrenocortical stress response. *Comprehensive Physiology* **6**, 603–621 (2016).
5. Nicolson, N. A. and Csikszentmihalyi, M. “Stress, coping and cortisol dynamics in daily life,” in *The Experience of Psychopathology: Investigating Mental Disorders in their Natural Settings* (ed. de Vries, M. W.), 219–232 (Cambridge University Press, 1992).
6. Sladek, M. R., Doane, L. D., and Stroud, C. B. Individual and day-to-day differences in active coping predict diurnal cortisol patterns among early adolescent girls. *Journal of Youth and Adolescence* **46**, 121–135 (2016).
7. Verhagen, S. J. W. *et al.* Use of the experience sampling method in the context of clinical trials. *Evidence-Based Mental Health* **19**, 86–89 (2016).
8. Yehuda, R. Sensitization of the hypothalamic-pituitary-adrenal axis in posttraumatic stress disorder. *Annals of the New York Academy of Sciences* **821**, 57–75 (1997).
9. Herbert, J. Cortisol and depression: Three questions for psychiatry. *Psychological Medicine* **43**, 449–469 (2012).
10. Bos, R. V. D., Harteveld, M., and Stoop, H. Stress and decision-making in humans: Performance is related to cortisol reactivity, albeit differently in men and women. *Psychoneuroendocrinology* **34**, 1449–1458 (2009).
11. Rodrigues, S. M., Ledoux, J. E., and Sapolsky, R. M. The influence of stress hormones on fear circuitry. *Annual Review of Neuroscience* **32**, 289–313 (2009).
12. Uum, S. H. M. V. *et al.* Elevated content of cortisol in hair of patients with severe chronic pain: A novel biomarker for stress. *Stress* **11**, 483–488 (2008).
13. Kim, J., Campbell, A. S., Ávila, B. E.-F. D., and Wang, J. Wearable biosensors for healthcare monitoring. *Nature Biotechnology* **37**, 389–406 (2019).

14. Nakata, S. *et al.* A wearable pH sensor with high sensitivity based on a flexible charge-coupled device. *Nature Electronics* **1**, 596–603 (2018).
15. Lee, H. *et al.* A graphene-based electrochemical device with thermoresponsive microneedles for diabetes monitoring and therapy. *Nature Nanotechnology* **11**, 566–572 (2016).
16. Lee, H. *et al.* Wearable/disposable sweat-based glucose monitoring device with multistage transdermal drug delivery module. *Science Advances* **3**, e1601314 (2017).
17. Han, S. *et al.* Battery-free, wireless sensors for full-body pressure and temperature mapping. *Science Translational Medicine* **10**, eaan4950 (2018).
18. Yang, Y. and Gao, W. Wearable and flexible electronics for continuous molecular monitoring. *Chemical Society Reviews* **48**, 1465–1491 (2019).
19. Bariya, M., Nyein, H. Y. Y., and Javey, A. Wearable sweat sensors. *Nature Electronics* **1**, 160–171 (2018).
20. Reeder, J. T. *et al.* Waterproof, electronics-enabled, epidermal microfluidic devices for sweat collection, biomarker analysis, and thermography in aquatic settings. *Science Advances* **5**, eaau6356 (2019).
21. Bhandodkar, A. J. *et al.* Battery-free, skin-interfaced microfluidic/electronic systems for simultaneous electrochemical, colorimetric, and volumetric analysis of sweat. *Science Advances* **5**, eaav3294 (2019).
22. Zhu, C. *et al.* Stretchable temperature-sensing circuits with strain suppression based on carbon nanotube transistors. *Nature Electronics* **1**, 183–190 (2018).
23. Boutry, C. M. *et al.* Biodegradable and flexible arterial-pulse sensor for the wireless monitoring of blood flow. *Nature Biomedical Engineering* **3**, 47–57 (2019).
24. Son, D. *et al.* An integrated self-healable electronic skin system fabricated via dynamic reconstruction of a nanostructured conducting network. *Nature Nanotechnology* **13**, 1057–1065 (2018).
25. Gao, W. *et al.* Fully integrated wearable sensor arrays for multiplexed in situ perspiration analysis. *Nature* **529**, 509–514 (2016).

26. Choi, J. *et al.* Soft, Skin-integrated multifunctional microfluidic systems for accurate colorimetric analysis of sweat biomarkers and temperature. *ACS Sensors* **4**, 379–388 (2019).
27. Heikenfeld, J. *et al.* Accessing analytes in biofluids for peripheral biochemical monitoring. *Nature Biotechnology* **37**, 407–419 (2019).
28. Kim, J. *et al.* Noninvasive alcohol monitoring using a wearable tattoo-based iontophoretic-biosensing system. *ACS Sensors* **1**, 1011–1019 (2016).
29. Tai, L.-C. *et al.* Methylxanthine drug monitoring with wearable sweat sensors. *Advanced Materials* **30**, 1707442 (2018).
30. Emaminejad, S. *et al.* Autonomous sweat extraction and analysis applied to cystic fibrosis and glucose monitoring using a fully integrated wearable platform. *Proceedings of the National Academy of Sciences of the United States of America* **114**, 4625–4630 (2017).
31. Kinnamon, D. *et al.* Portable biosensor for monitoring cortisol in low-volume perspired human sweat. *Scientific Reports* **7**, 13312 (2017).
32. Parlak, O. *et al.* Molecularly selective nanoporous membrane-based wearable organic electrochemical device for noninvasive cortisol sensing. *Science Advances* **4**, eaar2904 (2018).
33. Shao, Y. *et al.* Graphene based electrochemical sensors and biosensors: A review. *Electroanalysis* **22**, 1027–1036 (2010).
34. Wang, X. *et al.* Competitive immunoassays for the detection of small molecules using single molecule arrays. *Journal of the American Chemical Society* **140**, 18132–18139 (2018).
35. Findlay, J. W. A. and Dillard, R. F. Appropriate calibration curve fitting in ligand binding assays. *The AAPS Journal* **9**, E260–E267 (2007).
36. Jia, M. *et al.* Quantification of cortisol in human eccrine sweat by liquid chromatography – tandem mass spectrometry. *Analyst* **141**, 2053–2060 (2016).
37. Miller, R. *et al.* Comparison of salivary cortisol as measured by different immunoassays and tandem mass spectrometry. *Psychoneuroendocrinology* **38**, 50–57 (2013).

38. Khan, M. S. *et al.* Paper-based analytical biosensor chip designed from Graphene-nanoplatelet-amphiphilic-diblock-co-polymer composite for cortisol detection in human saliva. *Analytical Chemistry* **89**, 2107–2115 (2017).
39. Laudat, M. H. *et al.* Salivary cortisol measurement: A practical approach to assess pituitary-adrenal function. *Journal of Clinical Endocrinology & Metabolism*, **66**, 343–348 (1988).
40. Oster, H. *et al.* The functional and clinical significance of the 24-h rhythm of circulating glucocorticoids. *Endocrine Reviews*, **38**, 3–45 (2016).
41. Ivars, K. *et al.* Development of salivary cortisol circadian rhythm and reference intervals in full-term infants. *PLOS One*, **10**, e0129502 (2015).
42. Russell, E. *et al.* The detection of cortisol in human sweat. *Therapeutic Drug Monitoring*, **36**, 30–34 (2013).
43. Katchman, B. A. *et al.* Eccrine sweat as a biofluid for profiling immune biomarkers. *Proteomics - Clinical Applications*, **12**, 1800010 (2018).
44. Burke, P. M. *et al.* Correlation between serum and salivary cortisol levels in depressed and nondepressed children and adolescents. *American Journal of Psychiatry* **142**, 1065–1067 (1985).
45. Vanbruggen, M. D. *et al.* The relationship between serum and salivary cortisol levels in response to different intensities of exercise. *International Journal of Sports Physiology and Performance* **6**, 396–407 (2011).
46. Jung, C. *et al.* Plasma, salivary and urinary cortisol levels following physiological and stress doses of hydrocortisone in normal volunteers. *BMC Endocrine Disorders* **14**, 91 (2014).
47. Dickerson, S. S. and Kemeny, M. E. Acute stressors and cortisol responses: a theoretical integration and synthesis of laboratory research. *Psychological Bulletin* **130**, 355–391 (2004).
48. Kudielka, B. M. and Wüst, S. Human models in acute and chronic stress: Assessing determinants of individual hypothalamus–pituitary–adrenal axis activity and reactivity. *Stress* **13**, 1–14 (2010).

49. Kanaley, J. A. Cortisol and growth hormone responses to exercise at different times of day. *Journal of Clinical Endocrinology and Metabolism* **86**, 2881–2889 (2001).
50. Weise, M. *et al.* Stress dose of hydrocortisone is not beneficial in patients with classic congenital adrenal hyperplasia undergoing short-term, high-intensity exercise. *Journal of Clinical Endocrinology and Metabolism* **89**, 3679–3684 (2004).
51. Luger, A. *et al.* Acute hypothalamic–pituitary–adrenal responses to the stress of treadmill exercise. *New England Journal of Medicine* **316**, 1309–1315 (1987).
52. Rimmele, U. *et al.* Trained men show lower cortisol, heart rate and psychological responses to psychosocial stress compared with untrained men. *Psychoneuroendocrinology* **32**, 627–635 (2007).
53. Thuma, J. R. *et al.* Circadian rhythm of cortisol confounds cortisol responses to exercise: Implications for future research. *Journal of Applied Physiology* **78**, 1657–1664 (1995).
54. Schwabe, L., Haddad, L., and Schachinger, H. HPA axis activation by a socially evaluated cold-pressor test. *Psychoneuroendocrinology* **33**, 890–895 (2008).
55. Zimmer, C. *et al.* Sex differences in cortisol response to noxious stress. *Clinical Journal of Pain* **19**, 233–239 (2003).
56. Goodin, B. R. *et al.* Poor sleep quality and exaggerated salivary cortisol reactivity to the cold pressor task predict greater acute pain severity in a non-clinical sample. *Biological Psychology* **91**, 36–41 (2012).
57. McRae, A. L. *et al.* Stress reactivity: Biological and subjective responses to the cold pressor and Trier Social stressors. *Human Psychopharmacology* **21**, 377–385 (2006).
58. Bullinger, M. *et al.* Endocrine effects of the cold pressor test: Relationships to subjective pain appraisal and coping. *Psychiatry Research* **12**, 227–233 (1984).
59. Geliebter, A. *et al.* Plasma cortisol levels in response to a cold pressor test did not predict appetite or ad libitum test meal intake in obese women. *Appetite* **59**, 956–959 (2012).
60. Mitchell, L. A., MacDonald, R. A., and Brodie, E. E. Temperature and the cold pressor test. *Journal of Pain* **5**, 233–237 (2004).

61. Machale, S., Cavanagh, J. T., Bennie, J., Carroll, S., Goodwin, G. M., and Lawrie, S. M. Diurnal variation of adrenocortical activity in chronic fatigue syndrome. *Neuropsychobiology* **38**, 213–217 (1998).
62. Strickland, P. *et al.* comparison of salivary cortisol in chronic fatigue syndrome, community depression, and healthy controls. *Journal of Affective Disorders* **47**, 191–194 (1998).
63. Vythilingam, M. *et al.* Low early morning plasma cortisol in posttraumatic stress disorder is associated with co-morbid depression but not with enhanced glucocorticoid feedback inhibition. *Psychoneuroendocrinology* **35**, 442–450.

Chapter 3

A WEARABLE SWEAT SENSOR FOR SYSTEMIC INFLAMMATION MONITORING

Materials from this chapter appear in “Tu, J.; Min, J.; Song, Y.; Xu, C.; Li, J.; Moore, J.; Hanson, J.; Hu, E.; Parimon, T.; Wang, T.-Y.; Davoodi, E.; Chou, T.-F.; Chen, P.; Hsu, J. J.; Rossiter, H. B.; Gao, W. A wireless patch for the monitoring of C-reactive protein in sweat. *Nature Biomedical Engineering* 14 (2023) doi:10.1038/s41551-023-01059-5.”

3.1 Introduction

Inflammatory processes and immune responses are associated with a broad spectrum of physical and mental disorders that contribute substantially to modern morbidity and mortality globally. The top three leading causes of death worldwide, namely, ischemic heart disease, stroke, and chronic obstructive pulmonary disease (COPD), are each characterized by chronic inflammation¹⁻³. Although the acute inflammatory response is a critical survival mechanism, chronic inflammation contributes to long-term silent progression of disease through irreversible tissue damage⁴⁻⁶. Delayed diagnosis and treatment of chronic diseases impose heavy financial burdens on patients and the healthcare systems^{2,4}. A readily available means of monitoring inflammatory biomarkers at home could improve patient outcomes and lower cost factors by monitoring disease progression and initiating early treatment and intervention⁷.

Although there is no canonical standard biomarker for the measurement and prediction of systemic chronic inflammation⁶, C-reactive protein (CRP), an acute-phase protein synthesized by hepatocytes in response to a wide range of both acute and chronic stimuli, has a close association with chronic inflammation and respective risks of mortality in several disease states (**Fig. 3-1a**)⁸⁻¹². The stable nature of CRP in plasma, the absence of circadian variation, and its insensitivity to common medications such as corticosteroids render it extremely attractive to clinicians as a handy means to assess a patient's physiological inflammatory state¹³. There is also a growing interest in exploring the effectiveness of serial CRP measurements for therapeutic decision-making^{14,15}.

At present, circulating CRP levels are clinically assessed in specific laboratories that rely on invasive blood draws from patients (**Appendix A, Table A-1**). Commercial point-of-care CRP monitors are still bulky in size and cannot reach picomolar-level sensitivity to assess CRP levels in non-invasively accessible alternative biofluids such as sweat and saliva (**Appendix A, Table A-2**). A faster, sensitive, non-invasive, and user-friendly approach, accessible to not only clinicians but also patients and caregivers, could unleash the full potential of inflammatory biomarker monitoring for clinical management beyond hospital settings.

Recent advances in flexible electronics and digital health have transformed conventional laboratory tests into remote wearable molecular sensing that enables real-time monitoring of

physiological biomarkers^{16–24}. Sweat contains abundant biochemical molecules ranging from electrolytes and metabolites, to large proteins^{25,26}, and importantly, it is readily accessible by non-invasive techniques (**Fig. 3-1a**). However, currently reported wearable biosensors are largely restricted to the detection of a limited selection of biomarkers such as electrolytes and metabolites at μM or greater concentrations *via* ion-selective and enzymatic sensors or direct oxidation/reduction^{16,20,27–40}. The majority of clinically relevant protein biomarkers including CRP are present at nM to pM levels in blood while the anticipated levels of proteins in sweat are expected to be much lower than in blood²⁶. Despite recent efforts in the development of wearable bioaffinity biosensors for trace-level biomarkers such as cortisol, the accurate and *in situ* detection of sweat protein biomarkers remains a major challenge due to their extremely low concentrations (pM level) and the large interpersonal and intrapersonal variations in sweat compositions^{41–44}. The detection of protein biomarkers usually requires integrating bioaffinity receptors such as antibodies and aptamers^{43,45}. However, such techniques typically require lengthy target incubation, labor-intensive washing steps, and the addition of redox solutions for signal transduction. Thus, there is a strong desire for a wearable biosensing technology that allows automatic *in situ* monitoring of ultra-low-level circulating proteins at home and in community settings.

In this work, we report a wireless wearable nanobiosensor, InflaStat, for non-invasive personalized inflammatory status monitoring (**Fig. 3-1b-e**). It consists of an autonomous iontophoresis module for on-demand and controlled sweat extraction, a sweat gland-powered skin-interfaced microfluidic module that capitalizes on sweat flow to achieve fully automated protein and detector antibody capturing, subsequent washing, and picomolar-level electrochemical detection on the skin, and a flexible nanoengineered multimodal sensor array for *in situ* sweat inflammatory biomarker analysis. The use of gold nanoparticles (AuNPs)-decorated mass-producible laser-engraved graphene (LEG) enables highly sensitive and efficient electrochemical detection of trace-level sweat CRP *in situ* on the skin. AuNPs conjugated with electroactive redox molecule thionine (TH) and detector antibody (dAb) enable efficient electrochemical signal transduction (Signal ON) and further signal amplification. The integrated pH, temperature, and ionic strength graphene sensors enable real-time personalized CRP data calibration to mitigate the interpersonal sample matrix variation-induced sensing error, and provide a more comprehensive assessment of the

inflammatory status^{46,47}. We confirmed the presence of CRP in human sweat from healthy subjects and identified elevated sweat CRP levels in patients with chronic and acute inflammations associated with COPD, heart failure (HF), and active and past infections (e.g., COVID-19). A strong correlation between sweat and serum CRP levels was obtained in both healthy and patient populations, for the first time, indicating the promise of this technology in non-invasive disease classification, monitoring, and management.



Figure 3-1 Wearable electrochemical nanobiosensor for automatic, non-invasive, and wireless inflammation monitoring. **a**, Circulating C-reactive protein (CRP), released from inflammatory responses, is closely related to various chronic and acute health conditions and could be secreted *via* the sweat gland. COPD, chronic obstructive pulmonary disease. **b**, Schematic of the skin-interfaced multimodal wearable nanobiosensor that contains an iontophoretic module for localized sweat extraction on-demand, a microfluidic module for automated sweat sampling and reagent routing, and a flexible laser-engraved graphene (LEG) multimodal sensor array for multiplexed sensing of sweat CRP, pH, temperature, and ionic strength. PI, polyimide; carbogel,

carbachol hydrogel; PET/M-tape, polyethylene terephthalate/medical tape; IP, iontophoresis. **c,d**, Optical images of a disposable microfluidic graphene sensor patch (**c**) and a vertical stack assembly of the fully integrated wireless wearable system (**d**). Scale bars, 0.5 cm. **e**, The mechanism of *in situ* microfluidic sweat CRP analysis that involves fully-automatic sweat sampling, reagent routing, and detection. AuNPs, gold nanoparticles; cAb, capture antibody; dAb, detector antibody; SWV, square wave voltammetry; TH, thionine; LTH, leuco thionine.

3.2 Design of the wearable microfluidic LEG-AuNPs biosensor

Key components of the wearable sensor are a skin-interfaced flexible, disposable, multimodal microfluidic biosensor patch fabricated on a polyimide (PI) substrate *via* CO₂ laser engraving and a flexible printed circuit board (FPCB) for iontophoretic sweat induction, sensor data acquisition and wireless communication (**Fig. 3-1a,b** and **Appendix A, Fig. A-1**). The sensor array consists of an electrodeposited AuNPs-decorated LEG working electrode immobilized with anti-CRP capture antibodies (cAb), a Ag/AgCl reference electrode, an LEG counter electrode for sweat CRP capturing and electrochemical analysis, an LEG-based impedimetric ionic strength sensor, a LEG-polyaniline-based potentiometric sweat pH sensor, and a strain-insensitive resistive graphene temperature sensor (**Appendix A, Fig. A-2**). Considering that the potential users of this technology include sedentary and immobile patients, an iontophoresis module (based on a pair of LEG electrodes) is incorporated for on-demand delivery of cholinergic agonist carbachol from the carbachol hydrogel (carbagen) for autonomous sweat stimulation throughout daily activities without the need for vigorous exercise. A cost-effective and flexible microfluidic module is assembled by stacking laser-cut medical adhesives and polyethylene terephthalate (PET) for efficient sweat sampling (**Fig.3-1c**). The miniaturized FPCB interfaces compactly on top of the microfluidic sensor patch to form the fully integrated wearable system (**Fig. 3-1d**). Powered by a small on-board lithium battery, the wearable system is able to wirelessly communicate with a user interface *via* Bluetooth Low Energy (**Appendix A, Fig. A-3**).

In order to realize automatic wearable CRP detection *in situ*, the microfluidic module comprises a reagent reservoir for the storage of the labeled anti-CRP dAbs-conjugated AuNPs, a serpentine mixing channel for mixing of dAb with sweat CRP, and a detection reservoir for the capture and

quantification of sweat CRP (**Fig.3-1e**). The redox molecule, TH, is used to label the nanoparticle conjugates to achieve direct electrochemical sensing. As the autonomously induced sweat flows into the microfluidics, the deposited dAbs conjugated AuNPs are reconstituted within the reagent reservoir (I) and routed along with sweat through a serpentine passive mixer to facilitate the dynamic binding between sweat CRP and dAb (II). As the mixture enters the detection reservoir, it slowly fills the chamber before exiting *via* the outlet; the detection reservoir has an optimized size to allow sufficient time for CRP-dAb to bind with anti-CRP cAb functionalized LEG-AuNPs working electrode (III). Subsequently, a fresh sweat stream continues to refresh the microfluidics to achieve passive label removal (IV). Square wave voltammetry (SWV) is used to measure the amount of TH bound to the working electrode surface. Since TH molecules are directly conjugated to CRP dAb-immobilized AuNPs, their amount bound is directly correlated to the amount of CRP ‘sandwiched’ between cAbs at the electrode surface and dAb-immobilized AuNPs, and consequently, the initial concentration of CRP in solution.

3.2.1 Materials and methodology

Materials and Reagents

Silver nitrate, iron chloride (III) and hydrogen tetrachloroaurate (III) hydrate were purchased from Alfa Aesar. Sodium thiosulfate pentahydrate, sodium bisulfite were purchased from Sigma Aldrich. Potassium chloride was purchased from Thermo Fisher Scientific. Agarose was purchased from Fisher Scientific. Medical adhesives were purchased from 3M and Adhesives Research. Polyimide (PI) films (75- μm thick) were purchased from DuPont. Polyethylene terephthalate (PET) films (50 μm thick) were purchased from McMaster-Carr.

Fabrication of the multimodal microfluidic sensor patch

A PI film was raster engraved at focus height (8% Power, 15% Speed, 1000 Points Per Inch) to fabricate laser engraved graphene (LEG)-based iontophoresis (IP) electrodes, connection leads, impedance, CRP working, counter and reference electrodes using a 50 W CO₂ laser cutter (Universal Laser System). The pH electrode and temperature sensor were engraved using vector mode with 1% and 3% Power, respectively (15% Speed, 1000 Points Per Inch (PPI)). The working electrode of pH sensor was prepared by electrochemically cleaning the LEG electrode in 1M HCl

via cyclic voltammetry from -0.2 to 1.2 V at 0.1 V s^{-1} for 10 cycles followed by electrodeposition of polyaniline pH sensing membrane *via* cyclic voltammetry from -0.2 to 1.2 V at 0.1 V s^{-1} for 10 cycles. The shared Ag/AgCl reference electrode was fabricated by electrodeposition of Ag on the LEG electrode in a solution containing silver nitrate, sodium thiosulfate, and sodium bisulfite (250 mM, 750 mM, and 500 mM, respectively) using multi-current steps (30 s at $-1 \mu\text{A}$, 30 s at $-5 \mu\text{A}$, 30 s at $-10 \mu\text{A}$, 30 s at $-50 \mu\text{A}$, 30 s at -0.1 mA and 30 s at -0.2 mA), followed by drop casting 10 μL -aliquot of 0.1M iron chloride (III) for 1 minute. AuNPs were electrodeposited on the LEG CRP working electrode *via* pulse deposition (two 0.5 s pulses at -0.2 V separated by a 0.5 s pulse at 0 V) for 40 cycles in the presence of 0.1 mM gold(III) chloride trihydrate and 10 mM sulfuric acid.

The iontophoresis hydrogels containing cholinergic agent carbachol (placed on the IP electrodes) were prepared by dissolving agarose (3% w/w) in deionized water using a microwave oven. After the agarose was fully dissolved, the mixture was cooled down to $165 \text{ }^\circ\text{C}$ and 1% carbachol for anode (or 1% KCl for cathode) was added to the above mixture and stirred to homogeneity. The cooled mixture was casted into cylindrical molds or assembled microfluidic patch and solidified at room temperature. The hydrogels were stored at $4 \text{ }^\circ\text{C}$ until use.

To prepare the microfluidic module, an assembly of thin PET film ($50 \mu\text{m}$) sandwiched between double-sided medical adhesives ($180 \mu\text{m}$ top layer, $260 \mu\text{m}$ bottom layer with a $50 \mu\text{m}$ PET backing) was attached to a substrate and cut through to make the channels and reagent reservoirs using the laser cutter at 2.7% power, 1.8% speed, 1000 PPI vector mode. Next 4% power, 10% speed, 1000 PPI vector mode was used to cut a circular outline through only the top layer of medical adhesive ($180 \mu\text{m}$). The circular top layer was peeled off to make the detection reservoir. A sweat accumulation layer was prepared by cutting through a $130 \mu\text{m}$ adhesive. The labeled dAb-AuNPs were drop-casted and dried in the reagent reservoir and stored in dry state at 4°C before assembly with the sensor patch.

Electronic system design and integration

A 2-layer flexible printed circuit board (FPCB) was designed using Eagle CAD and Fusion 360. The FPCB outline was designed as a rounded rectangle ($31.7 \text{ mm} \times 25.5 \text{ mm}$) the same size as the microfluidic sensor patch such that the patch can be inserted directly underneath the FPCB via a

cutout (10 mm x 3.8 mm). The electronic system is composed of a magnetic reed switch (MK24-B-3, Standex-Meder Electronics) and a voltage regulator (ADP162, Analog Devices) for power management; a boost converter (TPS61096, Texas Instruments), BJT array (BCV62C, Nexperia), and analog switch (DG468, Vishay Intertechnology) for iontophoretic induction; an electrochemical front-end (AD5941, Analog Devices), an operational amplifier (LPV811, Texas Instruments), and a voltage divider for sensor array interface; and a Bluetooth Low Energy (BLE) module (CYBLE-222014-01, Cypress Semiconductor) programmed via PSoC Creator 4.3 for system control and Bluetooth wireless communication. A BLE dongle (CY5677, Cypress Semiconductor) programmed via PSoC Creator 4.3 or custom mobile application programmed via Flutter was used to establish a BLE connection with the wearable device and to wirelessly acquire sensor data for calibration and voltammogram analysis. A rechargeable 3.8 V lithium button cell battery with capacity of 8 mAh was used to power the electronic system. To reduce the existing noise caused by motion artifacts, filtering and smoothing techniques are employed. On the hardware side, the electrochemical AFE filters noise from the ADC *via* digital filters. On the software side, smoothing algorithms (moving average filter/median filter) are automatically applied in real-time.

3.3 LEG-AuNPs immunosensor for CRP detection

3.3.1 Materials and Methodology

Materials and Reagents

2-(N-morpholino)ethanesulfonic acid hydrate (MES), mercaptoundecanoic acid (MUA), mercaptohexanol (MCH), N-(3-Dimethylaminopropyl)-N'-ethylcarbodiimide (EDC), N-hydroxysulfosuccinimide sodium salt (sulfo-NHS), bovine serum albumin (BSA), hydroquinone, hydrocortisone, human immunoglobulin G (IgG), thionine acetate salt, 1H-Pyrrole-1-propionic acid (PPA), 1-Pyrenebutyric acid (PBA), Tween® 20, calcium chloride were purchased from Sigma Aldrich. Potassium ferricyanide (III), and potassium ferrocyanide (IV) were purchased from Acros Organics. Potassium chloride, 96-well Nunc MaxiSorp™ flat-bottom plate, lyophilized human tumor necrosis factor alpha (TNF- α) were purchased from Thermo Fisher Scientific. Sulfuric acid, hydrochloric acid, sodium carbonate anhydrous, sodium bicarbonate, sodium

chloride, sodium dihydrogen phosphate, potassium hydrogen phosphate, potassium chloride, hydrogen peroxide (30% (w/v)), dimethylformamide (DMF), 10X phosphate-buffered saline (PBS) were purchased from Fisher Scientific. 20 nm carboxyl (carboxyl-PEG3000-SH) gold nanoparticles (AuNPs) was purchased from Cytodiagnosics Inc. CRP capture antibody (cAb) and biotinylated detector antibody (dAb) were from the ELISA kit purchased from R&D systems (Human CRP DuoSet ELISA, DY1707).

LEG-AuNPs CRP working electrode functionalization

LEG-AuNPs working electrodes were immersed in 0.5 mM MUA and 1 mM MCH in proof 200 ethanol overnight for self-assembled monolayer (SAM) formation. After rinsing with ethanol followed by deionized (DI) water and drying under airflow, electrodes were incubated with 10 μL of a mixture solution containing 0.4 M EDC and 0.1 M Sulfo-NHS in 25 mM MES buffer, pH 5.0, for 35 minutes at room temperature in a humid chamber. Covalent attachment of CRP cAbs was carried out by drop casting 10 μL of anti-CRP solution (250 $\mu\text{g mL}^{-1}$ in PBS, pH 7.4) and incubated at room temperature for 2.5 hours, followed by a 1-hour blocking step with 1.0% BSA prepared in PBS. Electrodes were stored in 1% BSA in PBS until use.

CRP detector antibody conjugation

20 nm carboxylic acid functionalized PEGylated gold AuNPs were activated with EDC/Sulfo-NHS mix solution (30 mg mL^{-1} and 36 mg mL^{-1} , respectively) in 10 mM MES buffer (pH 5.5) for 30 minutes. The conjugates were washed with 1X PBS containing 0.1% Tween® 20 (PBST) and centrifuged at 6500 relative centrifugal force (rcf) for 30 minutes. After supernatant removal, 50 $\mu\text{g mL}^{-1}$ polystreptavidin R (PS-R) was added and allowed to crosslink for 1 hour at room temperature. Following centrifugation at 3500 rcf for 30 minutes and supernatant removal, 5 $\mu\text{g mL}^{-1}$ biotinylated anti-CRP dAb in 1% BSA prepared in 1X PBS (pH 7.4) was incubated for 1 hour at room temperature. After another round of washing (centrifugation at 2000 rcf), the carboxyl groups of PS-R and dAb on AuNP were activated with EDC/Sulfo-NHS mix solution (30 mg mL^{-1} and 36 mg mL^{-1} , respectively) in 10 mM MES buffer (pH 5.5) for 30 minutes. After the washing step using centrifugation at 1500 rcf, 100 μM thionine was incubated for 1 hour. The final

conjugate was washed with PBST, centrifuged at 1250 rcf, reconstituted in 1% BSA and filtered through 0.2 μm syringe filter to remove all aggregates.

For direct redox probe conjugation to antibodies, 100 $\mu\text{g mL}^{-1}$ dAb was buffer exchanged by concentrating with a 100K MWCO protein concentrator and reconstituted in 10 mM MES buffer (pH 5.5). The carboxyl groups of dAb were activated with EDC/Sulfo-NHS mix solution (30 mg mL^{-1} and 36 mg mL^{-1} , respectively) in 10 mM MES buffer (pH 5.5) for 30 minutes in column. Following buffer exchange with 1X PBS (pH 7.4), 100 μM thionine was incubated for 1 hour. The final conjugate was buffer exchanged with PBS, reconstituted in 1% BSA, and filtered through 0.2 μm syringe filter to remove all aggregates.

Characterization of the biosensing platform

The morphology and material properties of the LEG-based CRP sensing electrodes before and after surface modification were characterized by focused ion beam-scanning electron microscopy (FIB-SEM) (FEI Nova 600 NanoLab), transmission electron microscopy (TEM) (TecnaiTF-20), Raman spectroscopy, x-ray photoelectron spectroscopy (XPS) (Kratos Ultra XPS), and Ultraviolet–visible spectroscopy (UV-vis). Raman spectra of the electrodes were recorded using a 532.8 nm laser with an inVia Reflex (Renishaw, UK). Dynamic light scattering data were collected with Malvern Dynamic Light Scattering (DLS) Zetasizer. UV-Vis absorbance data were collected with BioTek Synergy HTX multi-mode reader.

In vitro electrochemical characterizations were carried out on a CHI660e electrochemical workstation with a commercial Ag/AgCl electrode as the reference electrode.

Specifically, in order to characterize surface modification after each step electrochemically, differential pulse voltammetry (DPV) and open circuit potential-electrochemical impedance spectroscopy (OCP-EIS) readings were obtained in 0.1M KCl, containing 5.0 mM of $\text{K}_4\text{Fe}(\text{CN})_6/\text{K}_3\text{Fe}(\text{CN})_6$ (1:1) under conditions: potential range, -0.2–0.6 V; pulse width, 0.2 s; incremental potential, 4 mV; amplitude, 50 mV; frequency range, 0.1– 10^6 Hz; amplitude, 5 mV.

Comparison of sensing performance with bare graphene-modified sensors was conducted following protocols published previously^{43,61}. Briefly, the LEG electrodes were electrodeposited with poly(propionic acid) (PPA) *via* cyclic voltammetry or modified with pyrenebutyric acid (PBA)

via π - π stacking by immersing the electrodes in 5 mM PBA prepared in DMF for 2 hours. LEG was electrochemically oxidized in PBS (1X, pH 3) at +1.75V for 45 seconds to produce graphene oxide (LEGO). Next the LEG electrodes were activated with EDC/Sulfo-NHS and were incubated with cAbs ($250 \mu\text{g mL}^{-1}$ in PBS, pH 7.4) for 2.5 hours. To compare the electrochemical performance, the cAb-modified electrodes were incubated in 0 ng mL^{-1} or 10 ng mL^{-1} CRP in 1% BSA for 15 minutes, followed by for 15-minutes incubation in $1 \mu\text{g mL}^{-1}$ horseradish peroxidase (HRP) conjugated anti-CRP dAbs. Amperometric readings were recorded at 0 V in 50 mM sodium phosphate buffer (pH 6.0) containing 2.0 mM hydroquinone and 10 mM H_2O_2 .

Electrochemical detection of CRP in buffer and biofluids was performed by mixing 4.5 μL -aliquots of CRP standards (or raw biofluids to be analyzed) with 0.5 μL dAb-loaded AuNPs (1/10 dilution prepared in 10% BSA prepared in 1X PBS, pH 7.4) and drop casting onto the working electrode, allowing CRP and dAb binding to take place for 15 minutes before rinsing with PBS. Square wave voltammetry (SWV) was used to record the CRP signal in 1X PBS, pH 7.4. SWV conditions: potential range, 0–0.6 V; increment potential, 10 mV; amplitude, 50 mV; frequency, 25 Hz. The performance of the CRP sensors subjected to different incubation and detection conditions was evaluated from pH 6 to pH 10 and from 0.1X PBS to 2X PBS. Selectivity test was conducted in the presence of mixture solutions of 1/100 dAb-loaded AuNPs (final concentration) and 5 ng mL^{-1} cortisol, immunoglobulin G (IgG), tumor necrosis factor alpha (TNF- α) and CRP in the presence of 5 ng mL^{-1} CRP.

The influence of mechanical deformation on the sensor performance was investigated by incubating the sensor patch in CRP standards for 15 minutes or McIlvaine buffers for pH sensors under mechanical deformation (with radii of bending curvature 2.5 and 3.5 cm). The temperature sensor readings were recorded by placing the patch in an oven under mechanical deformation.

3.3.2 Results and Discussion

The functionalization process for the preparation of the CRP immunosensor is illustrated in **Fig. 3-2a** and **Appendix A, Fig. A-4** AuNPs are electrodeposited on the LEG surface followed by subsequent thiol monolayer assembly with mercaptoundecanoic acid and mercaptohexanol. As the formation of SAM layer relies on specific gold-sulfur bonding, immersion of the sensor patch in

alkanethiol solution has negligible influence on other graphene-based electrodes (**Appendix A, Fig. A-4**). Pulsed potential-deposited AuNPs evenly distribute throughout the mesoporous graphene structure and possess superior electrocatalysis capability and form a large number of binding sites on the surface of the particles for biomolecule immobilization (**Fig. 3-2b,c** and **Fig. A-5**). This substantially improves the sensitivity of the CRP sensor with little non-specific adsorption (**Appendix A, Fig. A-6**). The formation of LEG-AuNPs composite is confirmed through the increased ratio of the intensity of D and G bands in the Raman spectra due to the presence of AuNPs (**Fig. 3-2d**)⁴⁸. The individual sensor modification steps on the LEG electrodes are characterized with X-ray photoelectron spectroscopy (**Fig. 3-2e** and **Appendix A, Fig. A-7**). The intensity of Au4f increases significantly after the deposition of AuNPs while N1s increases only after the cAb immobilization step, indicating successful electrode preparation (**Fig. 3-2e**). Differential pulse voltammetry (DPV) and electrochemical impedance spectroscopy (EIS) were used to further characterize the LEG surface electrochemically after each modification step (**Fig. 3-2f** and **Appendix A, Fig. A-8**). The decrease in peak current height in DPV voltammograms and increased resistance in Nyquist plots after self-assembled monolayer (SAM) and cAb protein immobilization indicate that SAM and cAb impede the electron transfer at the interface. This is due to the increase in surface coverage by non-conductive species. Moreover, the negatively charged carboxylate functional groups in the SAM layer result in the repulsion of the negatively charged redox indicator, ferricyanide, and further reduces the electron transfer rate. Subsequent modification of the SAM layer with EDC/NHS chemistry replaces the negatively charged carboxylate groups with neutral NHS-ester groups. This is empirically observed as an increase in peak current height. Such electrode fabrication processes show high batch-to-batch reproducibility as the main processes including laser engraving, electrochemical deposition, and solution process are all mass-producible (**Appendix A, Fig. A-9**).

In order to realize trace-level sweat CRP analysis, PEGylated AuNPs that possess large surface area-to-volume ratio are functionalized with polystreptavidin R to increase the loading of biotinylated-dAbs and subsequently enhance the sensitivity (**Appendix A, Fig. A-10** and **A-11**). One-step direct electrochemical detection is enabled by crosslinking the redox label TH onto the carboxylate residues on the dAb-loaded AuNPs. As the TH-labeled dAb-loaded AuNPs bind to the

mesoporous graphene electrode upon CRP recognition, TH located on the external sites of the proteins are in close proximity to the graphene surface in each mesopores for electron transfer. Increases in hydrodynamic sizes (**Fig. 3-2g**) and the shifts of ultraviolet-visible (UV-Vis) absorbance (**Appendix A, Fig. A-12**) of the AuNPs conjugate after each modification step, along with the transmission electron microscope (TEM) image of the dispersed AuNPs-dAb conjugates (**Fig. 3-2h**) confirm the successful immobilization of the dAbs.

The performance of the CRP sensor was evaluated with SWV in CRP spiked phosphate-buffered saline (PBS) solutions (**Fig. 3-2i**). The increases in peak current height of TH reduction show a linear relationship with increased target concentrations (**Fig. 3-2j**). The sensor showed an ultralow limit of detection of 8 pM, good batch-to-batch reproducibility (**S Appendix A, Fig. A-13**), and the sensing accuracy can be further enhanced by automating the sensor preparation and modification process (e.g., *via* automated fluid dispensing or inkjet printing⁴⁹). The LEG-AuNPs CRP immunosensor demonstrates high selectivity over other potential interference proteins and hormones attributed to the sandwich assay format (**Fig. 3-2k** and **Appendix A, Fig. A-14**). Considering interpersonal variations during the human study, the influence of sweat pH, ionic strength, temperature, and sample volume on the antibody-antigen binding kinetics and redox probe electron transfer rate on CRP sensing accuracy was investigated (**Appendix A, Fig. A-15**) and mitigated by introducing suitable calibration mechanisms. The potential variations of the Ag/AgCl pseudo-reference electrode in the presence of varying Cl⁻ concentration in the physiologically-relevant range result in a small shift in the peak potential but its influence on the overall peak current density (and thus CRP quantification) is negligible (**Appendix A, Fig. A-16**). The accuracy of the CRP sensor for biofluid analysis was validated by the laboratory gold standard enzyme-linked immunosorbent assay (ELISA) using human sweat and saliva samples (**Fig. 3-2l**). The disposable CRP sensors also maintained stable sensor performance over a 10-day period when stored in PBS in the refrigerator at 4°C (**Appendix A, Fig. A-17**).

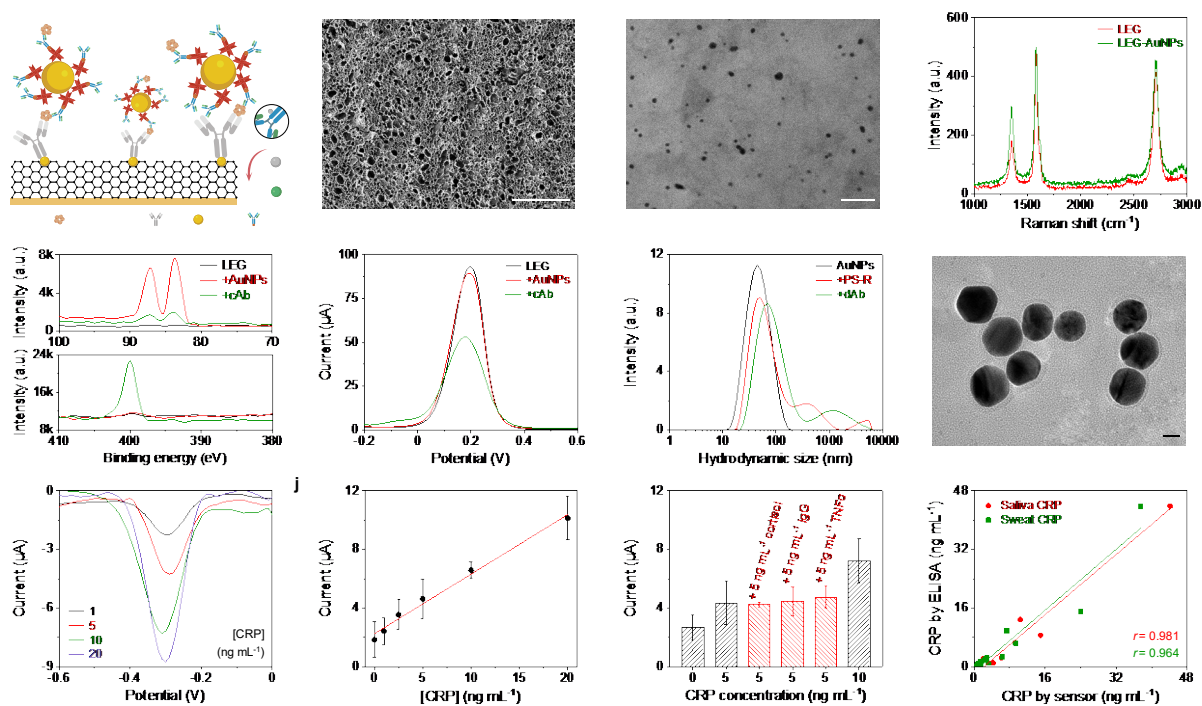


Figure 3-2 Materials and electrochemical characterizations of the LEG-AuNPs CRP sensor.

a, Schematic of the one-step electrochemical sandwich CRP immunosensor. PS-R, Polystyrene. **b**, Scanning electron microscope (SEM) image of the mesoporous LEG electrode. Scale bar, 100 μm . **c**, Transmission electron microscopy (TEM) image of AuNPs-decorated graphene flakes. Scale bar, 50 nm. **d**, Raman spectra of LEG electrode and AuNPs-decorated LEG electrode. **e**, X-ray photoelectron spectra of the LEG after the deposition of AuNPs, thiol-based self-assembled monolayer (SAM), and cAb immobilization. **f**, DPV voltammograms of a sensing electrode in a 0.1 M KCl solution containing 5.0 mM $\text{K}_4\text{Fe}(\text{CN})_6/\text{K}_3\text{Fe}(\text{CN})_6$ (1:1) after each surface-modification step: bare LEG, deposition of AuNPs, SAM modification, carboxylic acid group activation with N-(3-Dimethylaminopropyl)-N'-ethylcarbodiimide/N-hydroxysulfosuccinimide (EDC/Sulfo-NHS), and cAb immobilization followed by bovine serum albumin (BSA) blocking. **g**, Hydrodynamic sizes of the PEGylated AuNPs after each conjugation step by dynamic light scattering: PS-R immobilization, biotinylated dAb binding, and redox molecule TH conjugation followed by BSA deactivation. **h**, TEM image of the dispersed dAb-loaded AuNPs with protein corona shells. Scale bar, 10 nm. **i,j**, SWV voltammograms (**i**) and the corresponding calibration plot (**j**) of the CRP sensors in 1X PBS (pH 7.4) with 0–20 ng mL^{-1} CRP

and 1% BSA. Error bars represent the s.d. from 3 sensors. **k**, Selectivity of the CRP sensor to potential interferences in sweat. Error bars represent the s.d. from 3 sensors. **i**, Validation of the CRP sensor in human sweat samples (n=13) and saliva samples (n=6) with ELISA. The Pearson correlation coefficient was acquired through linear regression.

3.4 Evaluation of sweat CRP for non-invasive monitoring of systemic inflammation

3.4.1 Materials and Methodology

Materials and reagents

4-(2-hydroxyethyl)-1-piperazineethanesulfonic acid (HEPES), calcium chloride, 3 kDa Amicon Ultra-0.5 centrifugal filter unit, and urea were purchased from Sigma Aldrich. Pierce™ Protein Concentrators PES, 100K MWCO, trypsin, Pierce™ C18 Spin Columns were purchased from Thermo Fisher Scientific. LCMS grade acetonitrile, HPLC grade water, folic acid, trifluoroacetic acid were purchased from Fisher Scientific. Recombinant human CRP protein standard was purchased from Abcam (ab167710). Lysyl endopeptidase was purchased from FUJIFILM Wako Chemical Corp.

Subjects and procedures

The performance of the wearable sensor was evaluated in human sweat and saliva samples from healthy human subjects and subjects recently recovered from COVID-19 infection in compliance with the protocols that were approved by the institutional review board (IRB) (#19-0892, #19-0894 and #21-1108) at California Institute of Technology (Caltech). The participating subjects were recruited from Caltech campus and the neighboring communities through advertisement by posted notices, word of mouth, and email distribution. All subjects gave written, informed consent before participation in the study.

Human subjects for evaluation of the sweat CRP in COPD monitoring were recruited at The Lundquist Institute/Harbor-UCLA Medical Center with the protocol approved by the IRB at the Lundquist Institute (#32051-01). Male and female, current or former smokers with or without COPD were recruited. Inclusion criteria were: aged 40-80 years; BMI between 18–40 kg m⁻²; >10 pack-year smoking history. Additional inclusion criteria for COPD patients were: forced expiratory

volume in 1 second / forced vital capacity (FEV₁/FVC) <0.7; FEV₁ < 80%; modified Medical Research Council (mMRC) dyspnea scale ≥ 2 ; COPD Assessment Test (CAT) >5. Exclusion criteria included: significant chronic disease, other than COPD; severe and/or uncontrolled medical conditions that could interfere with the study; malignancy within the previous 2 years; HIV infection; active tuberculosis; documented cardiovascular disease or resting ECG abnormality; use of systemic corticosteroids; COPD exacerbation within 3 months; those requiring supplemental oxygen.

Adult patients with a diagnosis of heart failure were recruited from the University of California, Los Angeles (UCLA) Ahmanson Cardiomyopathy Clinic, and the protocol was approved by the UCLA IRB (#19-000388). Exclusion criteria included pregnancy, severe skin allergy, current need for inpatient hospitalization, current use of beta-blocker medication therapy due to theoretical interaction with pilocarpine, active inotropic medication infusion, hypotension or hypertension, severe bradycardia or tachycardia, or significant cardiac conduction disorder.

Human subjects for evaluation of the sweat CRP in infection monitoring were recruited with a protocol approved by the IRB at Cedars-Sinai Medical Center (#STUDY00001099). Enrolled patients were admitted to the hospital ≥ 18 years of age that had an active infection (e.g., pneumonia, UTI, cellulitis, etc.).

Sample collection for in vitro studies

An iontophoresis session was implemented using a Model 3700 Macroduct Sweat Collection System for sweat induction, the subjects were asked to wear a Macroduct collector over a period of 60 minutes for sweat collection. Subjects were asked to refrain from eating, drinking, and chewing gum 30 minutes before saliva collection. After rinsing mouth with water, volunteers deposited saliva in 1.5 mL Eppendorf tubes which were subsequently centrifuged at 10000 revolutions per minute (rpm) for 10 minutes and analyzed. Fresh blood samples were collected at same periods of time as saliva and/or sweat either using a finger-prick approach or *via* venous blood draw. Once standardized clotting procedure finished, serum was separated by centrifuging at 3575 rpm for 15 minutes, and instantly stored at -80 °C.

Human sample analysis with enzyme-linked immunosorbent assay (ELISA)

ELISA tests for CRP were performed in an accuSkan™ FC Filter-Based Microplate Photometer at a detection wavelength of 450 nm, according to the manufacturer's instructions. Briefly, 96-well Nunc MaxiSorp™ flat-bottom plate was modified with anti-CRP antibodies in 50 mM carbonate buffer (pH 9.6) overnight at 4°C. Standards or diluted biofluid samples prepared in 1% BSA were added to anti-CRP antibody-coated microtiter plate wells and incubated for 2 hours at room temperature. After three washing steps with wash buffer (PBST, pH7.4), biotinylated detector antibodies were added to each well and incubated for 2 hours at room temperature. After three washing steps, streptavidin-HRP was added and incubated for 20 minutes at room temperature. Following three washing steps, 100 µL of 3,3',5,5'-Tetramethylbenzidine (TMB) substrate was incubated for 15 minutes, and absorbance values were measured immediately after the addition of 50 µL of 1M H₂SO₄ to each well.

Human sample analysis with liquid chromatography-tandem mass spectrometry (LC-MS/MS)

1 mL pooled sweat sample was concentrated using Amicon centrifugal filters with a molecular weight cutoff (MWCO) of 3 kDa to 15 µL final volume at a concentration factor of 67X. The concentrated samples were buffer exchanged in 8 M urea in 10 mM 4-(2-hydroxyethyl)-1-piperazineethanesulfonic acid (HEPES) buffer (pH 7.4), reduced with 3.7 mM tris(2-carboxyethyl)phosphine (TCEP) for 20 minutes at 37 °C and alkylated with 10 mM chloroacetamide (CAA) for 15 minutes at 37 °C. Proteins from each sample were digested at 37 °C with lysyl endopeptidase at a 1:100 ratio for 2 hours. The samples were then diluted with 50 mM HEPES buffer (pH 7.4) to a final concentration of 2 M urea and digested with trypsin at a 1:50 ratio at 37 °C for 14 hours. Digested peptides were acidified with 20% trifluoroacetic acid (TFA) and desalted with C18 spin columns using 50% acetonitrile (ACN) as the activation solution, 0.5% TFA in 5% ACN as the equilibration solution and wash solution, 2% TFA in 20% ACN as the sample buffer, and 0.2% formic acid (FA) in 70% ACN as the elution buffer. Desalted peptides were freeze-dried and stored at -20 °C until use. Lyophilized peptide was reconstituted in 10 µL 0.2% FA in 2% ACN. All incubation procedures were carried out with shaking at 750 rpm in the dark.

LC-MS/MS analysis was performed with an Vanquish Neo UHPLC system (ThermoFisher Scientific, San Jose, CA) coupled to an Orbitrap Eclipse Tribrid mass spectrometer (ThermoFisher Scientific, San Jose, CA). Peptides were separated on an Aurora UHPLC Column (25 cm × 75 μm, 1.6 μm C18, AUR2-25075C18A, Ion Opticks) with a flow rate of 0.35 μL min⁻¹ for a total duration of 75 min and ionized at 1.6 kV in the positive ion mode. The gradient was composed of 6% solvent B (3.5 min), 6–25% B (41.5 min), 25–40% B (15 min), 40–98% B (1 min) and 98% B (14 min); solvent A: 0.1% FA in water; solvent B: 80% ACN and 0.1% FA. MS1 scans were acquired at the resolution of 120,000 from 350 to 1,800 m z⁻¹, AGC target 1e6, and maximum injection time 50 ms. The charge states and intensity threshold of precursor ions for triggering MS2 was set to 2–7 and 5e3, respectively. For targeted CRP analysis, the precursor ions from the inclusion list (**Appendix A, Table A-3**) were selected for MS2 spectrum acquisition in the ion trap using fast scan rate and quadrupole isolation mode (isolation window: 1.2 m z⁻¹) with higher-energy collisional dissociation (HCD, 30%) activation type. Dynamic exclusion was set to 30 s. The temperature of ion transfer tube was 300°C and the S-lens radio frequency (RF) level was set to 30. MS2 fragmentation spectra were searched with Proteome Discoverer SEQUEST (version 2.5, Thermo Scientific) against in silico tryptic digested Uniprot Human database. The maximum missed cleavages was set to 2. Dynamic modifications were set to oxidation on methionine (M, +15.995 Da), protein N-terminal acetylation (+42.011 Da) and Met-loss (-131.040 Da). Carbamidomethylation on cysteine residues (C, +57.021 Da) was set as a static modification. The maximum parental mass error was set to 10 ppm, and the MS2 mass tolerance was set to 0.6 Da. The false discovery threshold was set strictly to 0.01 using the Percolator Node validated by q-value. The relative abundance of parental peptides was calculated by integration of the area under the curve of the MS1 peaks using the Minora label-free quantification (LFQ) node.

3.4.2 Results and Discussion

Despite the high potential of non-invasive CRP monitoring, the presence and levels of CRP in sweat are extremely underexplored in the literature⁵⁰. To affirm the presence of CRP in sweat generated by iontophoresis and by vigorous exercise, we first conducted a proteomic characterization of different types of sweat samples using bottom-up proteomic analysis as illustrated in **Fig. 3-3a**. Using a recombinant CRP protein standard as the reference, we

successfully identified CRP in both exercise and iontophoretic sweat samples from human subjects (**Fig. 3-3b**, **Appendix A**, **Fig. A-18**, and **Table A-3**). In this regard, we further evaluated the use of our LEG-AuNPs CRP sensors for the assessment of sweat CRP as a universal, cost-effective, and non-invasive approach to monitor systemic inflammation in various disease states (**Fig. 3-3c** and **Appendix A**, **Tables A4–A6**).

We investigated healthy subjects grouped according to smoking status (current, former, and never smokers), where CRP levels in both serum and sweat were greater in current smokers as compared with former and never smokers (**Fig. 3-3d**), consistent with previous reports on the effect of current smoking on serum CRP⁵¹. However, among COPD patients, serum and sweat CRP values were greater in former smokers than current smokers, consistent with irreversible tissue damage and chronic inflammation in COPD patients even after smoking cessation⁵². Monitoring sweat CRP in COPD patients may therefore be useful for following disease progression and/or predicting exacerbation in this patient population⁵³.

Chronic systemic inflammation is also related to increased risks of cardiovascular events³. In a preliminary study with HF patients, our sensor results show that serum and sweat CRP values were substantially elevated in HF patients with preserved ejection fraction (HFpEF) but not in HF patients with reduced ejection fraction (HFrEF) (**Fig. 3-3e**), consistent with past studies^{54–57}. The investigation of the dynamics of sweat CRP using our technology could potentially have high value in predicting HFpEF disease progression and clinical outcomes⁵⁵.

In addition to chronic infections in COPD and HF, it is well known that acute infections (such as COVID-19) could lead to severe inflammatory responses¹⁴. In a pilot study, we evaluated our sensor on hospitalized patients with active infections for two consecutive days (**Fig. 3-3f**). Significant increase (over 10-fold on average) in both serum and sweat CRPs was identified in patients with active infection as compared with healthy subjects, indicating the presence of highly elevated sweat CRP in acute inflammation.

By analyzing the samples from healthy subjects and patient populations with various inflammatory conditions using our sensor, a high correlation coefficient (r) of 0.844 ($n=80$) between sweat and serum CRP concentrations was obtained for the first time (**Fig. 3-3g**). Such correlation appears to

be higher than those obtained from saliva and urine samples (**Appendix A, Fig. A-19**), suggesting the great potential of using sweat CRP for the non-invasive monitoring of systemic inflammation toward the management of a variety of chronic and acute health conditions.

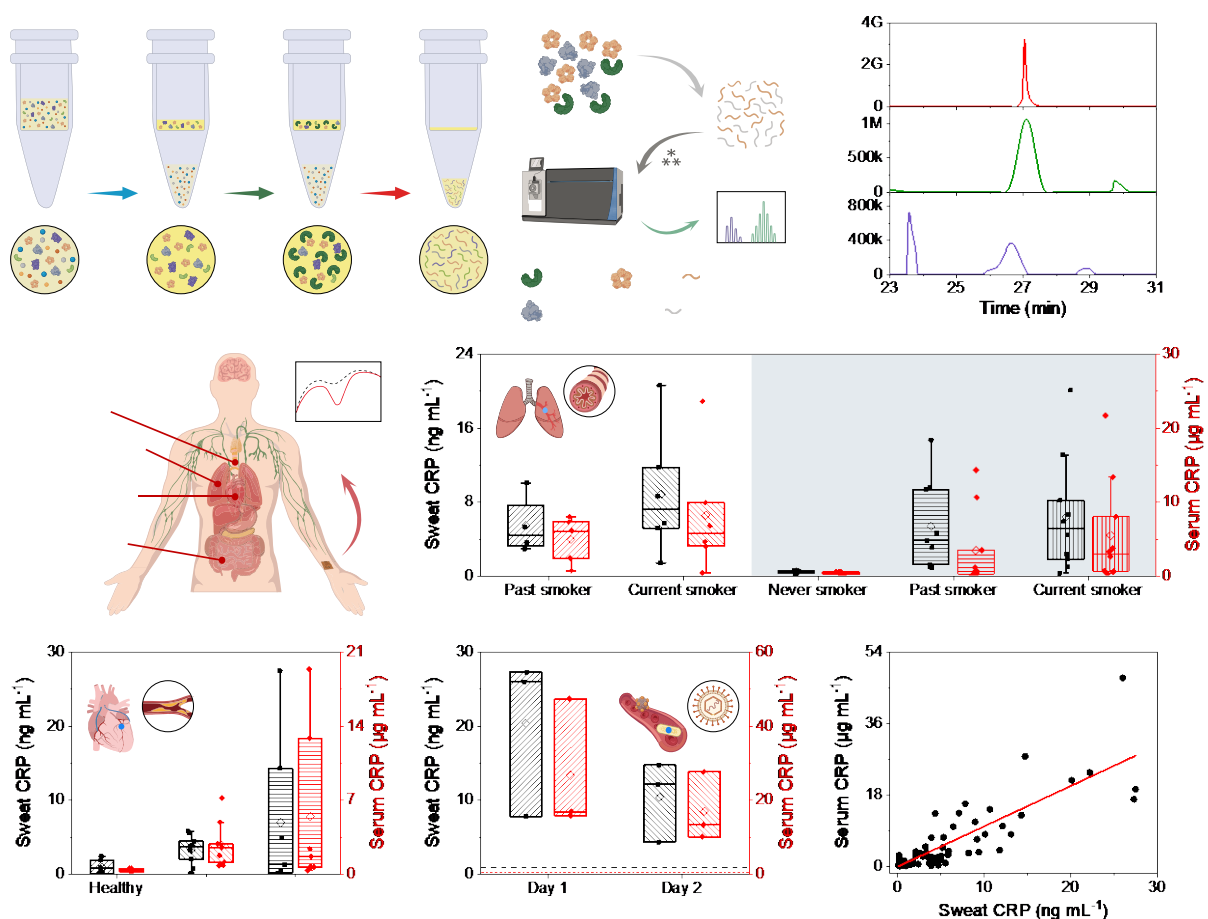


Figure 3-3. Evaluation of sweat CRP for non-invasive monitoring of systemic inflammation in healthy and patient populations. **a**, Schematic of proteomic analysis of human sweat using the liquid chromatography-mass spectrometry (LC-MS/MS). **b**, Chromatograms of the recombinant CRP reference peptide GYSIFSYATKR, iontophoresis-extracted and exercise sweat samples from human subjects. **c**, Schematic of the non-invasive inflammation monitoring in various health conditions with the LEG-AuNPs CRP sensor. **d**, Box-and-whisker plot of CRP levels in iontophoresis-extracted sweat and serum samples from subjects with COPD (n=10) and without COPD (n=24). The subjects are classified into five subgroups: current smokers with

COPD (n=6) or without COPD (n=10), former smokers with COPD (n=4) and without COPD (n=9), and never smokers without COPD (n=5). The bottom whisker represents the minima; the top whisker represents the maxima; and the square in the box represents the mean. **e**, Box-and-whisker plot of CRP levels in sweat and serum samples from healthy subjects (n=7), patients with heart failure with reduced ejection fraction (HFrEF) (n=7), and patients with heart failure with preserved ejection fraction (HFpEF) (n=9). The bottom whisker represents the minima; the top whisker represents the maxima; the square in the box represents the mean. **f**, Box-and-whisker plot of CRP levels in sweat and serum samples from 3 patients with active infection on two consequent days (n=3). The bottom whisker represents the minima; the top whisker represents the maxima; the square in the box represents the mean. Dotted lines represent the mean values of the sweat and serum CRP levels for healthy subjects. **g**, Correlation of serum and sweat CRP levels. The correlation coefficient r was acquired through Pearson's correlation analysis (n=80, $p < .00001$).

3.5 Characterization of the multiplexed microfluidic patch for automatic immunosensing

3.5.1 Materials and Methodology

Materials and reagents

Albumin–fluorescein isothiocyanate conjugate (FITC-albumin) was purchased from Sigma Aldrich. SureLight® Peridinin-Chlorophyll Protein Complex was purchased from Assaybio.

Numerical simulation

Simulation of the CRP-antibody binding reaction and mass transport process were conducted using the commercial software COMSOL Multiphysics through finite element analysis (FEA). Tetrahedral elements with refined meshes allowed modeling of the source diffusion in 3D space with testified accuracy. The chemical reaction rate is described by law of mass action

$$r = k^f c_{CRP} \cdot c_{antibody} - k^r c_{complex}$$

where r , k^f , k^r , c_{CRP} , $c_{antibody}$, and $c_{complex}$ denote reaction rate, forward reaction coefficient, reverse reaction coefficient, concentration of CRP, concentration of antibody and concentration of CRP-antibody complex, respectively. The forward and reverse reaction coefficients are assumed

to be $5.96 \times 10^4 \text{ M}^{-1}\text{s}^{-1}$ and $2.48 \times 10^{-3} \text{ s}^{-1}$, respectively⁶². The concentration of CRP in sweat is assumed to be 1 ng mL^{-1} .

The fluid behavior is described by the Navier-Stokes equation for incompressible flow

$$\rho \left(\frac{\partial v}{\partial t} + (v \cdot \nabla)v \right) = -\nabla p + \mu \nabla^2 v$$

$$\nabla \cdot v = 0$$

where ρ , v , p , and μ denote liquid density, flow velocity, pressure, and viscosity, respectively. The sweat flow rate is $1.5 \text{ } \mu\text{g mL}^{-1}$. And the convection diffusion is described by

$$\frac{\partial c}{\partial t} + v \cdot \nabla c = D \nabla^2 c$$

where c and D denote concentration and diffusion coefficient. The diffusion coefficient of CRP is $5 \times 10^{-11} \text{ m}^2\text{s}^{-1}$, the diffusion coefficient of antibody and CRP-antibody complex are set to be the same as gold nanoparticles which is $1 \times 10^{-12} \text{ m}^2\text{s}^{-1}$.

Experimental flow tests

The flow tests to evaluate the microfluidic sensing system were done with a syringe pump (Thermo Fisher Scientific, 78-01001). For the fluorescent flow test, a flow patch was pre-deposited with $0.5 \text{ } \mu\text{g}$ Peridinin-Chlorophyll Protein Complex (PerCP) and $200 \text{ } \mu\text{g}$ BSA in the reagent reservoir and dried before full patch assembly, and $0.25 \text{ } \mu\text{g mL}^{-1}$ FITC-albumin in 1X PBS was injected into the patch placed on a blue light transilluminator (Accuris SmartBlue Mini) at a flow rate of $1.5 \text{ } \mu\text{L min}^{-1}$. For the CRP sensor validation, $7 \text{ } \mu\text{L}$ of 2X PBS and $2 \text{ } \mu\text{L}$ of 10X dAb-loaded AuNP were deposited in the reagent reservoir and dried before full patch assembly, artificial sweat (0.1X or 0.2X PBS) containing CRP (1 ng mL^{-1} or 5 ng mL^{-1}) was injected into the patch at specified flow rate. For on-body flow test, an assembled flow patch pre-deposited with black dye in the reagent reservoir was attached onto a subject's arm after sweat induction by iontophoresis.

3.5.2 Results and Discussion

In order to realize accurate and automatic immunosensing *in situ*, the flexible sensor patch was designed to have a laser-engraved microfluidic module (consisting of a reagent reservoir, a mixing

channel, and a detection reservoir) and a multiplexed multimodal LEG sensor array (consisting of a CRP immunosensor, an ionic strength sensor, and a pH sensor) (**Fig. 3-4a**). As the microfluidic module routes sweat passively on the skin, the impedimetric ionic strength sensor automatically captures the state of the detection reservoir (reagent flow and refreshment); the measured admittance signals show a log-linear response with the electrolyte concentrations (**Fig. 3-4b,c**). As large interpersonal variations in electrolyte and pH levels were observed in both exercise and chemically induced sweat samples (**Appendix A, Fig. A-20**), high-level buffering salts were deposited with the dAbs in the reagent reservoir to mitigate potential binding environment changes caused by sweat composition variations (**Appendix A, Fig. A-21**). As such, this introduces an electrolyte gradient between the detection reagent reconstituted sweat (mixture) and fresh sweat that subsequently enters the detection reservoir. According to the numerical simulation, the routing of sweat and detection reagents can be summarized into four steps: reconstitution (I), incubation (II), refreshment (III), and detection (IV) (**Fig. A-4d,e** and **Appendix A, Note A-1**). Based on the microfluidic flow test using artificial sweat (0.2X PBS) under a mean physiological sweat rate ($1.5 \mu\text{L min}^{-1}$), the admittance signal is close to zero initially when no fluid enters the chamber during the reconstitution stage; as reconstituted, high-salt loaded detection reagents flow into the detection chamber, admittance reaches its peak value and gradually decreases as high-salt loaded reagents are flushed out of the detection chamber by newly secreted sweat (**Fig. 3-4f**). Since electrolyte content in iontophoresis sweat remains relatively stable for the same individual²⁸, the admittance response plateaus after all reagents have been refreshed by natural sweat, indicating the working electrode is ready for electrochemical CRP detection. Further experimental flow test using fluorescent proteins (fluorescein isothiocyanate-albumin as CRP surrogate and peridinin chlorophyll protein as detection reagent) shows a similar trend in incubation and refreshment process as the simulation and electrolyte flow test (**Fig. 3-4g**). Based on sweat rate information collected from 24 current and former smokers with and without COPD (**Appendix A, Fig. A-22**), flow tests with flow rates varying from 0.5 to $3.5 \mu\text{L min}^{-1}$ show similar admittance patterns with plateaus after various refreshing processes (**Fig. 3-4h**). The gradient of admittance at different flow rates converges to zero, as pre-loaded salts and dye are refreshed from the detection reservoir. The

mean sweat volume routed during this process before sensors readings were taken was estimated to be 21 μL based on flow rate and admittance measurements (**Fig. 3-4h**).

The performance of CRP sensors based on this automated electrolyte monitoring mechanism was evaluated in multiple microfluidic flow tests. SWV electrochemical measurements were initiated during the admittance plateaus (**Fig. 3-4i**). An increased concentration (from 1 to 5 ng mL^{-1}) led to an increased SWV peak current height while no substantial difference in CRP sensor response was observed for the same concentration under physiologically relevant flow rates (1, 1.5, 2.5, and 3.5 $\mu\text{L min}^{-1}$) (**Fig. 3-4i,j** and **Appendix A, Fig. A-23**). Although a higher flow rate could also result in a faster refreshment of the detection chamber and thus a shorter incubation time for the detection antibody and CRP, the increment in CRP signals under varying incubation time corresponding to the physiologically relevant sweat rates (between 5 and 20 minutes) is relatively small (**Appendix A, Fig. A-15**). Although the binding condition is pre-adjusted with deposited salts, the flow test with different initial electrolyte concentrations (0.1X and 0.2X PBS were chosen as artificial sweat to simulate interpersonal variations in sweat electrolyte concentrations) shows slightly decreased SWV signals at the lower electrolyte concentration due to the influence of electrolyte levels on the rate of TH reduction (**Fig. 3-4k,l**). Similar to *in vitro* selectivity results, no major interferences on the CRP detection signal were observed in the flow test (**Appendix A, Fig. A-24**). Moreover, flow tests using artificial sweat with different pH levels lead to varied SWV signals (**Appendix A, Fig. A-25**). These results indicate that sweat rate calibration is not necessary while additional *in situ* signal calibrations with sweat pH and electrolyte levels are needed to mitigate the interpersonal variations on CRP detection accuracy. Compared to previously reported passive wearable microfluidic sensors which rely on vigorous exercise to induce sweat and cannot reach sensitivities below mM levels (**Appendix A, Table A-7**), our technology offers an attractive fully automated microfluidic sweat induction, harvesting, and high-accuracy quantitative analysis solution, ideally suitable for at-home monitoring of clinically relevant trace-level biomarkers.

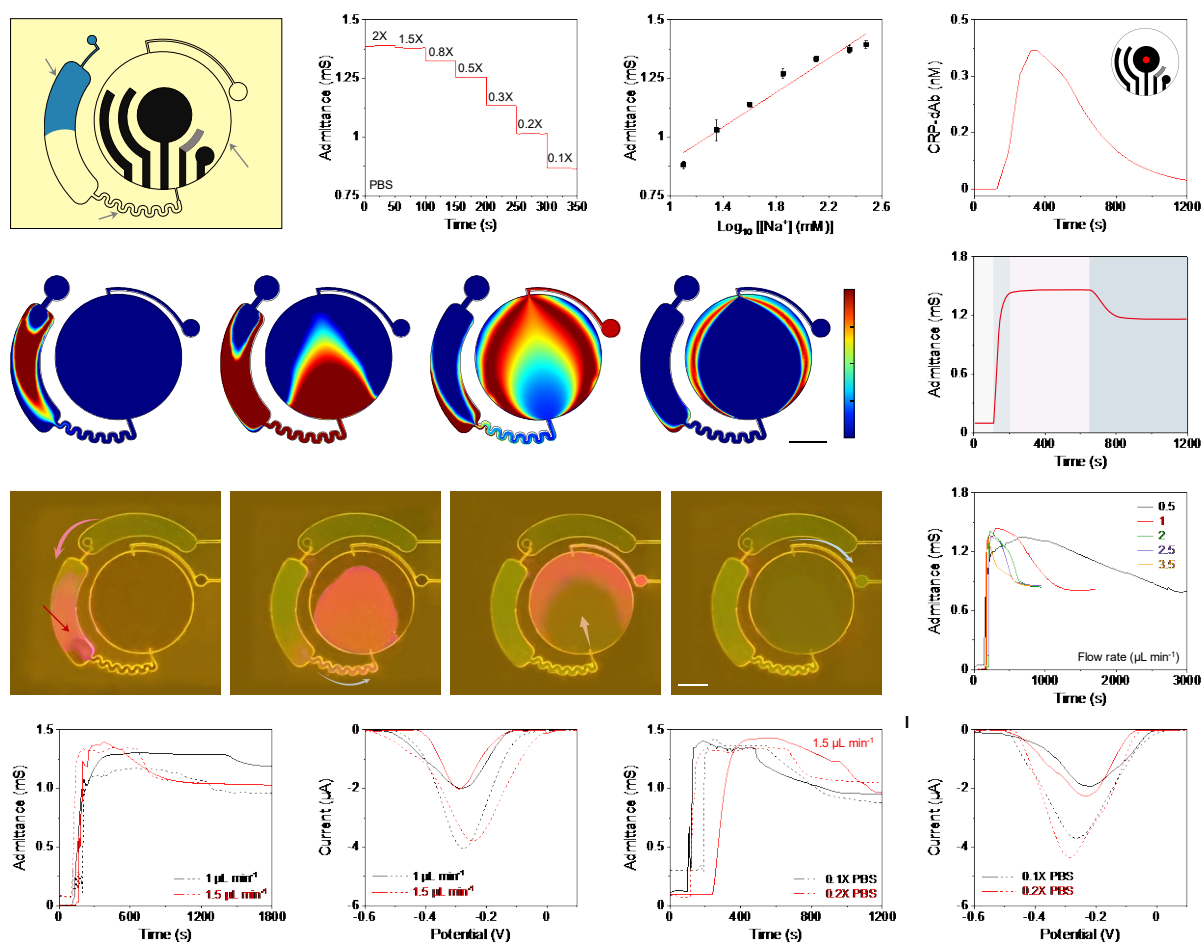


Figure 3-4. Multiplexed microfluidic patch for automatic immunosensing. **a**, Illustration of the multiplexed sensor array for automatic immunosensing. **b,c**, Admittance responses (**b**) and the corresponding calibration plot (**c**) of the impedimetric ionic strength sensor in NaCl solutions. Error bars represent the s.d. from 3 sensors. **d**, Simulated CRP-dAb concentration changes on the working electrode over time. Red dot in the inset image indicates the location of the concentration change plot. **e**, Simulated CRP-dAb concentrations colormaps showing phases of automatic sweat sampling and reagents routing toward *in situ* CRP detection: reconstitution (I), incubation (II), refreshment (III), and detection (IV). Scale bar, 200 μm . **f,g**, Admittance changes of the LEG ionic strength sensor (**f**) and optical images (**g**) during the four stages (I–IV) of automatic CRP sensing process in a laboratory flow test using artificial sweat (0.2X PBS) at a flow rate of 1.5 $\mu\text{L min}^{-1}$. Yellow fluorescein isothiocyanate (FITC)-albumin fluorescent label was used to imitate the flow

of sweat CRP and red Peridinin Chlorophyll Protein Complex (PerCP) was used in place of dAb-loaded AuNPs. Scale bar, 200 μm . **h**, Admittance responses of the ionic strength sensor in artificial sweat (0.2X PBS) at different flow rates from 0.5 to 3.5 $\mu\text{L min}^{-1}$. **i–l**, Influence of the flow rates (**i,j**) and ionic strengths (**k,l**) on microfluidic automatic CRP sensing. Solid and dotted lines represent tests performed in 1 and 5 ng mL^{-1} CRP, respectively.

3.6 System integration and on-body evaluation of the wearable biosensor

The fully integrated wearable inflammation monitoring system, InflaStat, is designed based on vertical stack assembly of a flexible microfluidic sensor patch and an FPCB and can be comfortably worn by the subjects (**Fig. 3-5a**). As illustrated in electronic circuit block diagram and schematic in **Fig. 3-5b** and **Appendix A, Fig. A-26**, the FPCB is able to perform current-controlled iontophoresis, multiplexed multimodal electrochemical measurements (including voltammetry, impedimetry, and potentiometry), signal processing, and wireless communication. The integrated system could also accurately obtain the dynamic responses of the integrated LEG-based pH, ionic strength, and skin temperature sensors for real-time CRP sensor calibration (**Fig. 3-5c-f, Appendix A, Fig. A-27**). The InflaStat is designed to have good mechanical flexibility and stability toward practical usage during various physical activities. Each individual sensor shows relatively small variations under a moderate radius of bending curvature (5 cm) (**Appendix A, Fig. A-28**). More strain-insensitive sensor designs can be included when necessary⁵⁸. During on-body operation, the InflaStat can conformally adhere to the skin through medical adhesive with *in situ* CRP sensing performed in the microfluidics without direct sensor-skin contact.

Clinical on-body evaluation of the wearable system was performed on healthy subjects (involving both never smokers and current smokers) as well as patients with COPD and post-COVID-19 infection (**Fig. 3-5g–l** and **Appendix A, Fig. A29–A31**). During the on-body trials, the wearable system laminates conformally on the subject's arm, chemically induces and analyzes sweat (**Appendix A, Fig. A-32**), and acquires inflammatory biomarker information non-invasively and wirelessly (**Fig. 3-5g**). The obtained sensor data can be displayed on a custom developed mobile app in real-time (**Fig. 3-5h**). *In situ* pH, temperature, and CRP sensor readings are acquired after the ionic strength sensor indicate full refreshment of the detection reservoir (**Fig. 3-5h–l**). It should

be noted that the TH's reduction peak for the CRP sensor appears at a slightly shifted potential given the variations in sweat pH (**Appendix A, Fig. A-33**). The CRP concentration was converted in the mobile app based on the obtained SWV voltammogram and the corresponding real-time obtained ionic strength, pH, and temperature values (**Appendix A, Fig. A-34** and **Note A-2**). As expected, an elevated CRP level was observed from the current smokers as compared with the never smokers in healthy subjects. The CRP levels in the COPD patients and post-COVID subjects were substantially greater than those of non-smoking healthy subjects, suggesting the promise of using the InflaStat in practical non-invasive systemic inflammation monitoring and disease management applications. *In vitro* analysis of sweat and serum from post-COVID subjects corroborate the on-body observation that patients who experienced moderate symptoms during COVID may still present a low-grade inflammation post-COVID episode as indicated by the slightly elevated CRP levels (**Appendix A, Fig. A-35** and **Table A-8**). It should be noted that similar as serum, sweat CRP levels remained stable during the test period (**Appendix A, Fig. A-36**) and no substantial variations were observed for chemically-induced sweat samples at different body locations (**Appendix A, Fig. A-37**).

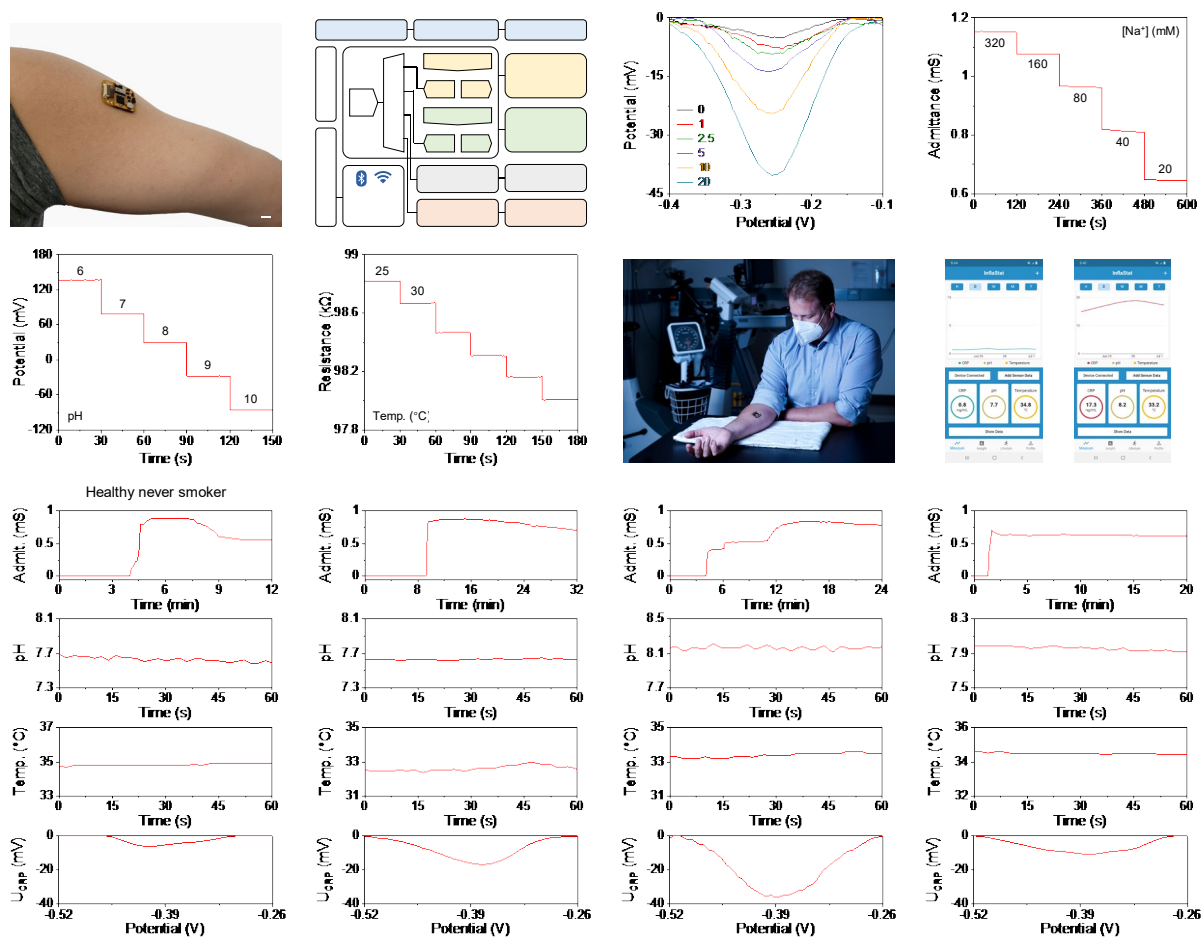


Figure 3-5. On-body evaluation of the multiplexed wearable patch toward non-invasive automatic inflammation monitoring. **a**, Image of a fully integrated wearable sensor on the arm of a human subject. Scale bar, 1 cm. **b**, Block diagram of the electronic system of the InflaStat. **c–f**, Calibration plots obtained using the wearable system from the CRP (**c**), ionic strength (**d**), pH (**e**) and temperature (**f**) sensors. Error bars represent the s.d. from 3 sensors. **g**, Photograph of a subject wearing the sensor patch during a clinical study. **h**, Custom mobile application for real-time data acquisition and display toward inflammation tracking. **i–l**, On-body multiplexed physicochemical analysis and CRP analysis with real-time sensor calibrations using the wearable sensor from a healthy never smoker (**i**), a healthy smoker (**j**), a COPD patient (**k**) and a post-COVID subject (**l**).

3.7 Conclusion

We developed a fully integrated wearable biosensor platform for real-time, non-invasive inflammatory biomarker monitoring through automatic *in situ* microfluidic analysis. The wearable sensor is capable of autonomous sweat extraction, harvesting, biomarker analysis, and wireless data transmission in sedentary individuals on-demand across daily human activities. In contrast to previous wearable platforms for monitoring biomarkers and our previously reported LEG-based sensors which typically detects metabolites at μM or higher level^{27,59}, this technology realizes highly sensitive detection of ultra-low-level inflammatory proteins *in situ* with a 6 orders-of-magnitude (picomolar level) improvement in sensitivity through a holistic combination of 1) a nanoengineered immunosensor highly sensitive and selective CRP analysis, 2) a microfluidic module for automatic sweat extraction, sampling, reagent routing and refreshing, 3) and a multiplexed multimodal graphene sensor array for real-time data acquisition and sensor calibration. The operation principle proposed herein can be readily adapted to survey a broad array of inflammatory biomarkers (e.g., cytokines) and beyond. We assessed the elevation of sweat CRP in healthy subjects and patients with various health conditions (e.g., COPD, HF, and active and past infections) for the monitoring of chronic and acute systemic inflammation and reported a high correlation between sweat and serum CRP levels for the first time. In practice, the spot checking of CRP every several hours is sufficient to monitor active infections and immune responses. The disposable point-of-care CRP sensor patch design with a reusable wearable electronic system serves the purpose of immediate, non-invasive, on-the-skin assessment of circulating CRP at any given time. When necessary, dynamic and automatic wearable CRP sensing could be realized by incorporating capillary bursting valves⁶⁰ and CRP sensor arrays into a single disposable sensor patch. It is also worth noting that although the clinical use cases we demonstrate in this work do not conform to current clinical practices, the reason behind this disparity is the lack of such specific, immediate, and non-invasive inflammation assessment tools rather than the lack of needs. The current turnaround time (1 day) of the clinical high-sensitivity CRP Test (hsCRP) does not meet this need for frequent assessments. In addition to hospitalized cases which require close monitoring of inflammatory state, many chronic diseases, such as COPD and inflammatory bowel disease,

could benefit from at-home, daily or frequent, fully automatic, and non-invasive assessment of CRP for disease management.

This wearable technology provides quantitative, personalized inflammatory information that addresses the unmet needs of patients and caregivers of chronic inflammatory diseases as society progresses towards decentralized medicine. Furthermore, given sweat's accessibility and its non-invasiveness, it holds great promise in interrogating the dynamicity of CRP in various disease models and providing clinical insights previously unfathomable. Further investigation of the metabolic timeline of sweat CRP in response to inflammatory stimuli and therapy initiation may provide insight into its promptness in clinical diagnosis and decision-making. We believe this technology represents an unprecedented wearable approach to assessing trace-level disease-relevant protein biomarkers on-demand.

Bibliography of Chapter 3

1. The top 10 causes of death. <https://www.who.int/news-room/fact-sheets/detail/the-top-10-causes-of-death>.
2. Mannino, D. M. *et al.* Economic burden of COPD in the presence of comorbidities. *Chest* **148**, 138–150 (2015).
3. Ferrucci, L. & Fabbri, E. Inflammageing: chronic inflammation in ageing, cardiovascular disease, and frailty. *Nature Review Cardiololgy* **15**, 505–522 (2018).
4. Ashley, N. T., Weil, Z. M. & Nelson, R. J. Inflammation: mechanisms, costs, and natural variation. *Annual Review of Ecology, Evolution, and Systematics* **43**, 385–406 (2012).
5. Schett, G. & Neurath, M. F. Resolution of chronic inflammatory disease: universal and tissue-specific concepts. *Nature Communications* **9**, 3261 (2018).
6. Furman, D. *et al.* Chronic inflammation in the etiology of disease across the life span. *Nature Medicine* **25**, 1822–1832 (2019).
7. Wylezinski, L. S. *et al.* Illuminating an invisible epidemic: a systemic review of the clinical and economic benefits of early diagnosis and treatment in inflammatory disease and related syndromes. *Journal of Clinical Medicine* **8**, 493 (2019).

8. The Emerging Risk Factors Collaboration, *et al.* C-reactive protein concentration and risk of coronary heart disease, stroke, and mortality: an individual participant meta-analysis. *Lancet* **375**, 132–140 (2010).
9. Ridker, P. M. A test in context: high-sensitivity C-reactive protein. *Journal of the American College of Cardiology* **67**, 712–723 (2016).
10. Proctor, M. J. *et al.* Systemic inflammation predicts all-cause mortality: a glasgow inflammation outcome study. *PLOS One* **10**, e0116206 (2015).
11. Prins, B. P. *et al.* Investigating the causal relationship of C-reactive protein with 32 complex somatic and psychiatric outcomes: A large-scale cross-consortium mendelian randomization study. *PLOS Medicine* **13**, e1001976 (2016).
12. Balayan, S. *et al.* Biosensor development for C-reactive protein detection: A review. *Applied Surface Science Advances* **12**, 100343 (2022).
13. Young, B., Gleeson, M. & Cripps, A. W. C-reactive protein: a critical review. *Pathology* **23**, 118–124 (1991).
14. Lobo, S. M. Sequential C-reactive protein measurements in patients with serious infections: does it help? *Critical Care* **16**, 130 (2012).
15. Guo, S., Mao, X. & Liang, M. The moderate predictive value of serial serum CRP and PCT levels for the prognosis of hospitalized community-acquired pneumonia. *Respiratory Research* **19**, 193 (2018).
16. Gao, W. *et al.* Fully integrated wearable sensor arrays for multiplexed in situ perspiration analysis. *Nature* **529**, 509–514 (2016).
17. Yang, Y. & Gao, W. Wearable and flexible electronics for continuous molecular monitoring. *Chemical Society Reviews* **48**, 1465–1491 (2019).
18. Ray, T. R. *et al.* Soft, skin-interfaced sweat stickers for cystic fibrosis diagnosis and management. *Science Translational Medicine* **13**, eabd8109 (2021).
19. Kim, J. *et al.* Wearable biosensors for healthcare monitoring. *Nature Biotechnology* **37**, 389–406 (2019).
20. Lee, H. *et al.* A graphene-based electrochemical device with thermoresponsive microneedles for diabetes monitoring and therapy. *Nature Nanotechnology* **11**, 566–572 (2016).

21. Koh, A. *et al.* A soft, wearable microfluidic device for the capture, storage, and colorimetric sensing of sweat. *Science Translational Medicine* **8**, 366ra165 (2016).
22. Ates, H. C. *et al.* On-site therapeutic drug monitoring. *Trends in biotechnology* **38**, 1262–1277 (2020).
23. Bariya, M., Nyein, H. Y. Y. & Javey, A. Wearable sweat sensors. *Nature Electronics* **1**, 160–171 (2018).
24. Parlak, O. *et al.* A. Molecularly selective nanoporous membrane-based wearable organic electrochemical device for noninvasive cortisol sensing. *Science Advances* **4**, eaar2904 (2018).
25. Tu, J. *et al.* The era of digital health: A review of portable and wearable affinity biosensors. *Advanced Functional Materials* **30**, 1906713 (2020).
26. Heikenfeld, J. *et al.* Accessing analytes in biofluids for peripheral biochemical monitoring. *Nature Biotechnology* **37**, 407–419 (2019).
27. Yang, Y. *et al.* A laser-engraved wearable sensor for sensitive detection of uric acid and tyrosine in sweat. *Nature Biotechnology* **38**, 217–224 (2020).
28. Yu, Y. *et al.* Biofuel-powered soft electronic skin with multiplexed and wireless sensing for human-machine interfaces. *Science Robotics* **5**, eaaz7946 (2020).
29. Sempionatto, J. R. *et al.* An epidermal patch for the simultaneous monitoring of haemodynamic and metabolic biomarkers. *Nature Biomedical Engineering*. **5**, 737–748 (2021).
30. Emaminejad, S. *et al.* Autonomous sweat extraction and analysis applied to cystic fibrosis and glucose monitoring using a fully integrated wearable platform. *Proceedings of the National Academy of Sciences of the United States of America USA* **114**, 4625–4630 (2017).
31. Bandodkar, A. J. *et al.* Wearable sensors for biochemical sweat analysis. *Annual Review of Analytical Chemistry* **12**, 1–22 (2019).
32. Xuan, X. *et al.* A. Lactate biosensing for reliable on-body sweat analysis. *ACS Sensors* **6**, 2763–2771 (2021).
33. Pirovano, P. *et al.* A wearable sensor for the detection of sodium and potassium in human sweat during exercise. *Talanta* **219**, 121145 (2020).

34. Garcia-Cordero, E. *et al.* Three-dimensional integrated ultra-low-volume passive microfluidics with ion-sensitive field-effect transistors for multiparameter wearable sweat analyzers. *ACS Nano* **12**, 12646–12656 (2018).
35. He, W. *et al.* Integrated textile sensor patch for real-time and multiplex sweat analysis. *Science Advances* **5**, eaax0649 (2019).
36. Choi, D.-H. *et al.* Out-of-clinic measurement of sweat chloride using a wearable sensor during low-intensity exercise. *npj Digital Medicine* **3**, 49 (2020).
37. Zhong, B. *et al.* Wearable sweat loss measuring devices: from the role of sweat loss to advanced mechanisms and designs. *Advanced Science* **9**, 2103257 (2022).
38. Lin, H. *et al.* A programmable epidermal microfluidic valving system for wearable biofluid management and contextual biomarker analysis. *Nature Communications* **11**, 4405 (2020).
39. Saldanha, D. J., Cai, A. & Dorval Courchesne, N.-M. The evolving role of proteins in wearable sweat biosensors. *ACS Biomaterials Science & Engineering* **9**, 2020-2047 (2021).
40. Mishra, R. K. *et al.* Continuous opioid monitoring along with nerve agents on a wearable microneedle sensor array. *Journal of the American Chemical Society* **142**, 5991–5995 (2020).
41. Wang, B. *et al.* Wearable aptamer-field-effect transistor sensing system for noninvasive cortisol monitoring. *Science Advances* **8**, eabk0967 (2022).
42. An, J. E. *et al.* Wearable cortisol aptasensor for simple and rapid real-time monitoring. *ACS Sensors* **7**, 99–108 (2022).
43. Torrente-Rodríguez, R. M. *et al.* Investigation of cortisol dynamics in human sweat using a graphene-based wireless mHealth system. *Matter* **2**, 921–937 (2020).
44. Jagannath, B. *et al.* Novel approach to track the lifecycle of inflammation from chemokine expression to inflammatory proteins in sweat using electrochemical biosensor. *Advanced Materials Technologies* **7**, 2101356 (2022).
45. Gao, Y. *et al.* A flexible multiplexed immunosensor for point-of-care in situ wound monitoring. *Science Advances* **7**, eabg9614 (2021).
46. Barkas, F. *et al.* Electrolyte and acid-base disorders in inflammatory bowel disease. *Annals of Gastroenterology* **26**, 23–28 (2013).

47. Majewski, S. *et al.* Skin condition and its relationship to systemic inflammation in chronic obstructive pulmonary disease. *International Journal of Chronic Obstructive Pulmonary Disease* **12**, 2407–2415 (2017).
48. Yang, X. *et al.* Graphene uniformly decorated with gold nanodots: in situ synthesis, enhanced dispersibility and applications. *Journal of Materials Chemistry* **21**, 8096–8103 (2011).
49. Yu, Y. *et al.* All-printed soft human-machine interface for robotic physicochemical sensing. *Science Robotics* **7**, eabn0495 (2022).
50. Harshman, S. W. *et al.* The proteomic and metabolomic characterization of exercise-induced sweat for human performance monitoring: A pilot investigation. *PLoS One* **13**, e0203133 (2018).
51. Pinto-Plata, V. M. *et al.* C-reactive protein in patients with COPD, control smokers and non-smokers. *Thorax* **61**, 23–28 (2006).
52. Retamales, I. *et al.* Amplification of inflammation in emphysema and its association with latent adenoviral infection. *American Journal of Respiratory and Critical Care Medicine* **164**, 469–473 (2001).
53. Tonstad, S. & Cowan, J. L. C-reactive protein as a predictor of disease in smokers and former smokers: a review. *International Journal of Clinical Practice* **63**, 1634–1641 (2009).
54. Simmonds, S. J. *et al.* Cellular and molecular differences between HFpEF and HFrfEF: a step ahead in an improved pathological understanding. *Cells* **9**, 242 (2020).
55. Lakhani, I. *et al.* Diagnostic and prognostic value of serum C-reactive protein in heart failure with preserved ejection fraction: a systematic review and meta-analysis. *Heart Failure Reviews* **26**, 1141–1150 (2021).
56. Butler, J. *et al.* Clinical and economic burden of chronic heart failure and reduced ejection fraction following a worsening heart failure event. *Advances in Therapy* **37**, 4015–4032 (2020).
57. Albar, Z. *et al.* Inflammatory markers and risk of heart failure with reduced to preserved ejection fraction. *American Journal of Cardiology* **167**, 68–75 (2022).
58. Xin, Y. *et al.* Design strategies for strain-Insensitive wearable healthcare sensors and perspective based on the seebeck coefficient. *Advanced Electronic Materials* **9**, 2200534 (2023).

59. Wang, M. *et al.* A wearable electrochemical biosensor for the monitoring of metabolites and nutrients. *Nature Biomedical Engineering* **6**, 1225–1235 (2022).
60. Bandodkar, A. J. *et al.* Battery-free, skin-interfaced microfluidic/electronic systems for simultaneous electrochemical, colorimetric, and volumetric analysis of sweat. *Science Advances* **5**, eaav3294 (2019).
61. Torrente-Rodríguez, R. M. *et al.* SARS-CoV-2 RapidPlex: A graphene-based multiplexed telemedicine platform for rapid and low-cost COVID-19 diagnosis and monitoring. *Matter* **3**, 1981–1998 (2020).
62. Zhuang, G. *et al.* Measurement of association rate constant of antibody-antigen interaction in solution based on enzyme-linked immunosorbent assay. *Journal of Bioscience and Bioengineering* **92**, 330–336 (2001).

Appendix A

SUPPLEMENTARY INFORMATION FOR CHAPTER 3

Materials from this chapter appear in “Tu, J.; Min, J.; Song, Y.; Xu, C.; Li, J.; Moore, J.; Hanson, J.; Hu, E.; Parimon, T.; Wang, T.-Y.; Davoodi, E.; Chou, T.-F.; Chen, P.; Hsu, J. J.; Rossiter, H. B.; Gao, W. A wireless patch for the monitoring of C-reactive protein in sweat. *Nature Biomedical Engineering* 14 (2023) doi:10.1038/s41551-023-01059-5.”

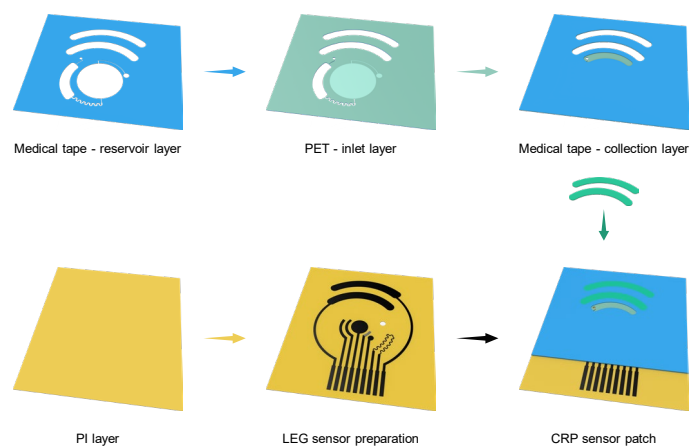


Figure A-1. Fabrication process of the microfluidic multimodal sensor patch.

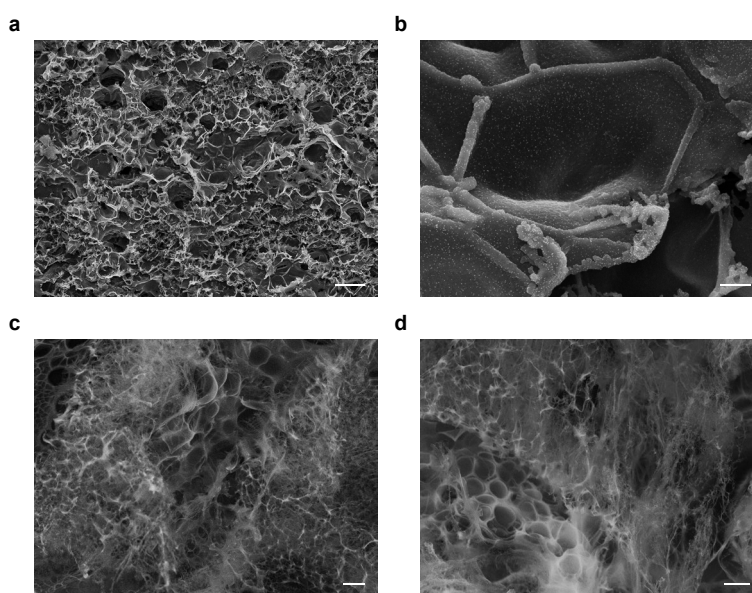


Figure A-2. SEM images of the LEG electrodes. a,b, The raster-mode engraved graphene (**a**) and the LEG-AuNPs composite (**b**) for CRP sensing. Scale bars, 10 μm (**a**) and 1 μm (**b**). **c,d,** SEM images of vector-mode engraved LEG electrodes for pH sensing (**c**) and temperature sensing (**d**). Scale bars, 2 μm .

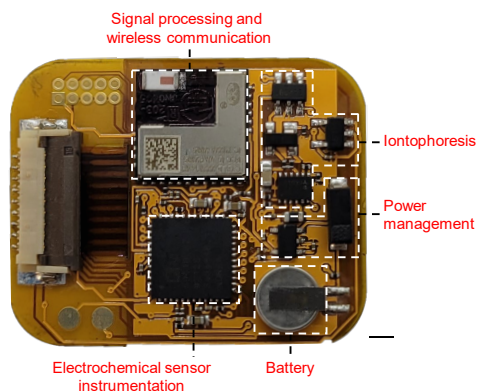


Figure A-3. The integrated wireless wearable electronics for CRP sensing. Scale bar, 5 mm.

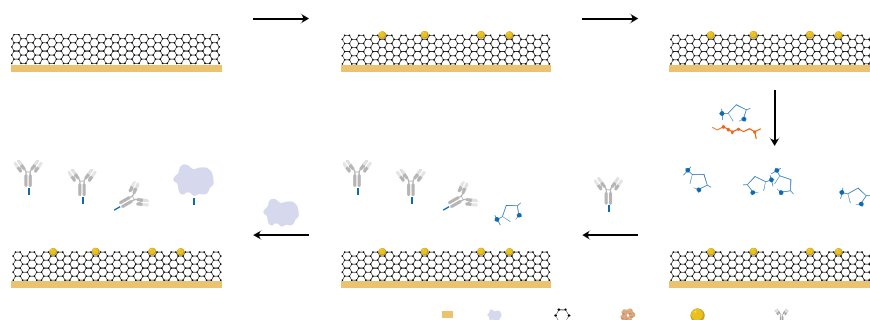


Figure A-4. Surface functionalization process of the working electrode of CRP sensor.

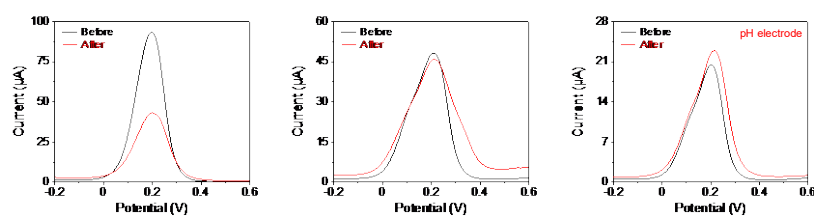


Figure A-5. Influence of the self-assembled monolayer (SAM) modification on electrode performance. **a–c**, DPV voltammograms of a working electrode (WE) (**a**), an IMP electrode (**b**), and a pH electrode (**c**) in 0.1 M KCl solution containing 5.0 mM $K_4Fe(CN)_6/K_3Fe(CN)_6$ after immersion in 0.5 mM MUA and 1 mM MCH in proof 200 ethanol overnight for SAM formation.

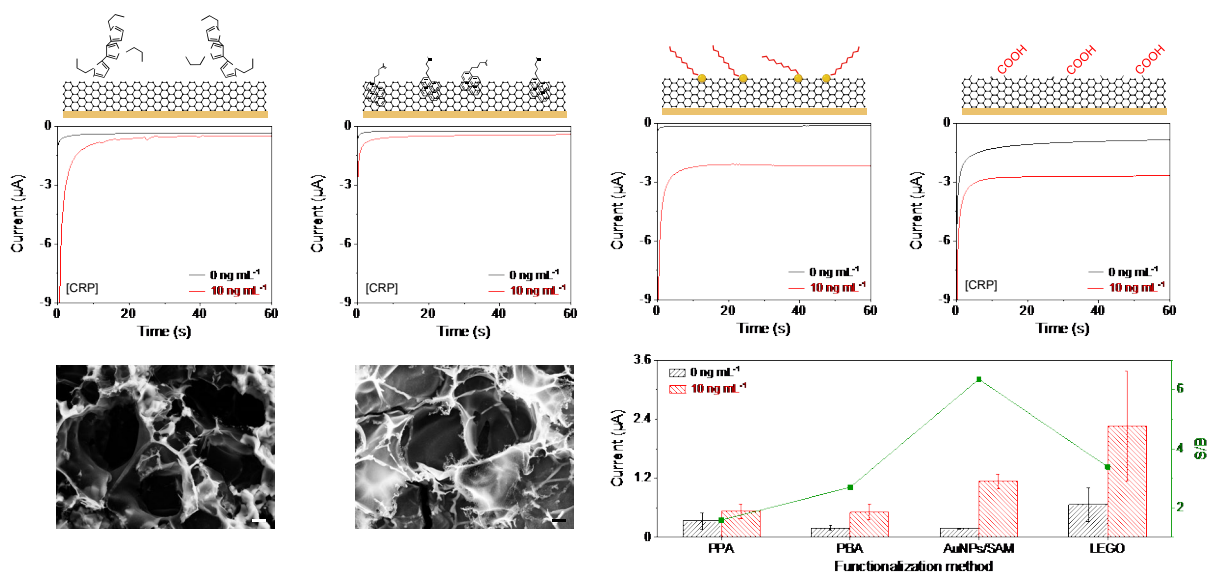


Figure A-6. Electrochemical performance of the LEG CRP sensors prepared by different functionalization methods. a–f, Amperometric responses and SEM images of CRP sensors based on the LEG modified with PPA (a,b), PBA (c,d); AuNPs/SAM (e), graphene oxide (LEGO) (f). Scale bars in b and d, 2 μm . g, Sensor performance comparison of different functionalization methods. Error bars represent the s.d. from 3 sensors. PPA, poly(pyrrolepropionic acid); PBA, pyrenebutyric acid; AuNP/SAM, LEG-AuNPs composite modified with thiol self-assembly monolayer; LEGO, laser-engraved graphene oxide by electrochemical oxidation. S/B, signal to background ratio.

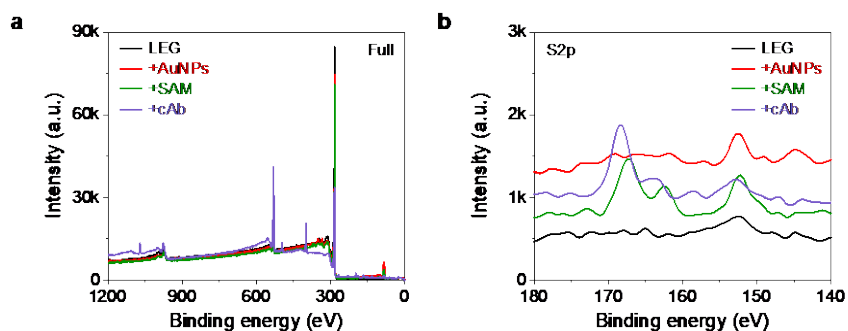


Figure A-7. Characterization of the CRP sensor functionalization using XPS. a,b, Full range (a) and s2p (b) XPS spectra of the LEG-AuNPs CRP sensor obtained after each modification step.

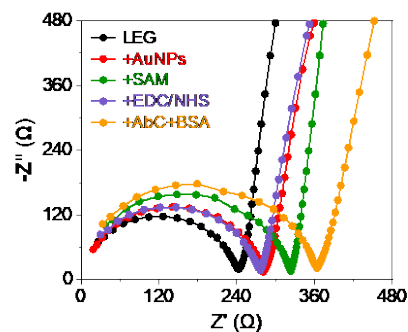


Figure A-8. Electrochemical impedance spectroscopy (EIS) for the LEG-AuNPs CRP sensor after each surface modification step. EIS tests were performed in a solution containing 0.1 M KCl and 5 mM $[\text{Fe}(\text{CN})_6]^{3-}$ at open circuit potentials with an alternating current amplitude of 5 mV in the range of 0.1–1000000 Hz.

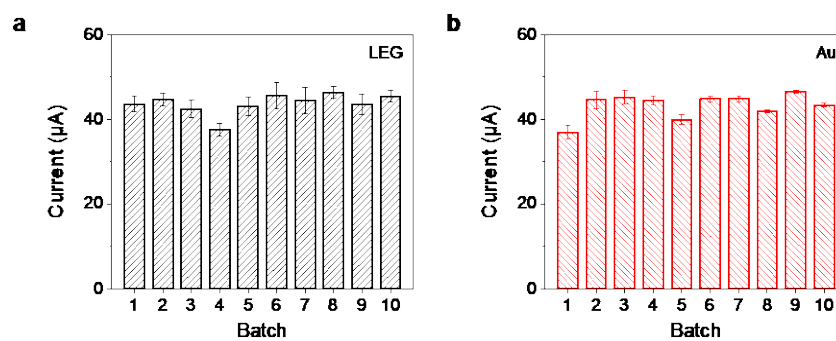


Figure A-9. Batch to batch variations in electrochemical performance of the LEG electrodes and LEG-AuNPs electrodes. a,b, Oxidation peak heights in the cyclic voltammograms (CVs) of the LEG electrodes (a) and LEG-AuNPs electrodes (b) 0.1 M KCl and 5 mM $[\text{Fe}(\text{CN})_6]^{3-}$. Scan rate, 50 mV s^{-1} . Error bars represent the s.d. from 3 sensors.

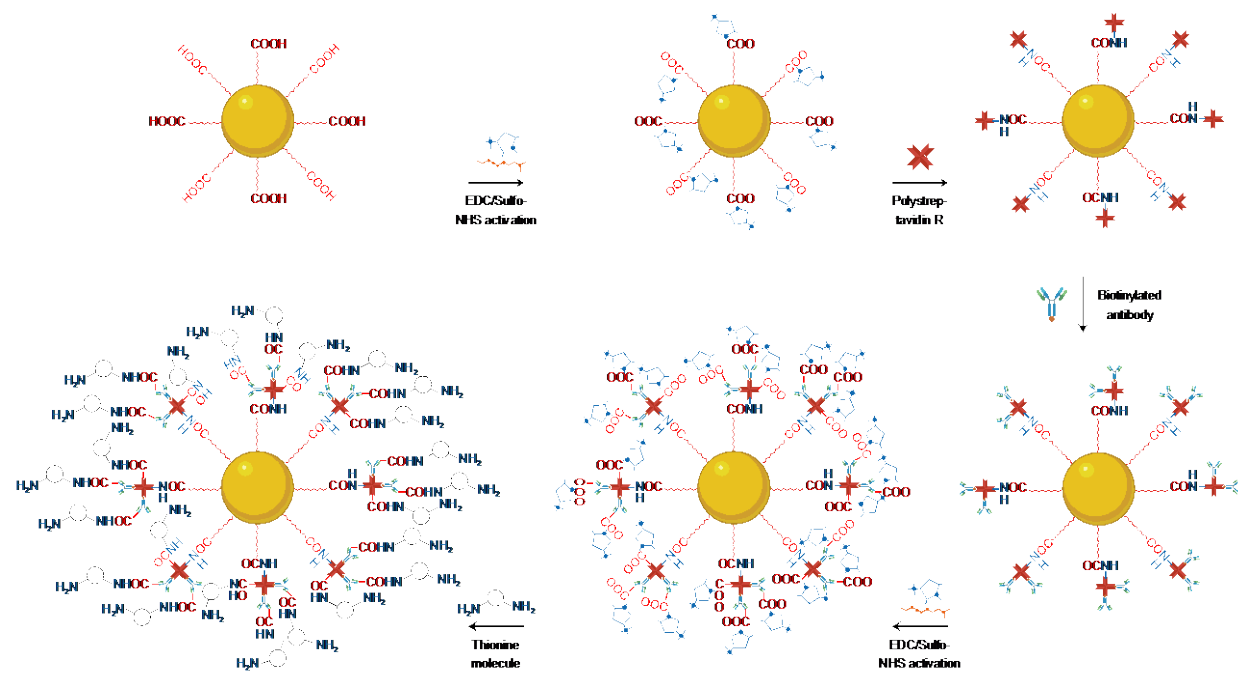


Figure A-10. Conjugation process of the dAb-conjugated AuNPs complex for signal amplification.

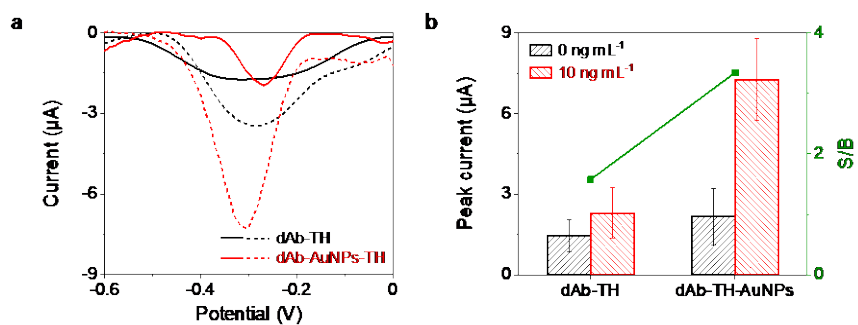


Figure A-11. Comparison of the electrochemical performances of redox probe conjugated dAb and dAb-conjugated AuNPs. a,b, SWV voltammograms (a) and the corresponding peak currents (b) of the CRP sensors modified with redox probe conjugated dAb and dAb-conjugated AuNPs. Solid lines and dotted lines represent the sensor responses in 0 and 10 ng mL^{-1} CRP, respectively. Error bars represent the s.d. from 3 sensors.

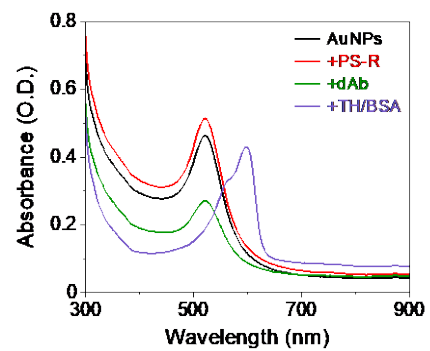


Figure A-12. UV-Vis absorbance of the dAb-AuNP conjugate after each modification step.

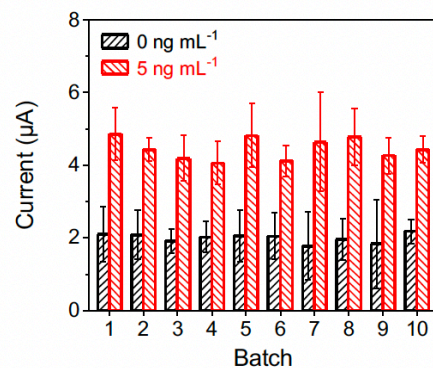


Figure A-13. The reproducibility of the CRP sensor. The detection was performed in 1X PBS (pH 7.4) in the presence of 0 and 5 ng mL⁻¹ CRP (10 batches for each concentration). Error bars represent the s.d. from 3 electrodes.

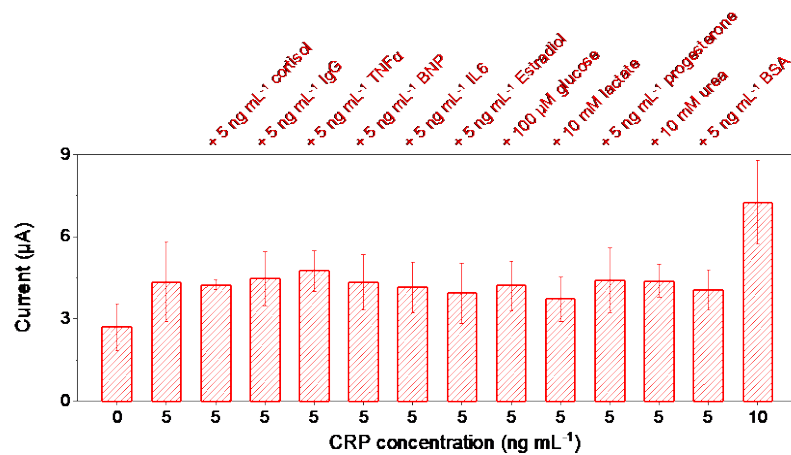


Figure A-14. Selectivity of the CRP sensor to potential interferences in sweat. Error bars represent the s.d. from 3 sensors.

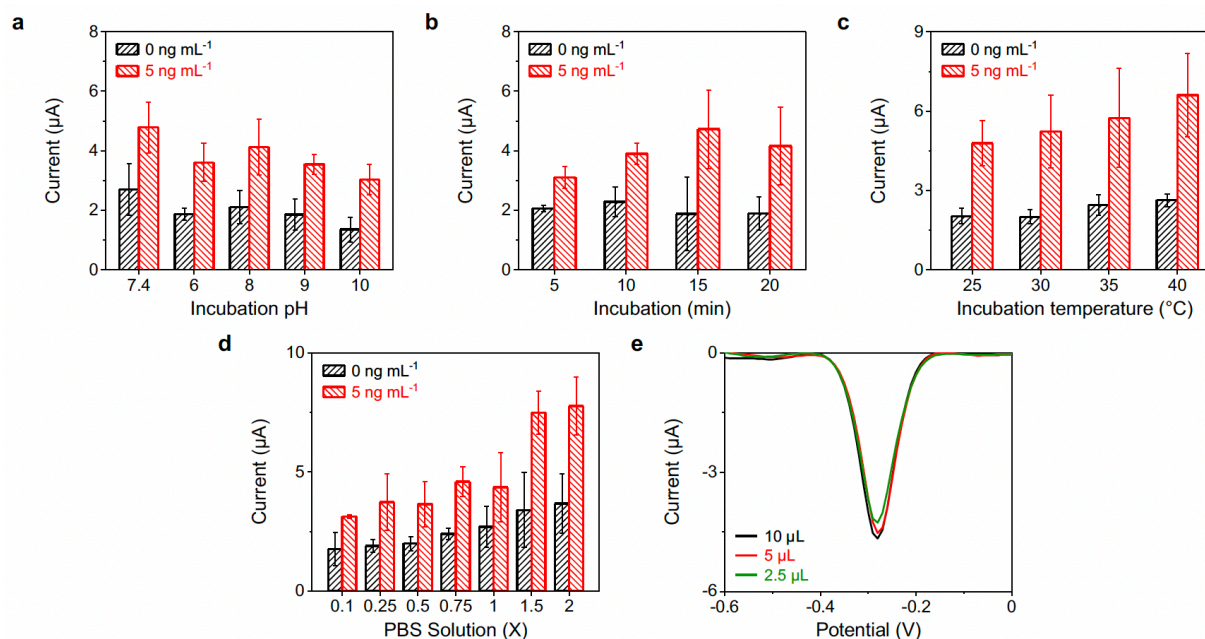


Figure A-15. The influence of incubation pH, time, temperature, sample volume, and detection ionic strength on the CRP sensor responses. **a–d**, Reduction peak current height in the SWV voltammograms of the CRP sensors with 0 and 5 ng mL⁻¹ CRP and 1% BSA incubated in 1X PBS (pH 6–10) for 15 min under 25°C (**a**), in 1X PBS (pH 7.4) for 1 to 30 minutes under 25°C (**b**), and in 1X PBS (pH 7.4) under 25–35 °C (**c**). The detection was performed in 1X PBS (pH 7.4) under 25°C. **d**, Reduction peak current height in the SWV voltammograms of the CRP sensors obtained in PBS with various ionic strengths after incubation in 1X PBS (pH 7.4) for 15 minutes under 25°C. **e**, SWV voltammograms of the CRP sensors after incubation with different sample volume. Error bars represent the s.d. from 3 sensors. **e**, SWV voltammograms of the CRP sensors at 5 ng mL⁻¹ with different incubation volumes (10, 5, 2.5 µL).

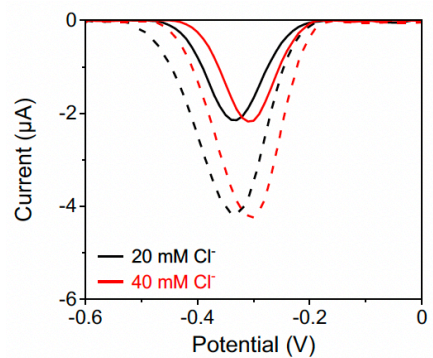


Figure A-16. SWV voltammograms of the CRP sensors in CRP solutions with varying Cl⁻ concentrations. Solid and dotted lines represent SWV voltammograms obtained in 0 and 5 ng mL⁻¹ CRP (PBS, pH 7.4), respectively.

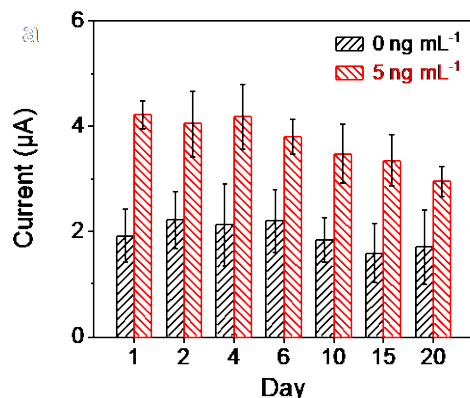


Figure A-17. The stability of the CRP sensor. The prepared CRP sensors were stored in the refrigerator for 1–20 days. The detection was performed in 1X PBS (pH 7.4) in presence of 0 and 5 ng mL⁻¹ CRP. Error bars represent the s.d. from 3 sensors.

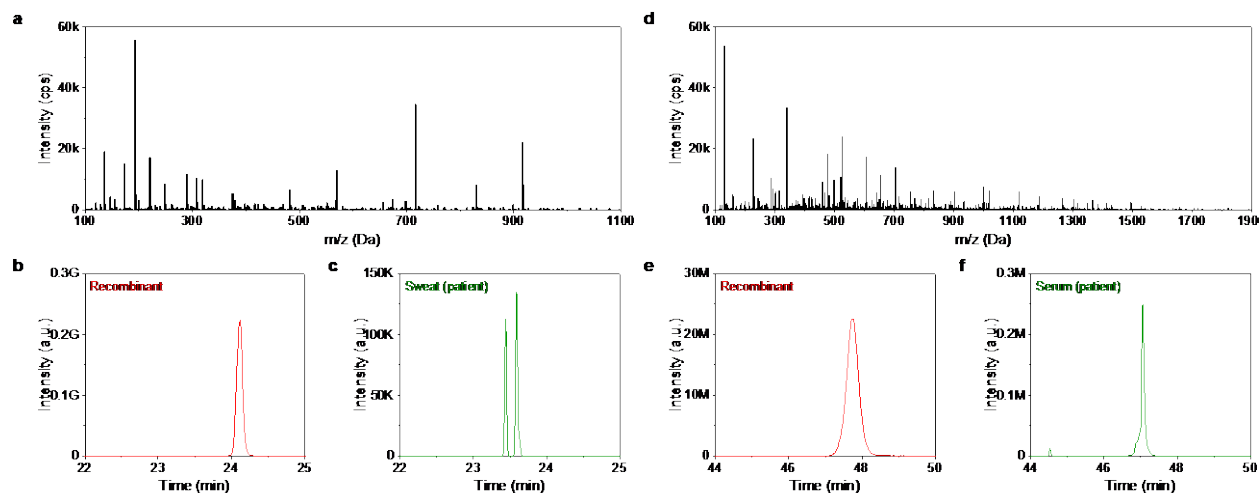


Figure A-18. Representative mass spectra of CRP derived peptides and chromatograms. **a**, MS2 spectrum of the 568.8 doubly charged ion of GYSIFSYATK CRP-derived peptide. **b**, Chromatogram of GYSIFSYATK peptide in recombinant CRP digests. **c**, Chromatogram of GYSIFSYATK peptide tracking CRP in iontophoretic sweat digests from COPD patients. **d**, MS2 spectrum of the 513.2 doubly charged ion of ALKYEYVQGEVFTKPQLWP CRP-derived peptide. **e**, Chromatogram of ALKYEYVQGEVFTKPQLWP peptide in recombinant CRP digests. **f**, Chromatogram of ALKYEYVQGEVFTKPQLWP peptide tracking CRP in serum digests from COPD patients.

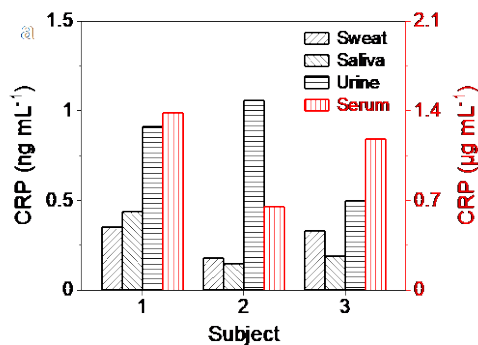


Figure A-19. CRP levels in serum, sweat, saliva, and urine. All samples were collected within a 30-min time window from healthy human subjects.

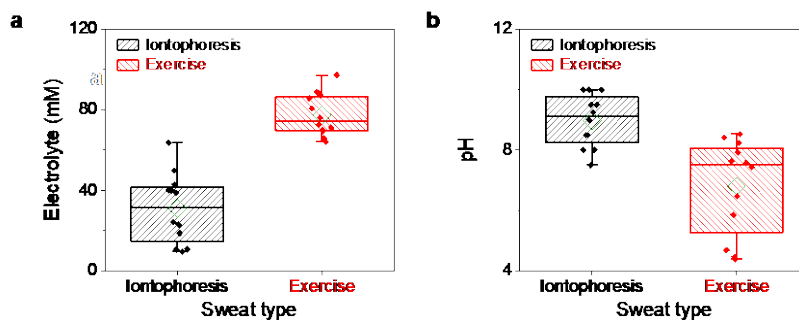


Figure A-20. Box-and-whisker plot of sweat electrolyte and pH levels between iontophoresis and exercise sweat. The bottom whisker represents the minima; the top whisker represents the maxima; the square in the box represents the mean. Error bars represent the s.d. of the mean from 12 sweat samples.

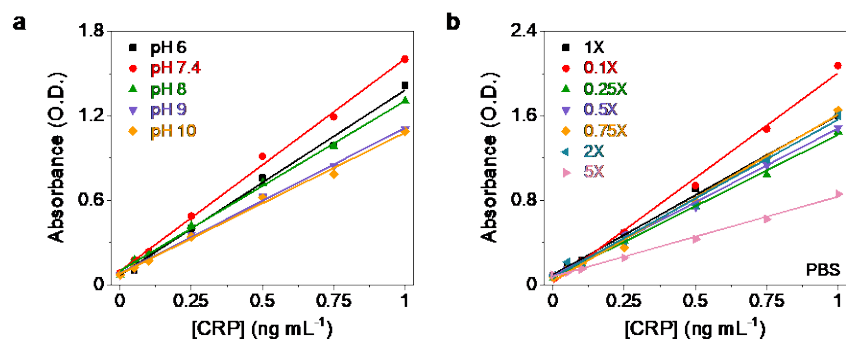


Figure A-21. The influence of electrolyte concentration and pH on the antigen capturing measured with ELISA.

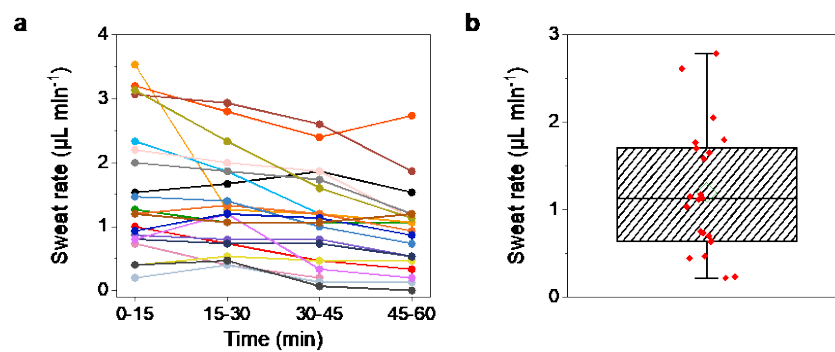


Figure A-22. Sweat rate of current and former smokers with and without COPD after 5 minutes of iontophoretic sweat induction. a, Time-dependent sweat rate fluctuation after an iontophoresis process. **b,** Sweat rate variations among the human subjects (averaged in the first 15 minutes after the iontophoresis). Error bars represent the s.d. from 24 human subjects.

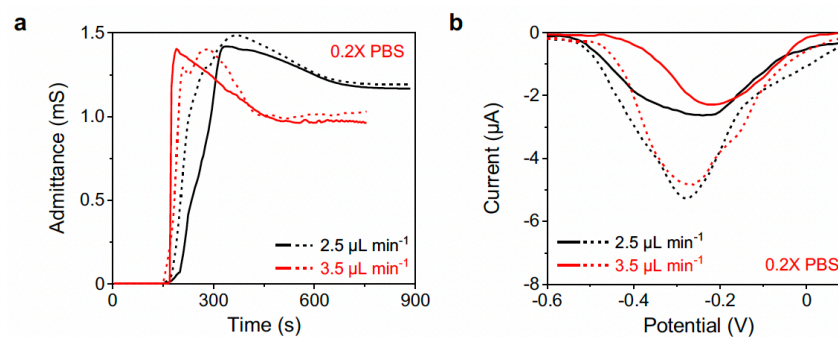


Figure A-23. Influence of the high flow rates on microfluidic automatic CRP sensing. Solid and dotted lines represent results obtained in artificial sweat (0.2X PBS) containing 1 and 5 ng mL^{-1} CRP, respectively.

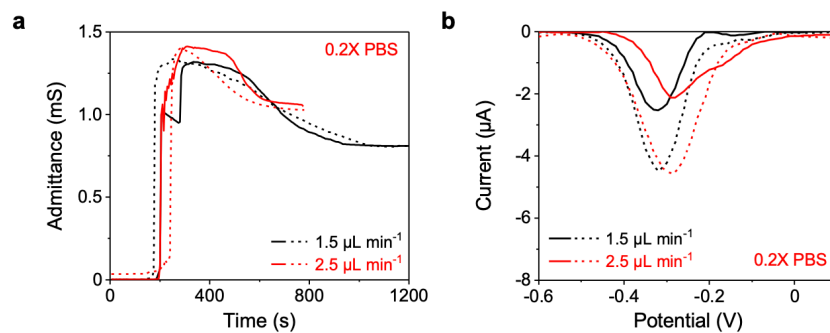


Figure A-24. Influence of the interferent molecules on microfluidic automatic CRP sensing. 10 mM lactate, 20 mM urea, and 1 ng mL⁻¹ cortisol were added to 1 ng mL⁻¹ and 5 ng mL⁻¹ CRP solutions. Solid and dotted lines represent results obtained in artificial sweat (0.2X PBS) containing 1 and 5 ng mL⁻¹ CRP, respectively.

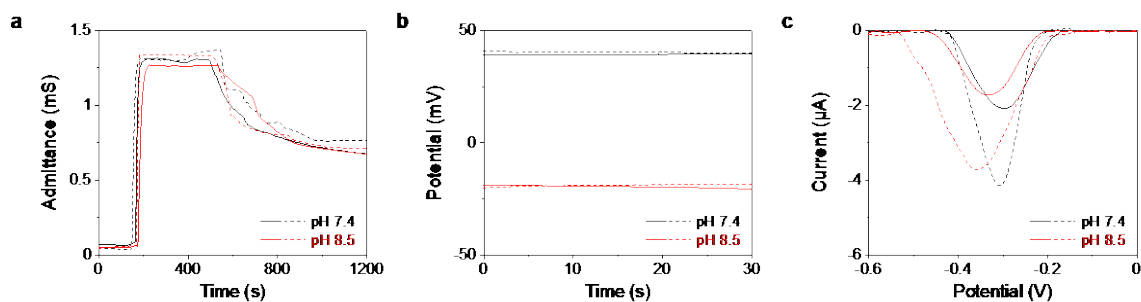


Figure A-25. Flow test characterization of the multimodal sensor patch in response to different initial pHs. a–c, Response of ionic strength sensors (a), pH sensors (b) and CRP sensors (c) at a flow rate of $1.5 \mu\text{L min}^{-1}$ in artificial sweat (0.2X PBS pH 7.4 or pH 8.5). Solid and dotted lines represent tests performed in 1 and 5 ng mL^{-1} CRP, respectively.

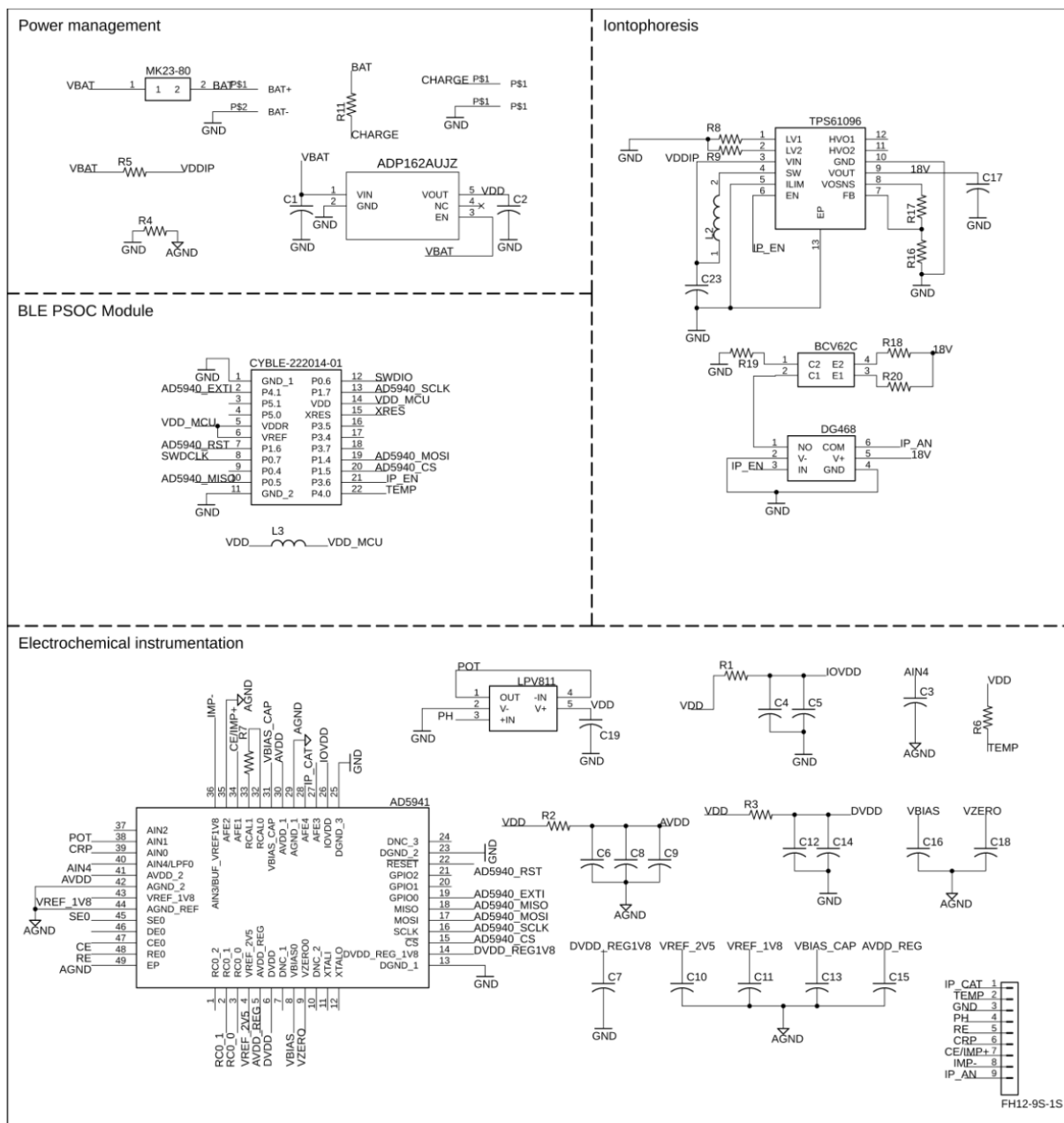


Figure A-26. Detailed circuit schematic of the InflaStat.

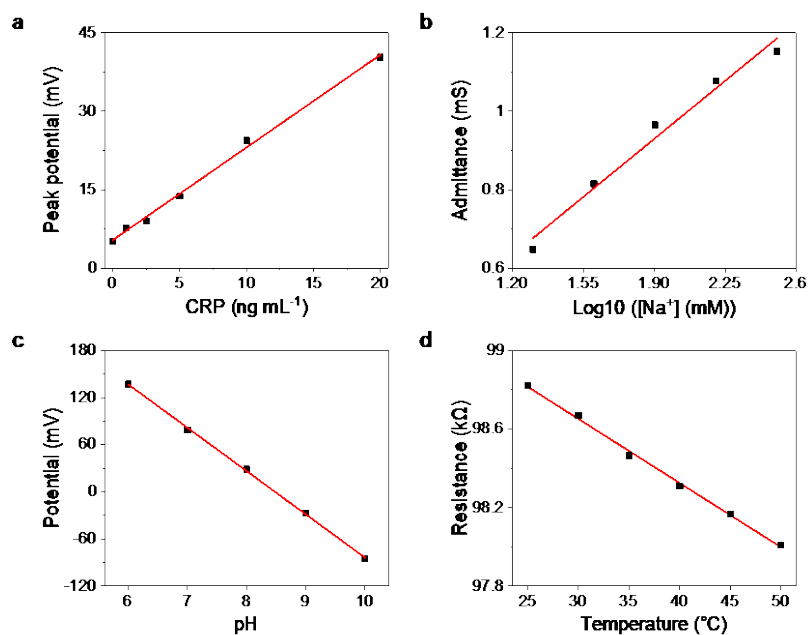


Figure A-27. LEG-based sensor calibration plots obtained with the InflaStat. a–d, Calibration plot of the CRP (a), ionic strength (b), pH (c), and temperature (d) sensors. The data corresponds to Fig. 5c–f.

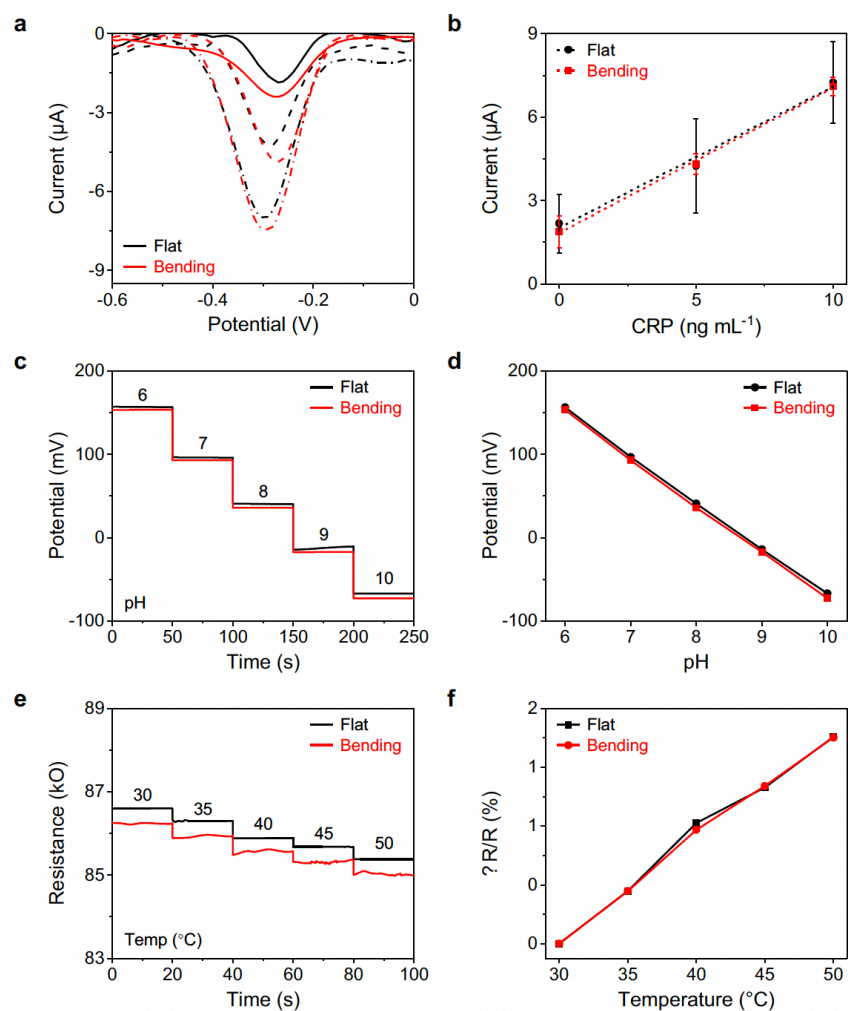


Figure A-28. Performance of the CRP, pH, and temperature sensors under mechanical deformation. **a,b** SWV voltammograms (**a**) and the corresponding calibration plots (**b**) of the CRP sensors under mechanical deformation in 1X PBS (pH 7.4) with 0–20 ng mL⁻¹ CRP and 1% BSA. Error bars represent the s.d. from 3 sensors. **c,d** Potentiometric measurements (**c**) and calibration plot (**d**) of the pH sensors under mechanical deformation in 1X PBS (pH 6–10). **e,f**, Response (**e**) and calibration plot (**f**) of the resistive temperature sensor under mechanical deformation in the physiological temperature range. Radius of bending curvature, 5 cm.

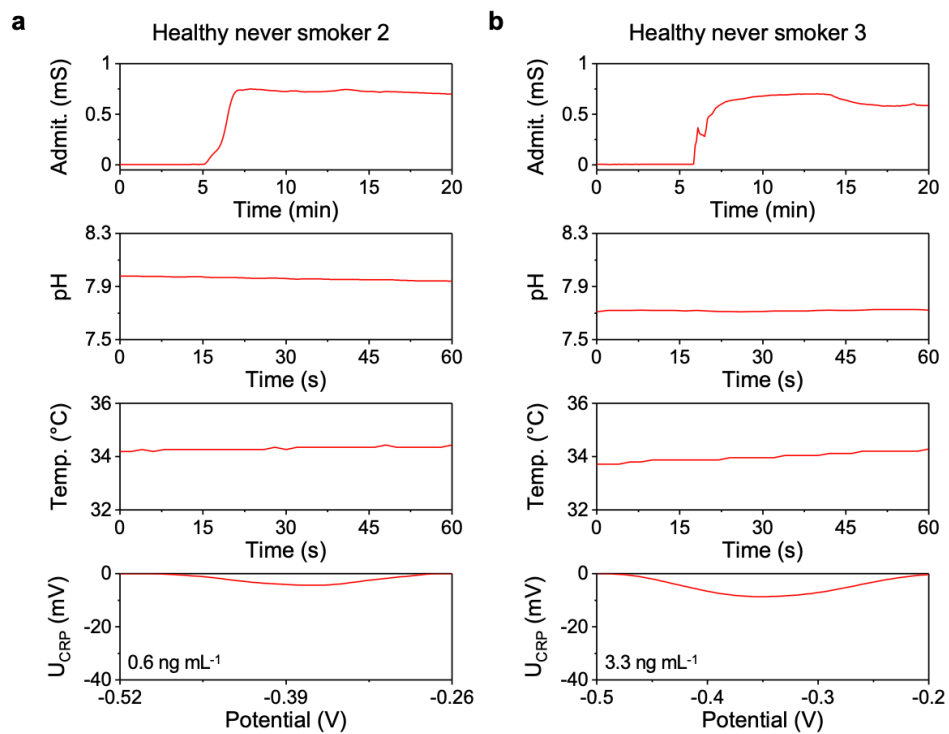


Figure A-29. On-body evaluation of the wearable sensor on healthy never smokers.

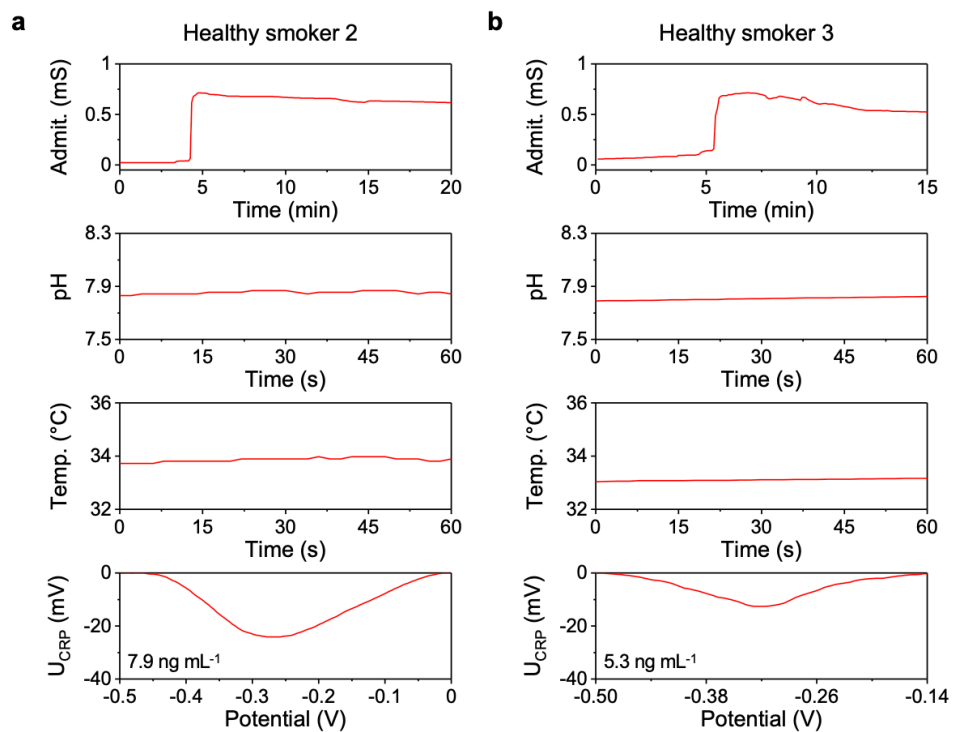


Figure A-30. On-body evaluation of the wearable sensor on healthy smokers.

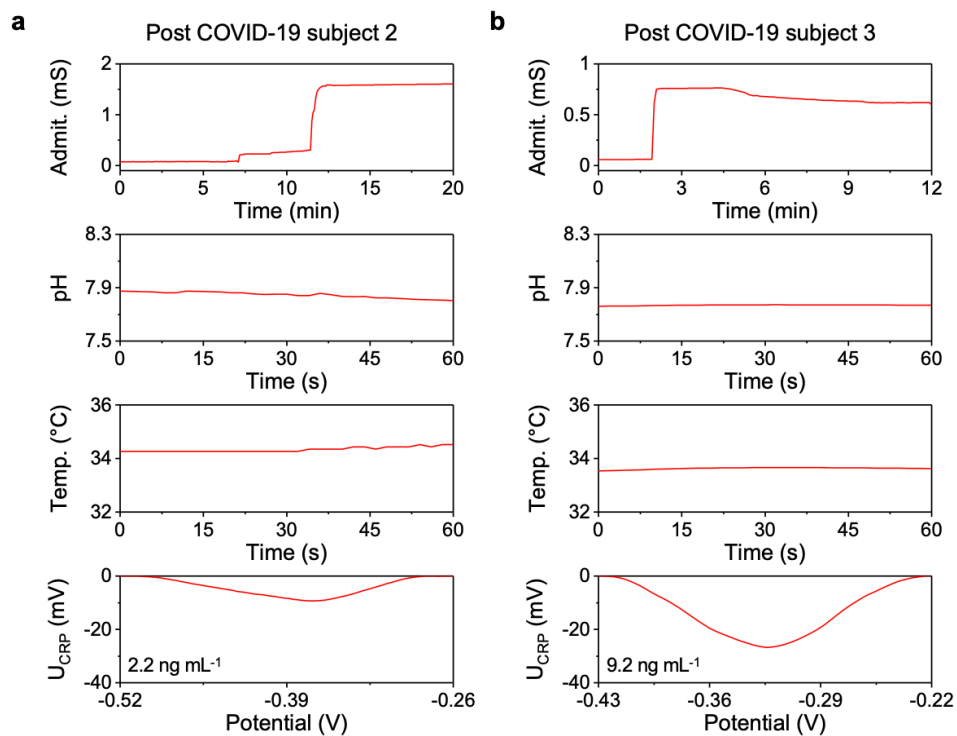


Figure A-31 On-body evaluation of the wearable sensor on post-COVID subjects.

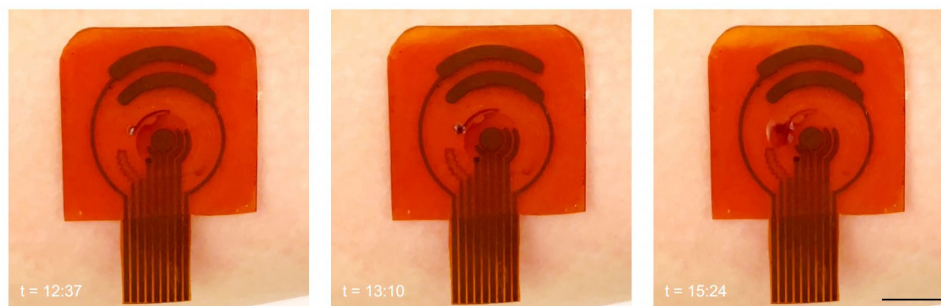


Figure A-32. Time-lapse images showing the automatic microfluidic reagent routing and washing. Scale bar, 5 mm.

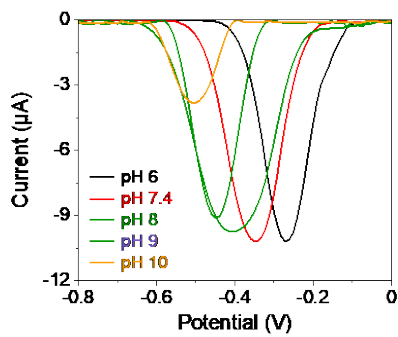


Figure A-33. Influence of solution pH in peak potential and current of the redox molecule thionine. SWV voltammograms were obtained using the LEG electrodes in 5 μM TH in 1X PBS.

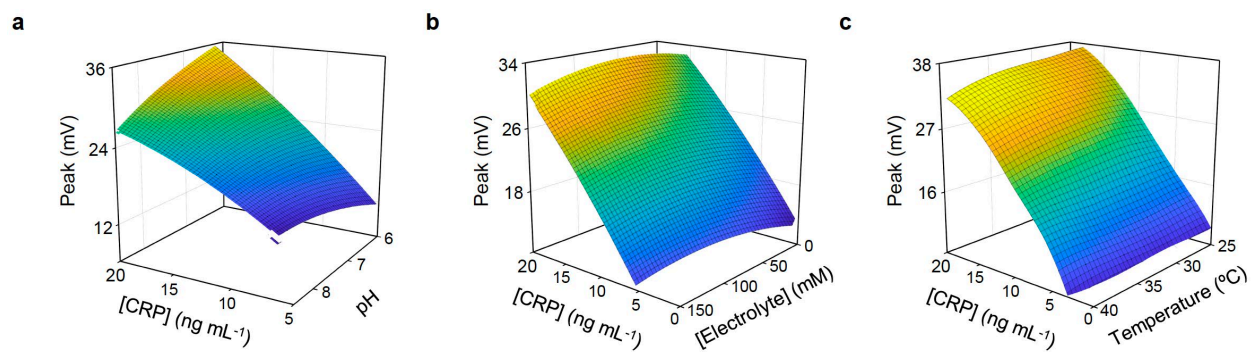


Figure A-34. Influence of the pH, ionic strength, and temperature on the CRP sensor reading.
a–c, Color maps showing the dependence of the CRP sensor response on pH (a), electrolyte (b), and temperature (c) levels.

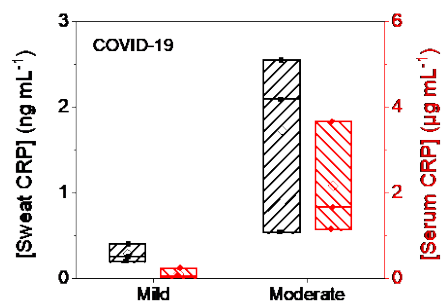


Figure A-35. Box-and-whisker plot of CRP levels in sweat and serum samples from post-COVID subjects with mild and moderate symptoms. The bottom whisker represents the minima; the top whisker represents the maxima; the square in the box represents the mean ($n=3$ for each group).

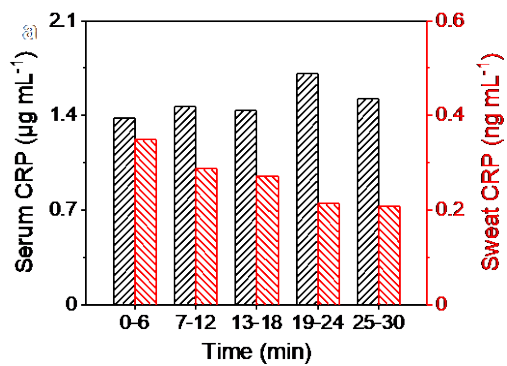


Figure A-36. Evaluation of system reproducibility *via* dynamic monitoring of sweat and blood CRP. Sweat and blood samples were sampled simultaneously from a healthy subject after iontophoresis.

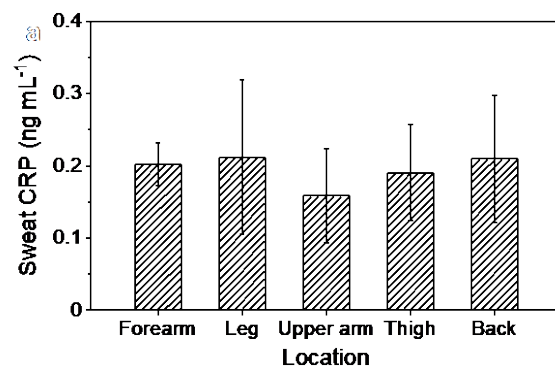


Figure A-37. Evaluation of sweat CRP levels across anatomic locations. Error bars represent the s.d. from 3 healthy subjects.

Product	Company	Turnaround time	Detection range
CRP, high Sensitivity (TEST: 120766)	LabCorp	Within 1 day	N/A
CRP, High Sensitivity, blood Level Lab Test (Epic Code LAB150)	Spectrum Health	1 day	N/A
Human CRP ELISA Kit (ab99995)	Abcam	4 h 45 min to overnight	34.29 - 25000 pg mL ⁻¹
CRP Human ELISA Kit # KHA0031	Invitrogen	4 h	18.75 - 1200 pg mL ⁻¹
Human CRP ELISA Kit (DEIA1407-M2)	Creative Diagnostics	3 h 20 min	31.25 - 2000 pg mL ⁻¹
Human CRP DuoSet ELISA (DY1707)	R&D Systems	Overnight	15.6 - 1000 pg mL ⁻¹
Human CRP ELISA Kit MBS2021863	MyBioSource	3 h	62.5 - 4000 pg mL ⁻¹
RayBio® Human CRP ELISA Kit (ELH-CRP-1)	Raybiotech	4 h 45 min	34 - 25000 pg mL ⁻¹

Table A-1 Commercial CRP kits and laboratory tests that can perform ng-level CRP detection.

Product	Company	Sample	Detection range	Equipment/portability
AFINION™ 2	Abbot	Whole blood/Serum	5 – 200 mg L ⁻¹	7.5 lbs analyzer
Tina-quant® w cobas c111 analyzer	Roche	Serum/Plasma	0.3 – 350 mg L ⁻¹	85.1 lbs analyzer
PATHFAST™ Immunoanalyzer	Mitsubishi Chemical	Whole blood/Serum/Plasma	0.05 – 30 µg mL ⁻¹	28 kg analyzer
AFIAS-6	Boditech	Whole blood/Serum/Plasma	0.5 – 200 mg L ⁻¹	15.1 kg analyzer
iChroma II	Boditech	Whole blood/Serum/Plasma	2.5 – 300 mg L ⁻¹	1.3 kg analyzer
AQT90 Flex	Radiometer	Whole blood/Plasma	5 – 500 mg L ⁻¹	35 kg
SMART 700/546	Eurolyser	Whole blood/Serum/Plasma	2 – 240 mg L ⁻¹	3.4 kg
CUBE-S	Eurolyser	Whole blood/Serum/Plasma	2 – 240 mg L ⁻¹	2.4 kg
Microsemi LC-667G	Horiba	Whole blood/Serum/Plasma	0 – 200 mg L ⁻¹	19 kg
Innovastar®	Diagnostic Systems GmbH	Whole blood/Plasma	5 – 400 mg L ⁻¹	4 kg
Spinit®	Biosurfit SA	Whole blood/Serum/Plasma	2 – 300 mg L ⁻¹	4.1 kg
QuickRead go	Aidian	Whole blood/Serum/Plasma	5 – 200 mg L ⁻¹	1.7 kg
Nano-Check™	Nano-Ditech	Whole blood/Serum/Plasma	0.5 – 20 mg L ⁻¹	Light LFA strip

Table A-2 | Commercial point-of-care CRP monitors.

Peptide sequence	m/z	z	Peptide sequence	m/z	z	Peptide sequence	m/z	z	Peptide sequence	m/z	z
AFTVCIHF YTEISSTR	644.6	3	ALKYEVQGE VFTKPQLWP	1067.16	2	GYSIFSYATKR QDNEILIFWSK	889.5	3	QDNEIL IFWSK	464.9	3
AFTVCIHF YTEISSTR	966.5	2	APITKPKAFTV CIHFYTEISSTR	927.5	3	GYSIFSYATKR QDNEILIFWSK	1333.7	2	QDNEIL IFWSK	696.9	2
AFTVCIHFYTEIS STRGYSIFSYATK	998.2	3	APITKPKAFTV CIHFYTEISSTR	1390.7	2	IICFVITSISH AFGQTDMSR	799.4	3	QTDMSR	360.6	2
AFTVCIHFYTEIS STRGYSIFSYATK	1525.2	2	APLTKPLK	434.3	2	IICFVITSISH AFGQTDMSR	1198.6	2	QTDMSR	368.6	2
AFTVCIHFYTEISS TRGYSIFSYATKR	1050.2	3	APLTKPKAFTV CLHFYTELSSTR	927.5	3	IICFVITSISHA FGQTDMSRK	842.1	3	QTDMSR	369.2	2
AFTVCIHFYTEISS TRGYSIFSYATKR	1603.3	2	APLTKPKAFTV CLHFYTELSSTR	1390.7	2	IICFVITSISHA FGQTDMSRK	1262.7	2	QTDMSRK	424.7	2
AFTVCLHF YTELSSTR	644.6	3	EKIICFVITSIS HAFGQTDMSR	885.1	3	IICFVITSISHAFG QTDMSRKAFVFPK	1071.9	3	QTDMSRK	433.2	2
AFTVCLHF YTELSSTR	966.5	2	EKIICFVITSIS HAFGQTDMSR	1327.2	2	IICFVITSISHAFG QTDMSRKAFVFPK	1607.4	2	QTDMSR KAFVFPK	513.3	3
AFTVCLHFYTELS STRGYSIFSYATK	1017.2	3	EKIICFVITSISH AFGQTDMSRK	927.8	3	KAFVFPK	418.8	2	QTDMSR KAFVFPK	518.9	3
AFTVCLHFYTELS STRGYSIFSYATK	1525.2	2	EKIICFVITSISH AFGQTDMSRK	1391.2	2	KAFVFPKES DTSYVSLK	649.3	3	QTDMSR KAFVFPK	769.4	2
AFVFPK	354.7	2	ESDTSYV SIKAPITK	546.9	3	KAFVFPKES DTSYVSLK	973.5	2	QTDMSR KAFVFPK	777.9	2
AFVFPKESDT SYVSIKAPITK	776.8	3	ESDTSYV SIKAPITK	819.9	2	KSLKK	302.2	2	QTDMSR KAFVFPK	785.9	2
AFVFPKESDT SYVSIKAPITK	1164.6	2	ESDTS YVSLK	376.9	3	MEKIICFVITSIS HAFGQTDMSR	928.8	3	RQDNEI LIFWSK	516.9	3
AFVFPKES DTSYVSLK	606.6	3	ESDTS YVSLK	564.8	2	MEKIICFVITSIS HAFGQTDMSR	1392.7	2	RQDNEI LIFWSK	774.9	2
AFVFPKES DTSYVSLK	909.5	2	ESDTSYVSL KAPLTKPLK	659.7	3	MEKIICFVITSIS HAFGQTDMSRK	971.5	3	VRKSLK	365.8	2
AFVFPKESDTSY VSLKAPLTKPLK	889.5	3	ESDTSYVSL KAPLTKPLK	989.1	2	MEKIICFVITSIS HAFGQTDMSRK	1456.7	2	YEVQG EVFTK	400.5	3
AFVFPKESDTSY VSLKAPLTKPLK	1333.7	2	GYSIF SYATK	379.5	3	PIKAFTVCIH FYTEISSTR	757.4	3	YEVQG EVFTK	600.3	2
AIKYEYVQ GEVFTK	504.6	3	GYSIF SYATK	568.8	2	PIKAFTVCIH FYTEISSTR	1135.6	2	YEVQGEVF TKPQLWP	607.6	3
AIKYEYVQ GEVFTK	756.4	2	GYSIFS YATKR	431.6	3	PIKAFTVCIHFYTEI SSTRGYSIFSYATK	1129.9	3	YEVQGEVF TKPQLWP	910.9	2
ALKYEVQGE VFTKPQLWP	711.7	3	GYSIFS YATKR	646.8	2	PIKAFTVCIHFYTEI SSTRGYSIFSYATK	1694.4	2			

Table A-3. Inclusion list of precursor ions used for targeted CRP protein.

Study ID	COPD	Sex	Age	BMI	Smoking condition	GOLD* classification	Serum CRP ($\mu\text{g mL}^{-1}$)	Sweat CRP (ng mL^{-1})
1	Non-COPD	M	55	28.69	Former	0	3.52	9.37
2	Non-COPD	M	57	20.77	Former	0	0.29	4.68
3	Non-COPD	F	59	21.19	Current	0	0.56	2.37
4	Non-COPD	F	59	23.04	Former	0	0.08	0.96
5	Non-COPD	F	58	25.76	Current	0	0.69	1.81
6	Non-COPD	M	68	21.87	Current	0	0.33	0.31
7	Non-COPD	F	82	23.67	Former	0	0.11	3.89
8	Non-COPD	M	70	28.56	Former	0	0.61	1.26
9	Non-COPD	M	57	29.38	Current	0	8.07	13.11
10	Non-COPD	F	58	38.28	Current	0	21.72	20.13
11	Non-COPD	M	72	36.38	Current	0	3.33	8.20
12	Non-COPD	M	62	25.25	Current	0	3.81	5.89
13	Non-COPD	F	61	22.81	Current	0	0.70	1.07
14	COPD	M	64	31.13	Former	2	7.31	5.28
15	COPD	F	77	27.11	Former	1	0.75	3.63
16	COPD	F	62	33.71	Current	3	4.04	11.78
17	COPD	M	59	31.91	Former	4	8.07	10.11
18	COPD	M	65	21.05	Current	1	4.64	5.17
19	COPD	M	76	25.36	Former	2	2.45	2.93
20	COPD	F	70	29.48	Current	3	0.43	1.43

GOLD* = Global initiative for chronic obstructive lung disease

Table A-4. Patient information for the COPD study. *GOLD classification: the Global Initiative for Chronic Obstructive Lung Disease severity status for COPD. BMI, body mass index (kg m^{-2}).

Study ID	HF Group	Sex	NYHA classification	LVEF	Serum CRP ($\mu\text{g mL}^{-1}$)	Sweat CRP (ng mL^{-1})
1	HFpEF	M	II	55%-60%	4.90	3.21
2	HFpEF	M	I	55%-60%	0.80	5.53
3	HFpEF	M	II	60%-65%	1.10	4.42
4	HFpEF	M	II	53%	2.80	0.17
5	HFpEF	F	III	55%-60%	7.20	3.90
6	HFpEF	F	I	50%-55%	2.50	2.05
7	HFrEF	M	II	35%-40%	0.70	1.29
8	HFrEF	M	III	20%-25%	0.70	0.49
9	HFrEF	F	III	45%-50%	0.37	0.11
10	HFrEF	M	II	45%-50%	2.40	0.19
11	HFrEF	M	II	35%-40%	1.66	4.99

Supplementary A-5. Patient information for the heart failure study. *NYHA classification: the New York Heart Association (NYHA) functional classification of heart failure. LVEF: Left ventricular ejection fraction.

Table A-6. Patient information for the active infection study.

Study ID	Condition	Severity	Day	Serum CRP ($\mu\text{g mL}^{-1}$)	Sweat CRP (ng mL^{-1})
1	Cellulitis	Moderate	1	15.80	7.80
			2	0.80	4.33
2	Osteomyelitis	Severe	1	16.90	27.31
			2	10.10	12.11
3	Urinary tract infection	Moderate	1	47.50	26.01
			2	27.70	14.74

Table A-7. The currently reported microfluidic wearable sweat sensors.

Target	Autonomous sweat induction	Sweat sampling	Sweat & reagent routing	In-situ detection mechanism	Sensitivity	Ref.
Lactate, chloride, creatinine, glucose	No	Yes	Yes	Colorimetric	$\mu\text{M} - \text{mM}$	[1]
Chloride, zinc, sodium	No	Yes	Yes	Fluorometric	$\mu\text{M} - \text{mM}$	[2]
Uric acid, tyrosine	No	Yes	No	DPV	μM	[3]
Tyrosine, tryptophan, leucine, branched-chain amino acids	Yes	Yes	No	DPV, LSV	μM	[4]
Glucose, lactate	No	Yes	Yes	Amperometric	$\mu\text{M} - \text{mM}$	[5]
Cortisol	No	Yes	Yes	DPV	ng mL^{-1}	[6]
Chloride, glucose, levodopa	No	Yes	No	Amperometric	μM	[7]
Uric acid	No	Yes	Yes	Plasmonic	μM	[8]
Lactate	No	Yes	No	Amperometric	mM	[9]
Sodium, potassium	No	Yes	No	Potentiometric	mM	[10]
Sodium, potassium	No	Yes	No	ISFET	mM	[11]
CRP	Yes	Yes	Yes	SWV	ng mL^{-1}	Current work

Table A-8. Patient information for the post-COVID-19 infection study.

Study ID	Symptom	Sex	Days from recovery	Serum CRP ($\mu\text{g mL}^{-1}$)	Sweat CRP (ng mL^{-1})
1	Mild	M	14	0.04	0.20
2	Mild	M	15	0.03	0.25
3	Mild	M	9	0.24	0.40
4	Moderate	M	14	1.15	0.54
5	Moderate	F	15	3.30	2.55
6	Moderate	M	12	3.67	2.09

Note A-1 Simulated CRP-dAb levels on the working electrode over time

As sweat samples containing CRP molecules enter the microfluidic patch, the detector antibodies deposited in solid state are expected to dissolve and diffuse within the detection chamber along the concentration gradient. The collision between CRP molecules with antibodies will lead to the antigen-antibody binding events along the microfluidic channels before they eventually reach the detection chamber. The introduction of a serpentine microfluidic channel is also expected to facilitate the mixing and binding of the antigen-antibody complex.

Therefore, to visualize and estimate the time scale of the binding events at various locations of the microfluidic module, simulation of the CRP-antibody reversible binding reaction and the mass transport process of reactant and product were conducted through finite element analysis (FEA) using the commercial software COMSOL Multiphysics (see **Methods** and **Fig. 4d,e**).

Based on the results illustrated in **Fig. 4d**, the binding and transport of CRP with detection antibodies can be categorized into four stages. The heat maps represent the concentration of CRP-detection antibody complex formed. In the reconstitution stage (I), detection antibodies diffuse along the concentration gradient. Binding of CRP starts to occur within the center of the reagent reservoir as indicated by the red color. As more sweat containing CRP molecules enter the reagent reservoir, more antigen-antibody complexes are formed as indicated by the larger area of red-color species. The antigen-antibody complex travels along the flow direction to enter the detection chamber (circular chamber). After the serpentine mixing channels, antigen-antibody complex slowly distributes evenly across the detection chamber, allowing binding with capture antibodies immobilized at the bottom of the detection chamber to occur (II. Incubation).

After all the pre-deposited detection antibodies in the reagent reservoir are reconstituted, formed antigen-antibody complex with sweat CRP or flushed into the detection reservoir, the concentration of detection antibodies in the reagent reservoir is gradually depleted. The continuous flow of sweat into the microfluidic module will no longer lead to the formation of more antibody-antigen complexes as indicated by the blue color in the reagent reservoir in step III (Refreshment). Hence, fresh sweat stream deplete of antigen-antibody complexes continues to enter the detection chamber and flush the unbound antibody-antigen complexes in the chamber towards the outlet.

Eventually, all unbound antibody-antigen complexes and detection antibodies (which are labeled with electroactive molecules) will be refreshed out of the detection chamber as shown in step IV. At this stage, detection is performed, and the electrochemical signal obtained is specific and correlated to the antigen-antibody complexes bound on the working electrode surface since the concentration of the complex in the detection chamber converges to zero (indicated by the blue color).

Note A-2 Real-time CRP sensor calibration during on-body studies

We investigated the influence of pH, electrolyte and temperature and found that all factors influence the sensor readout of CRP based on **Supplementary Fig. 34**.

To account for the influences from binding environments, a multivariate model consisting of four independent variables: temperature, pH, electrolyte, CRP concentration ([CRP]) and a dependent variable: peak current expressed in potential (mV) was constructed based on the following equation:

$$\text{peak current} = A \times [\text{CRP}] \times \text{pH}^m \times [\text{electrolyte}]^n \times \text{temperature}^j.$$

The coefficients were solved using non-linear least square fitting in Matlab and found to be:

$$A = -0.5117; m = 0.6862; n = 0.1068; j = -0.6135.$$

The model demonstrates good accuracy in predicting signals measured by the sensors ($r^2 = 0.94$). During on-body operation, readings from the pH, temperature, electrolyte, and CRP sensors can thus be used to real-time back-calculate the actual concentration of CRP based on the fitted model.

Bibliography of Appendix A

1. Koh, A. *et al.* A soft, wearable microfluidic device for the capture, storage, and colorimetric sensing of sweat. *Science Translational Medicine* **8**, 366ra165 (2016).
2. Sekine, Y. *et al.* A fluorometric skin-interfaced microfluidic device and smartphone imaging module for *in situ* quantitative analysis of sweat chemistry. *Lab on a Chip* **18**, 2178–2186 (2018).
3. Yang, Y. *et al.* A laser-engraved wearable sensor for sensitive detection of uric acid and tyrosine in sweat. *Nature Biotechnology* **38**, 217–224 (2020).
4. Wang, M. *et al.* A wearable electrochemical biosensor for the monitoring of metabolites and nutrients. *Nature Biomedical Engineering*. **6**, 1225–1235 (2022).
5. Lin, H. *et al.* A programmable epidermal microfluidic valving system for wearable biofluid management and contextual biomarker analysis. *Nature Communications* **11**, 4405 (2020).
6. Lee, H.-B., Meeseepong, M., Trung, T. Q., Kim, B.-Y. & Lee, N.-E. A wearable lab-on-a-patch platform with stretchable nanostructured biosensor for non-invasive immunodetection of biomarker in sweat. *Biosensors and Bioelectronics: X* **156**, 112133 (2020).
7. Nyein, H. Y. Y. *et al.* A wearable patch for continuous analysis of thermoregulatory sweat at rest. *Nature Communications* **12**, 1823 (2021).
8. Mogera, U. *et al.* Wearable plasmonic paper-based microfluidics for continuous sweat analysis. *Science Advances* **8**, eabn1736 (2022).
9. Xuan, X., Pérez-Ràfols, C., Chen, C., Cuartero, M. & Crespo, G. A. Lactate biosensing for reliable on-body sweat analysis. *ACS Sensors* **6**, 2763–2771 (2021).
10. Pirovano, P. *et al.* A wearable sensor for the detection of sodium and potassium in human sweat during exercise. *Talanta* **219**, 121145 (2020).
11. Garcia-Cordero, E. *et al.* Three-dimensional integrated ultra-low-volume passive microfluidics with ion-sensitive field-effect transistors for multiparameter wearable sweat analyzers. *ACS Nano* **12**, 12646–12656 (2018).

Chapter 4

DISCUSSION AND OUTLOOK

Materials from this chapter appear in “Tu, J.; Torrente-Rodríguez, R. M.; Wang, M; Gao, W. The era of digital health: A review of portable and wearable affinity biosensors. *Advanced Functional Materials* 30, 1906713 (2019) doi:10.1002/adfm.201906713” and “Tu, J., & Gao, W. Ethical considerations of wearable technologies in human research. *Advanced Healthcare Materials* 10(17), 2100127 (2021) doi:10.1002/adhm.202100127.”

In the realm of wearable sweat sensors, we find ourselves at the intersection of technological innovation, healthcare transformation, and ethical contemplation. The journey so far has been marked by significant advancements in flexible electronics and biosensing technologies, offering the promise of practical applications in non-invasive fitness and health monitoring.

Early prototypes faced limitations in terms of their target range and sensing capabilities. They could mainly detect generic metabolites and surrogate markers, which were not directly linked to specific diseases. Consequently, these early examples were largely confined to the realm of fitness monitoring. Inaccuracies arose due to direct skin contact, motion artifacts, residual skin cell interference, complex manufacturing processes, inefficient sampling methods, and the complexities of sweat composition and its variable rate of secretion. Furthermore, there was limited evaluation of sweat biomarkers for clinical conditions.

To address these challenges, we embarked on a journey of innovation. We developed highly sensitive graphene sensors using a mass-producible laser-engraving technique, enabling precise and reliable detection of a broad spectrum of sweat constituents. These breakthroughs allowed us to explore scalable and universal surface modification strategies for bioreceptor immobilization, achieving specific and sensitive detection of a wide range of targets within sweat. Our focus on clinical utility led to the evaluation of sweat cortisol using mHealth sensors, enabling rapid point-of-care detection of trace-level targets like hormones.

Recognizing the need for hassle-free, in situ epidermal sensing, we pioneered the development of a microfluidic-enabled C-reactive protein sensor. By exploring the conjugation of electroactive labels to antibodies, we opened the door to direct electrochemical detection of non-electroactive targets, significantly expanding the potential applications of wearable sweat sensors. To mitigate the challenges posed by sweat composition interferences, we introduced multimodal sensors, including temperature, pH, and electrolyte sensors, for in situ calibration. Buffering salts were incorporated to minimize interference to binding kinetics caused by salt and pH variations. At the system level, we introduced a pair of iontophoresis electrodes to enable on-demand sweat sampling across daily activities, making our technology practical for sedentary patients.

In this concluding chapter, we reflect upon the culmination of these efforts and the broader implications for healthcare, as well as provide a glimpse into the exciting prospects that lie ahead. The broader field of biosensors and bioelectronics presents the universal challenge of improving sensor stability and selectivity while optimizing system integration to create compact, robust wearable devices.

The quest for non-invasive and uninterrupted monitoring of vital health parameters has spurred innovation and research in the field of epidermal sensors. Traditional methods of periodic measurements, often reliant on invasive procedures, are gradually giving way to a vision of real-time, continuous tracking that seamlessly integrates into our daily lives. However, continuous epidermal biosensing still remains a paramount challenge, requiring innovative solutions that bridge the gap between technological capability and practicality. In **Chapter 4.1**, we discuss the challenges, breakthroughs, and the boundless potential of this technology to enhance precision medicine and healthcare in unprecedented ways.

Moreover, as wearable sensor research emerges as a transformative technology, it brings with it an ethical dimension that requires our attention. The lack of an overarching ethical framework to guide the research community in this rapidly evolving field is a concern that cannot be overlooked. In the face of these unique challenges, **Chapter 4.2** discusses the ethical considerations that surround wearable bioelectronics to create a foundation for responsible innovation.

4.1 Continuous Epidermal Sensing

Despite the recent efforts in incorporating bioaffinity sensing on flexible platforms, the current generation of bioaffinity wearable sensors is still designed for one-time usage. The extraction of chronological information is particularly challenging in the case of bioaffinity sensors. Since the bioreceptors bind strongly to the analytes, real-time refreshment of the surface for fresh solution/new concentration of the analyte is hard to achieve without damaging the bioreceptors. There is a fair amount of literature documenting the regeneration of biosensor surfaces; the techniques involved in regeneration have been classified by Millner and colleagues into chemical regeneration, thermal regeneration, and electrochemical regeneration.¹The key to surface

regeneration lies in controlling the entropic and enthalpic interactions of the bioreceptor to the analyte. Stability concerns of the bioreceptors aside, chemical regeneration methods relying on surface charge alteration and overall ionic strength tuning² are at most only feasible for point-of-care sensing systems. The integration of strong acidic/basic solvent into a wearable sensing system, which is in direct/close contact with body cavities/epidermis, is neither safe nor practical. Thermal regeneration (more applicable to nucleotide-based bioaffinity sensor^{3,4} might be slightly feasible for wearable sensing on the basis that miniaturized heating and sensing elements can be well insulated.

Electrochemical regeneration, on the other hand, represents a convenient approach for wearable sensors, especially in the case of electrochemical wearable sensors. Earlier reports of this concept regenerate the electrode surface by applying a negative/positive potential to the sensor surface to achieve reductive/oxidative desorption.^{5,6} These methods, however, also remove the receptor from the sensor surface. The application of low-level electrical pulses has been demonstrated for controllable bioreceptor-analyte binding without damaging the receptor.^{7,8} Reversible ovalbumin and anti-ovalbumin binding was achieved under application and removal of a 1.3 V bias.⁹ The binding/unbinding of the aptamer-analyte complex with on-demand electrical pulses have also been demonstrated.^{10,11} Overall, the use of pre-programmed electrical stimuli for surface regeneration represents an elegant strategy in approaching continuous wearable bioaffinity sensors.

In addition to surface regeneration, an indispensable part of *in vivo* continuous sensing is the microfluidic design. Plaxco and Soh's team developed an *ex vivo* aptamer-based biosensor for real-time monitoring of drugs named MEDIC (microfluidic electrochemical detector for *in vivo* continuous monitoring).¹² The team created a continuous-flow diffusion filter (CDF) based on by forming a vertically stacked laminar stream of isotonic buffer between bloodstream and electrode. Smaller drug target, doxorubicin diffuses through the filter to bind with the receptor while larger protein interferents are 'filtered' by the CDF. The redox probe tagged-aptamer undergoes a reversible conformational in a continuous flowing buffer solution which endows MEDIC its time responsive capability. In addition, the team also developed a kinetic differential measurement (KDM) to improve the accuracy of real-time current measurements by minimizing drift and enhancing the signal-to-noise ratio.

A similar concept has also been developed for real-time measurement in direct awake, ambulatory animals.¹³ The ability to implant the device resolves the issue of time lag (the time required for blood to enter the device) and continuous blood drawing. Instead of generating laminar flow for CDF using a pump and buffer and waste reserves, the team applies a polysulfone membrane to prevent blood cells from approaching the sensor surface. The sensor reported a temporal resolution of 3s and demonstrated its universality detection of several drug targets using different aptamer probes. However, it should be noted that part of the temporal resolution comes from a trade-off of sensor sensitivity. The rapid desorption of targets from bioreceptor without the input of external stimuli/energy implies a large dissociation constant, which naturally yields a higher limit of detection. Indeed, the majority of the reported spontaneous binding/rebinding aptamer-based continuous sensing systems report μM sensitivity.

Overall, the design of continuous epidermal sensing technology is a dynamic and evolving field. As researchers continue to refine and innovate these technologies on both the micro- and macro we can anticipate even more sophisticated and accurate wearable sensors that will play a pivotal role in personalized healthcare, real-time monitoring, and improving our understanding of physiological processes.

4.2 Ethical Considerations of Wearable Technologies in Human Research

Driven by the promise of revolutionizing healthcare, the field of wearable technology has evolved rapidly into a broad, multidisciplinary topic in the past few years. Advances in microfabrication of silicon electronics and the development of soft electronic materials have enabled the seamless integration of sensing technologies with skin.¹⁴ A plethora of studies have expanded the capability to access and analyze biofluids for broader applications of continuous disease monitoring.^{15,16} The development of low-energy, self-powered systems makes continuous and autonomous operation for extended times possible.¹⁷

At the same time, commercial wearable technologies have also expanded from consumer health wearables towards wearable medical technology as fitness tracker giants like Apple Watch and Fitbit received FDA clearance for their ECG features. Accelerated by the shortage of medical

resources and the need for telemedicine tools amid the pandemic, FDA also granted Emergency Use Authorizations (EUA) to several remote or wearable patient monitoring devices such as VitalPatch and VSMS ECG Patch (G Medical) to aid the remote monitoring of patients.¹⁸

The forced adoption of telemedicine during the extended lockdown period and the recent breakthrough in wearable technology will fuel the shift of the healthcare paradigm to virtual and voluntary at-home monitoring and diagnosis of diseases in a foreseeable future. Still, only a handful of wearable technologies have been successfully commercialized and adopted for clinical decision-making currently.¹⁹ Solutions proposed at the bench side to address on-body operational challenges of wearable technologies will eventually need to be validated in humans and clinical studies before their translation into practice.

Similar to all emerging technologies, the lack of an overarching framework to guide wearable technology researchers in practice poses a barrier to the recruitment of subjects and the design of proper human research to collect meaningful data. Undoubtedly, wearable research involving human participants is guided by the three major principles of the Belmont Report, namely, respect of persons, beneficence, and justice. Researchers could also learn and draw parallels from past experiences on clinical trials involving new medical technologies when considering whether a study is ethical. For instance, Emanuel et al. proposed seven key evaluation requirements: (1) scientific/societal value of the research; (2) scientific validity; (3) fair subject selection; (4) risk-benefit analysis; (5) involvement of Institutional Review Board; (6) informed consent and (7) respect for participants²⁰. While these broad frameworks apply to human research in general; wearable technology poses unique challenges beyond past case studies of medical technologies. The vast amount of multimodal, real-time data collected during human research instigate a new set of concerns on data privacy and security. The multidisciplinary nature of the field also makes the identification of a particular set of principles or a use case for ethical guidance difficult. Ethical considerations for the development or application of wearable technology for generic fitness tracking may differ from those for medical-grade wearable technology. Although Institutional Review Boards (IRB) are the major stakeholder in protecting the rights and welfare of human subjects, IRB members may fall short of covering all ethical issues revolved around a new wearable technology due to the lack of experience and expertise.²¹ Wearable researchers, on the

other hand, are more familiar with a new technology and the potential risks involved. Therefore, the research community also shares the onus of identifying and addressing ethical concerns of human research and safeguarding the welfare of participants.

In this chapter, we briefly discuss ethical considerations and challenges specific to the wearable research community with close reference to the current technological advancements and their potential applications. In their course of experimental design and subject recruitment, wearable researchers could play a role in addressing various ethical considerations, including reliability and validity of a device, risk assessment, subject selection and exclusion, data privacy and security as well as informed consent (**Figure 4-1**). While this essay is by no means an exhaustive discussion of all potential ethical concerns, we hope to provide better insight for investigators in various domains and different stages of wearable technology development.



Figure 4-1. Ethical considerations and challenges of using new wearable technologies in human research.

4.2.1 Reliability and Validity

To resolve challenges faced by conventional wearable systems such as the mechanical mismatch between the skin and rigid electronics during motion, increasing efforts have been invested in the synthesis of novel stretchable materials and their integration in skin-interfaced wearable sensors wearable and mountable devices.^{14,22} Soft material innovation and smart structural engineering in the past decade have enabled the development of epidermal sensing systems for monitoring physical activities and physiological signals, such as pressure, skin temperature, pulse oximetry, as well as chemical and biochemical analytes in biofluids such as sweat, saliva, and tear.²³ In the meantime, the dynamic working environment that a wearable physical or chemical sensor faces during on-body operation still introduces additional complexity and uncertainty into the real-time collection of accurate physiological information. For example, skin temperature sensors that rely on electrical behavior changes of the materials against temperature can easily be influenced by the mechanical strain.²⁴ Skin temperature variation inadvertently affects the performance of potentiometric sensors and enzymatic sensors.^{25,26} In addition to motion artifacts, photoplethysmography (PPG) based wearable sensors may have reduced accuracy in subjects with darker tones.^{27,28} Although various soft epidermal systems under research have demonstrated the intimate and unobtrusive integration of such system on the skin,²⁹ the technological limitations of visible-light based PPG are seldom discussed and assessed in both commercially available rigid substrate wearable devices and soft electronics research. Many factors present on the skin may affect the absorption of light differently; darker skin tones, tattoos, the presence of arm hair, sweat, body mass could all influence PPG accuracy and compromise PPG-related health outcome analysis. Inaccurate data collected during human research due to insufficient device validation is ineffective at best. These data could also potentially exert unintended harm if they are incorporated in closed-loop body computing systems and result in incorrect health conclusions or trigger unintended intervention to the physiological environment.³⁰ Therefore, the onus is on researchers engaged in developing novel sensing strategies on-the-skin to account for the dynamic changes in environmental and operational factors during human research and validate the veracity of a newly developed sensor against potential influences. One common strategy adopted by several research groups is the cross-validation of sensor response with laboratory gold standard (**Figure 4-2a** and

b).³¹⁻³⁴ Others cross-reference the data collected on-body with those collected ex vivo to identify any potential interference caused by the on-body operation.³⁵ Recently, various in-situ calibration mechanisms have also been introduced to account for the dynamic changes and improve sensor accuracy.^{26,36,37} In conjunction with ex-situ and in-vitro validation of the sensor, many investigators of wearable chemical sensors may also opt to evaluate the relationship/correlation between serum and biomarkers present in alternative biofluid source, considering the potential influences from biofluid secretion rate and mechanism.^{38,39} It is important to recognize that even if the results may not lead forward the translation of a technology (i.e., in the case of a weak or insignificant correlation), these studies still contain important information for the entire research community to evaluate the clinical significance of certain biomarkers and steer the research focus in a different direction. The appropriate and responsible reporting of validation data, as well as disclosure of uncertainty, are not only essential to ensure that results from human research are of scientific and societal significance but also the safety of participants.

In addition to the common reliability and accuracy issues faced by new sensing technologies, a unique challenge to wearable sensing devices is participants' constant access to the sensing data. False positives as a result of inaccurate sensor reading may cause unnecessary anxiety, and the nature of wearable devices with frequent measurements and accessible data may exacerbate this emotional stress and confusion. For wearable sensing devices that target for day-to-day usage/evaluation in participants, efforts should also be devoted towards identifying the right way and appropriate frequency of presenting accurate data to the participants.

4.2.2. Risk Assessment

Although 'non-invasiveness' has been one of the key driving forces for the development of wearable devices for biomarkers monitoring; researchers should not overlook any physical or chemical risks associated with the operation of wearable technology in human research. Common risks associated with the on-body evaluation of wearable technologies include skin irritation, electrical shock, radiation exposure, chemical exposure and infection.

Often, epidermal devices built on conventional polymeric substrates, such as polydimethylsiloxane (PDMS), polyethylene terephthalate (PET), and polyimide (PI), are not gas permeable.^{40,41} In some

use case scenario this property is leveraged to prevent evaporation of sweat and facilitate the retention of volatile organic components within the skin device interface,^{42,43} on the other hand, this may also lead to skin irritation and introduce discomfort when such devices are worn for a long time. Sometimes, other choices of breathable, inflammation-free design of epidermal electronics may be available for longer-term human study (**Figure 2c**).^{40,44} Researchers should take skin irritation and the length of study into consideration when designing human studies to minimize the risk and discomfort of participants.

Mountable devices like smart mouth guard,⁴⁵ earpieces³⁷ or glasses⁴⁶ warrant a closer examination of potential hazards due to chemical exposure because they are placed close to body cavities with weaker barriers of defense even though they are still considered “non-invasive” by many. In the case of a mouth guard, not only is the sensor/electrode exposed to the oral cavity but also other electronic components such as the printed circuit board (PCB).⁴⁷ The biocompatibility of individual components should be considered because even minute details like the choice of PCB solder may lead to accidental ingestion of toxic heavy metal (e.g., lead) during human studies. Additional precautions should be taken to encapsulate potential harmful components or replacing components with more biocompatible alternatives before researchers embark on device evaluation in human studies.

Soft electronics that are designed for direct contact with the ocular cavity^{48,49} and open wounds^{50,51} are typically associated with more risks when evaluated in vivo. In addition to biocompatibility and device design ergonomics concerns, an important factor to consider in order to meet the principle of nonmaleficence is the sterilization of devices to minimize risks of infection.^{52,53} Sensible steps to take before human research include the in vitro cytotoxicity screening of materials and the testing in preclinical animal models.⁵⁴⁻⁵⁶ In these two cases, ethical considerations relevant to animal research and the choice of animal models with modest translational distance (characterized by the number and size of inferential leaps from animals to humans⁵⁷) are important.

Wearable transdermal sensors in the form of microneedles are minimally invasive because of the small dimensions of the needles. Although reports show that recovery of skin barrier function can

be as fast as a few hours after micropore creation,⁵⁸ the application of wearable transdermal device introduce additional risks of infections as unclosed microchannels may promote microcirculation of bacteria.⁵⁹ Standard operation protocols that ensure implementation of good clinical practice prior to the application of microneedle patches are essential in minimizing influx of exogenous microbiomes from surroundings. Confounding factors such as random movements, natural variations in skin texture, manual application pressure may introduce additional compression or sheer stress that could potentially result in the failure and fracture of hollow microneedles. Moreover, microneedle materials or residual chemical from microneedle processing methods could introduce additional risks of skin irritation. Various mechanical and biophysical characterization methods could be conducted in vitro and in vivo to evaluate potential hazards and assess the safety (skin irritation) of new devices.^{60,61}

In addition to performing sensing and monitoring tasks, many wearable technologies developed in the lab also involve certain intervention capabilities where built-in actuators are triggered to deliver electrical/thermal stimulation or, in some cases, active drug components. GlucoWatch's reverse iontophoresis (RI) might be the earliest demonstration of such types of intervention to facilitate the access and concentration of biofluids or biomarkers.⁶² RI applies a mild current between two electrodes to induce ion migration across the skin and extracts interstitial fluids due to electro-osmotic flow. One reason for the later retraction of this device from the market is the reported skin irritations due to the application of current.⁶³ Similarly, skin irritation is also associated with the long-term operation of epidermal iontophoretic devices that rely on the application of mild current to deliver sweat-stimulating drugs to trigger the local secretion of sweat under sedentary conditions.^{15,64} Risks of skin irritation due to electrical shock and chemical build-up can be controlled and minimized by reducing current density, the time of application, appropriate buffering recipe and switching of cathode/anode to maintain local pH.⁶⁵ Other examples of intervention technologies are most commonly found in next-generation closed-loop systems where continuous monitoring of biomarkers is coupled with actuators that can be triggered when the level of a biomarker fluctuates beyond desirable levels.^{30,54} In addition to performing and disclosing electrical safety risk assessment, researchers should also consider biochemical risks such as allergic reaction when an intervention technology is designed to deliver active drug components

to subjects. Extra caution should be taken to address potential drug interaction when the subjects are taking additional medications.

While all wearable devices with wireless communication capabilities expose subjects to radiofrequency radiation, devices employing high-power communication technologies such as WiFi to transfer large datasets are more susceptible to radiation risks. Although high power devices like smart phones are generally regulated by specific absorption rate (SAR) testing and there is currently no clear evidence on the risks of low-level radiation,⁶⁶ wearable devices are clearly placed in closer proximity to the human body for longer periods of time. Risks associated with chronic exposure to low-intensity radiation are currently unknown. In addition, researchers should also be cautious of the cumulative effects of low-intensity radiation by operating multiple high-power wearable/portable devices in parallel.⁶⁷

4.2.3. Fair subject selection and exclusion

Human research studies in this emerging field mostly fall into the category of first-in-human (FIH) or early-stage human trials. Experiments are designed based on information from limited literature sources or animal studies that predict a participant's safety can be adequately protected with certain assumptions. Along with the objectives of scientific validity and societal value, experimental designs of human trials should clearly identify risks of harm to the subjects and outline all possible precautionary or intervention steps during the study to minimize risks and prevent harm. Selecting subjects who can make well-informed choices about research participation and from whom scientifically relevant data with minimal risks is a critical step.

Apt and fair subject selection may pose considerable challenges for FIH trials. For wearable medical technologies targeted at various vulnerable populations (patients with specific disease conditions), substantially more risks are involved as compared to the participation of healthy subjects. The evaluation of wearable sweat sensors typically requires subjects to perform mid- to high-intensity physical exercise. Human studies dealing with the non-invasive monitoring and management of chronic diseases such as metabolic syndrome or diabetes may require the recruitment of subjects with pre-existing medical conditions. Subjects who are physically inactive may find typical cycle ergometer exercise protocol designed for sweat collection (e.g., timed trial

with constant workload or graded workload) more physically demanding. Potential risks and exercise-induced emergencies (e.g., bronchoconstriction, anaphylaxis, heat-illness) should be identified with appropriate standard operating procedures outlined prior to the recruitment of subjects to safeguard vulnerable populations.

Human studies may also aim to intentionally trigger a transient physiological or psychological abnormality in subjects (e.g., stress⁶⁸ and fatigue⁶⁹ experiments). Under the oversight of IRB, researchers are responsible for weighing the potential scientific value against the susceptibility to risk for certain groups of individuals (e.g., pregnant women, students) and determining the appropriate exclusion criteria of a study. As the ultimate goal of most wearable technologies is to monitor or diagnose a user's health conditions, researchers may occasionally encounter incidental findings (e.g., abnormalities in the data collected from a participant) in the course of human research. A detailed framework for addressing and managing incidental findings during human research can be found elsewhere.⁷⁰

Investigators should also make concerted efforts in recruiting individuals of various backgrounds in order to conduct scientifically and ethically sound research. The main goal of early-stage human research in wearable technology is to validate and translate a novel technological breakthrough to a viable prototype that could potentially benefit the largest population. Therefore, potential risks/benefits and device validity should be evaluated across different groups to minimize subject selection biases or inadvertent exclusion-by-design. Wearable exoskeletons that are designed to restore or enhance human strength and agility hold great promise in rehabilitation. However, the device size and weight of wearable exoskeletons impose certain weight, height restrictions on the user/subject.⁷¹ Commercial exoskeleton providers tend to impose rigid inclusion criteria from a cost perspective by investing on one-size-fits-all prototypes. As a result, children and individuals who are obese (which could be common for disabled individuals with sedentary lifestyles) may be denied access to such technologies due to exclusion by design. Women from certain ethnic groups with lower average height also tend to be "underweight" based on the user selection criteria of most commercial exoskeletons. Wearable exoskeleton research could potentially tackle this discrimination on marginalized communities by understanding and reflecting on the exclusion criteria and improve the inclusivity of a device from the design stage. Researchers share the

responsibility to identify potential biases and dismantle any disparities caused by inappropriate device or human study design from the start. Incomplete metrics obtained in validation studies that lack diversity may also cause unintended consequences by reinforcing existing disparities in healthcare.⁷²

4.2.4. Data Privacy and Security

The integration of a plethora of sensors on soft epidermal systems has enabled the passive collection of temporal information of a wide range of behavioral and biometric data. Real-time, continuous transmission of the information collected to other devices or cloud storage for post-processing can be achieved with various wireless communication technologies such as Near Field Communication (NFC), Bluetooth, Zigbee, and Wi-Fi.³⁰ Information collected and transmitted through current wearable technologies ranges from a simple heartbeat to the geographical location of a user and his medical conditions. While data sharing presents its unique advantage to personalized and adaptive health interventions, the vast amount of private identifiable information associated with human research raises serious concern over the privacy and data confidentiality of participants. A recent survey on digital consumer health revealed that the use of consumer health wearable devices has decreased from 33% in 2018 to just 18% in 2019.⁷³ Participants of human studies involving pervasive sensing technologies also cited data privacy and confidentiality as a major concern.⁷⁴ Therefore, investigators need to think ahead of research and incorporate ethical and regulatory considerations of data privacy and security early in the research design.

At times, data anonymization via distortion or removal of identifying features is introduced in research protocol to protect personal data. However, the effectiveness of such approaches against personal identity theft is still questionable.⁷⁵ Depending on the nature of the human study (population-level or personalized medicine), requirements on the extent of personal information gathered may differ. Controversies over COVID-19 tracing with mobile health and wearable technologies manifest the risks and potential conflicts associated with personal data in large scale data-rich human research. The decentralized contact tracing app promoted by Google and Apple allows anonymized pairing between infected people and their close contacts on their phones; on the other hand, the centralized tracing method traces contacts with a health authority-owned

database by collecting personal information with mobile phone apps, wearable dongle or other surveillance methods. Although advocates of centralized tracing cited epidemiological benefits as health authorities can monitor the disease's spread, concerns over intensive surveillance and intrusion of privacy stalled the adoption of centralized tracing in many countries.⁷⁶ Some biometric information collected with wearable technology may fall in the grey zone when it comes to regulatory compliance of data protection laws like General Data Protection Regulation (GDPR) and Health Insurance Portability and Accountability Act (HIPAA). While the ethical, legal, and social concerns in data-driven human studies may require collaborative efforts from IRB-related stakeholders, security experts and legal and regulatory expertise to outline case-specific data management and storage protocols,⁷⁴ on an individual research level, investigators can also address this trust deficit crisis by being forthcoming with how data is collected and used.

4.2.5. Informed consent

Informed consent is an ethical, regulatory, and legal requirement in human research that allows researchers to communicate the potential benefits and risks of the study to the participants. However, an informed consent document can be lengthy and contain technical jargons that are hard for potential research participants to comprehend. To practice respect for persons and to minimize information asymmetry, the information about the human study must be conveyed in a simple language to ensure adequate understanding. Additional methods such as video and in-person demonstration may facilitate comprehension during the consent process.⁶⁷ Adaptions of the informed consent may be necessary to account for varying degrees of educational literacy, cognitive ability, and clinical status in potential participants.⁷⁷ In an informed consent document, potential risks and the purpose of the study should be clearly communicated for participants to make informed decision. Another important point to take note of and clarify in the informed consent for the wearable research community is the issue of data ownership and secondary use of data. In addition to the sensor and wireless communication technology development, a sizeable number of studies focus on software development and data analysis through machine learning.^{78,79} Research groups with limited hardware development expertise may opt for commercially available consumer health or medical health wearable devices to collect large scale human data.⁸⁰ In such cases, end-user licensing agreement of the commercial device may complicate the issue of data

ownership and usage. For example, Fitbit users may be unintentionally sharing their information with third parties when they sign up for an account.⁸¹ Researchers should inform participants of potential secondary usage of data as stated in the privacy policy documents of commercial devices.

While both medical grade and consumer health grade wearable technologies are available on the market, the fine distinctions between these two device categories tend to cause confusion among the general public. A user's misconception over the information collected by a wellness device may also be exacerbated by commercial advertisements' choice of wording and the implied benefits. Therefore, an informed consent should explicitly state if the purpose of the device under evaluation is to diagnose or treat a medical condition (which constitute as a medical device) or to collect information to avoid participants' confusion and over trust of a device and its data.

4.2.6. Summary and perspective

To date, much effort has been invested in the development and prototyping of soft electronics and robust sensing technologies at the bench side. Moving forward, current wearable technologies will need to demonstrate their validity and utility in clinical or point-of-care settings with larger scale human data from longitudinal and cohort studies. As current epidermal sensing technologies mature, they are expected to integrate into more complex closed-loop systems that allow autonomous intervention for therapeutic purposes to achieve the ultimate goal of personalized disease management. Although there have been commercial products that are capable of closing the loop in disease management such as Medtronic's sensor-augmented insulin pump therapy for diabetes management (**Figure 2e**); these systems are based on rigid electronics with minimally invasive monitoring techniques. Future advances in biomaterials and flexible electronics will drive the evolution of such closed-loop systems into smaller, more conformal, hassle-free prototypes that can find applications in a broader audience. For example, an integrated drug delivery system consists of graphene-based multipixel biosensors for noninvasive sweat glucose monitoring and a thermoresponsive microneedle patch (triggered by elevated glucose level) for insulin therapy was proposed.^[41] Still, wearable closed-loop sensor-augmented drug delivery system is in its infancy. Such prototypes have yet to be validated rigorously *in vivo*. In addition to a multitude of technological bottlenecks in reliable sensor reading, energy harvesting, communication, and

closed-loop algorithm, challenges such as therapy effectiveness, reliability and safety will need to be answered with large-scale and in-depth animal and/or human studies.

Despite the exponential growth of the field in the past decade, we are only at the beginning of harnessing wearable technology for performance enhancement and health management. As the field progresses, more innovative solutions to current technical challenges may become available; at the same time, these technologies may also bring about unforeseen ethical concerns during human research. We believe the active engagement of the research community in the ethical discussions and protection of human welfare is instrumental in facilitating successful early-stage human trials. Clear and close communication with research oversight bodies ensures that knowledge held by the researchers can be formalized and transferred to independent regulatory oversights and close the gap between current regulatory guidelines and the rapidly evolving research landscape. The medical community's acceptance of these non-invasive technologies and their subsequent translation to a broader audience will require the concerted efforts of the research community to conduct scientifically and ethically sound in-human validation and extensive investigation on the clinical relevance of data collected with wearable technologies.

4.3 Conclusion and Outlook

In the exploration of wearable biosensing, the chapter has traversed a landscape of both challenges and opportunities that hold the potential to reshape the future of healthcare and personalized disease management. It has highlighted the inherent synergy between continuous real-time monitoring wearable platforms and the world of bioaffinity sensing. It's evident that the two fields, when united, can usher in a new era of comprehensive health insights that adapt seamlessly to daily lives.

Two major challenges, label-free and wash-free assay design for system integration, and recognition site regeneration for continuous monitoring, stand as pivotal technological bottlenecks that require innovative solutions. Achieving real-time resolution in wearable bioaffinity sensors, capturing the dynamic interplay of biomarkers, and aligning it with physiological refresh rates, all pose essential considerations. In addition to the reflection of real-time biochemical information, the most attractive attribute of wearable sensors is the ability to capture and record the

chronological fluctuations of biomarkers. The timescale required to capture meaningful information differs for each biomarker. For instance, monitoring of acute stress reactivity requires a temporal resolution of 10 minutes for stress hormones quantification,⁸² whereas to establish the cortisol circadian pattern of a subject for mental health management, the sampling interval can be as wide as a few hours.⁸³ The periodic fluctuation of sex steroid hormones (i.e., progesterone, estradiol, luteinizing hormone) is as long as one month.⁸⁴ On the other hand, there is also a lower limit on how short the sampling and sensing interval need to be for each type of wearable platforms. For instance, a reported microfluidic model estimated the refresh time of sweat to be 2 minutes.⁸⁵ A sampling frequency beyond the physiological limit of biofluid generation acquires redundant information at the expense of excess power consumption. An order of magnitude estimation of the practical sampling frequency required is crucial to the design and practical implementation of wearable bioaffinity sensors towards disease management.

In addition to the problems specific to wearable bioaffinity sensors, several characteristics general to all analytical devices developed should also be met after the proof-of-concept stage including stability, reproducibility, and accuracy. In this review, we have drawn concepts from several fields in an attempt to discuss the key technological bottlenecks in the future of wearable platforms for disease monitoring. A list of characteristics essential to an ideal wearable bioaffinity sensor is found in **Table 4-1**.

Looking forward, there are several exciting opportunities ahead to address the technical challenges. The issue of stability of bioreceptor may potentially be ameliorated with the use of more stable bioreagents such as nanobodies⁸⁶⁻⁸⁸ and selective ligands.⁸⁹ Artificial receptors such as molecularly imprinted polymers and aptamers have also shown promising selectivity and sensitivity in biomarker recognition. Label-free strategies proposed for portable biosensors can also be readily adapted for wearable strategies. Similarly, ideas from self-powered/pump-free and paper microfluidics may be borrowed for wash-free on-body wearable sensing.

In this fusion of diverse technologies and interdisciplinary collaboration, the chapter envisions the emergence of a new era in healthcare, where the seamless integration of wearable bioaffinity sensors into daily lives not only enhances precision medicine but also empowers individuals with

a profound understanding of their well-being. As the field faces these challenges and embraces the opportunities that lie ahead, it draws ever closer to a future where health management is not just a reactive process but a proactive journey toward holistic well-being.

Key characteristics	Description
Conformability	Stretchability and mechanical properties of the sensor platform should be compliant with human epidermis or the surface of the organs in contact to minimize measurement errors.
Response time	Should produce a ‘real-time’ response, or at least a short response time to provide prompt information.
Continuity	The sensor should be able to register multiple measurements in a given time frame to provide a dynamic profile.
Reproducibility	Should provide same response when the same concentrations are measured at various time.
Stability	Should be stable with a reasonable shelf-life in various environmental parameters and conditions during execution.
Accuracy	The results should close to the agreement between a test result and the true value, or if not known, the accepted reference value can be considered.
Selectivity	Should easily discriminate between the target signal and other interfering molecules in the sample matrix and relate to the number of false positive and false negative results that are found with the validated method.
Sensitivity	The sensitivity and detection range should be better or broader than the physiologically relevant range of biomarkers.

Table 4-1. Key Characteristics of an ideal wearable bioaffinity sensor.

Bibliography of Chapter 4

1. Goode, J. A., Rushworth, J. V. H. & Millner, P. A. Biosensor regeneration: A review of common techniques and Outcomes. *Langmuir* **31**, 6267–6276 (2015).

2. Sahin, E., Grillo, A. O., Perkins, M. D. & Roberts, C. J. Comparative effects of pH and ionic strength on protein-protein interactions, unfolding, and aggregation for IgG1 antibodies. *Journal of Pharmaceutical Sciences* **99**, 4830–4848 (2010).
3. Delport, F. *et al.* Real-time monitoring of DNA hybridization and melting processes using a fiber optic sensor. *Nanotechnology* **23**, 065503 (2012).
4. Hilton, J. P., Nguyen, T. H., Pei, R., Stojanovic, M. & Lin, Q. A microfluidic affinity sensor for the detection of cocaine. *Sensors and Actuators A: Physical* **166**, 241–246 (2011).
5. Choi, S., Goryll, M., Sin, L. Y. M., Wong, P. K. & Chae, J. Microfluidic-based biosensors toward point-of-care detection of nucleic acids and proteins. *Microfluidics and Nanofluidics* **10**, 231–247 (2011).
6. Bhalla, V., Carrara, S., Stagni, C. & Samori, B. Chip cleaning and regeneration for electrochemical sensor arrays. *Thin Solid Films* **518**, 3360–3366 (2010).
7. Gilles, P. N., Wu, D. J., Foster, C. B., Dillon, P. J. & Chanock, S. J. Single nucleotide polymorphic discrimination by an electronic dot blot assay on semiconductor microchips. *Nat Biotechnol* **17**, 365–370 (1999).
8. Westin, L. *et al.* Anchored multiplex amplification on a microelectronic chip array. *Nat Biotechnol* **18**, 199–204 (2000).
9. Liron, Z., Tender, L. M., Golden, J. P. & Ligler, F. S. Voltage-induced inhibition of antigen-antibody binding at conducting optical waveguides. *Biosensors and Bioelectronics* **17**, 489–494 (2002).
10. Ma, X., Gosai, A., Balasubramanian, G. & Shrotriya, P. Aptamer based electrostatic-stimuli responsive surfaces for on-demand binding/unbinding of a specific ligand. *Journal of Materials Chemistry B* **5**, 3675–3685 (2017).
11. Gosai, A., Ma, X., Balasubramanian, G. & Shrotriya, P. Electrical stimulus-controlled binding/unbinding of human thrombin-aptamer complex. *Scientific Reports* **6**, 37449 (2016).
12. Ferguson, B. S. *et al.* Real-time, aptamer-based tracking of circulating therapeutic agents in living animals. *Science Translational Medicine* **5**, 213ra165 (2013).
13. Arroyo-Currás, N. *et al.* Real-time measurement of small molecules directly in awake, ambulatory animals. *Proc Natl Acad Sci U S A* **114**, 645–650 (2017).

14. Yang, J. C. *et al.* Electronic skin: Recent progress and future prospects for skin-attachable devices for health monitoring, robotics, and prosthetics. *Advanced Materials* **31**, 1904765 (2019).
15. Heikenfeld, J. *et al.* Accessing analytes in biofluids for peripheral biochemical monitoring. *Nature Biotechnology* **37**, 407–419 (2019).
16. Tu, J., Torrente-Rodríguez, R. M., Wang, M. & Gao, W. The era of digital health: A review of portable and wearable affinity biosensors. *Advanced Functional Materials* **30**, 1906713 (2020).
17. Yu, Y., Nyein, H. Y. Y., Gao, W. & Javey, A. Flexible electrochemical bioelectronics: The rise of in situ bioanalysis. *Advanced Materials* **32**, 1902083 (2020).
18. Health, C. for D. and R. Remote or Wearable patient monitoring devices EUAs. *The United States Food and Drug Administration* (2020).
19. Wearable technology in healthcare. *Nature Biotechnology* **37**, 376–376 (2019).
20. Emanuel, E. J., Wendler, D. & Grady, C. What makes clinical research ethical? *The Journal of the American Medical Association* **283**, 2701–2711 (2000).
21. Torous, J. & Nebeker, C. Navigating ethics in the digital age: Introducing connected and open research ethics (CORE), a Tool for Researchers and Institutional Review Boards. *J Med Internet Res* **19**, (2017).
22. Someya, T., Bao, Z. & Malliaras, G. G. The rise of plastic bioelectronics. *Nature* **540**, 379–385 (2016).
23. Kim, J., Campbell, A. S., de Ávila, B. E.-F. & Wang, J. Wearable biosensors for healthcare monitoring. *Nature Biotechnology* **37**, 389–406 (2019).
24. Xu, C., Yang, Y. & Gao, W. Skin-interfaced sensors in digital medicine: from materials to applications. *Matter* **2**, 1414–1445 (2020).
25. Bandodkar, A. J. *et al.* Epidermal tattoo potentiometric sodium sensors with wireless signal transduction for continuous non-invasive sweat monitoring. *Biosensors and Bioelectronics* **54**, 603–609 (2014).

26. Hong, Y. J. *et al.* Multifunctional wearable system that integrates sweat-based sensing and vital-sign monitoring to estimate pre-/post-exercise glucose levels. *Advanced Functional Materials* **28**, 1805754 (2018).
27. Shcherbina, A. *et al.* Accuracy in wrist-worn, sensor-based measurements of heart rate and energy expenditure in a diverse cohort. *Journal of Personalized Medicine* **7**, 3 (2017).
28. Fallow, B. A., Tarumi, T. & Tanaka, H. Influence of skin type and wavelength on light wave reflectance. *J Clin Monit Comput* **27**, 313–317 (2013).
29. Yokota, T. *et al.* Ultraflexible organic photonic skin. *Science Advances* **2**, e1501856 (2016).
30. Lin, Y., Bariya, M. & Javey, A. Wearable biosensors for body computing. *Advanced Functional Materials* **n/a**, 2008087.
31. Koh, A. *et al.* A soft, wearable microfluidic device for the capture, storage, and colorimetric sensing of sweat. *Science Translational Medicine* **8**, 366ra165-366ra165 (2016).
32. Parlak, O., Keene, S. T., Marais, A., Curto, V. F. & Salleo, A. Molecularly selective nanoporous membrane-based wearable organic electrochemical device for noninvasive cortisol sensing. *Science Advances* **4**, eaar2904 (2018).
33. Bندوقkar, A. J. *et al.* Battery-free, skin-interfaced microfluidic/electronic systems for simultaneous electrochemical, colorimetric, and volumetric analysis of sweat. *Science Advances* **5**, eaav3294 (2019).
34. Tian, L. *et al.* Large-area MRI-compatible epidermal electronic interfaces for prosthetic control and cognitive monitoring. *Nature Biomedical Engineering* **3**, 194–205 (2019).
35. Gao, W. *et al.* Fully integrated wearable sensor arrays for multiplexed in situ perspiration analysis. *Nature* **529**, 509–514 (2016).
36. Gao, L. *et al.* Epidermal photonic devices for quantitative imaging of temperature and thermal transport characteristics of the skin. *Nature Communications* **5**, 4938 (2014).
37. Ota, H. *et al.* 3D printed “earable” smart devices for real-time detection of core body temperature. *ACS Sensors* **2**, 990–997 (2017).
38. Choi, D.-H., Kitchen, G. B., Stewart, K. J. & Searson, P. C. The dynamic response of sweat chloride to changes in exercise load measured by a wearable sweat sensor. *Scientific Reports* **10**, 7699 (2020).

39. Klous, L., de Ruiter, C. J., Scherrer, S., Gerrett, N. & Daanen, H. A. M. The (in)dependency of blood and sweat sodium, chloride, potassium, ammonia, lactate and glucose concentrations during submaximal exercise. *European Journal of Applied Physiology* (2020) doi:10.1007/s00421-020-04562-8.
40. Fan, Y. J. *et al.* Highly robust, transparent, and breathable epidermal electrode. *ACS Nano* **12**, 9326–9332 (2018).
41. Zhou, W. *et al.* Gas-permeable, ultrathin, stretchable epidermal electronics with porous electrodes. *ACS Nano* **14**, 5798–5805 (2020).
42. Reeder, J. T. *et al.* Waterproof, electronics-enabled, epidermal microfluidic devices for sweat collection, biomarker analysis, and thermography in aquatic settings. *Science Advances* **5**, eaau6356 (2019).
43. Yang, Y. *et al.* A laser-engraved wearable sensor for sensitive detection of uric acid and tyrosine in sweat. *Nature Biotechnology* **38**, 217–224 (2020).
44. Miyamoto, A. *et al.* Inflammation-free, gas-permeable, lightweight, stretchable on-skin electronics with nanomeshes. *Nature Nanotech* **12**, 907–913 (2017).
45. Kim, J. *et al.* Non-invasive mouthguard biosensor for continuous salivary monitoring of metabolites. *Analyst* **139**, 1632–1636 (2014).
46. Sempionatto, J. R. *et al.* Eyeglasses based wireless electrolyte and metabolite sensor platform. *Lab on a Chip* **17**, 1834–1842 (2017).
47. Kim, J. *et al.* Wearable salivary uric acid mouthguard biosensor with integrated wireless electronics. *Biosensors and Bioelectronics* **74**, 1061–1068 (2015).
48. Introducing our smart contact lens project. *Google* <https://blog.google/alphabet/introducing-our-smart-contact-lens/> (2014).
49. Tseng, R. C., Chen, C.-C., Hsu, S.-M. & Chuang, H.-S. Contact-lens biosensors. *Sensors* **18**, 2651 (2018).
50. Guinovart, T., Valdés-Ramírez, G., Windmiller, J. R., Andrade, F. J. & Wang, J. Bandage-based wearable potentiometric sensor for monitoring wound pH. *Electroanalysis* **26**, 1345–1353 (2014).

51. Brown, M. S., Ashley, B. & Koh, A. Wearable technology for chronic wound monitoring: current dressings, advancements, and future prospects. *Front. Bioeng. Biotechnol.* **6**, (2018).
52. McCrudden, M. T. C. *et al.* Considerations in the sterile manufacture of polymeric microneedle arrays. *Drug Delivery and Translational Research* **5**, 3–14 (2015).
53. Ochoa, M. *et al.* Integrated sensing and delivery of oxygen for next-generation smart wound dressings. *Microsystems & Nanoengineering* **6**, 1–16 (2020).
54. Lee, H. *et al.* A graphene-based electrochemical device with thermoresponsive microneedles for diabetes monitoring and therapy. *Nature Nanotechnology* **11**, 566–572 (2016).
55. Lee, H. *et al.* Wearable/disposable sweat-based glucose monitoring device with multistage transdermal drug delivery module. *Science Advances* **3**, e1601314 (2017).
56. Keum, D. H. *et al.* Wireless smart contact lens for diabetic diagnosis and therapy. *Science Advances* **6**, eaba3252 (2020).
57. Kimmelman, J. *Gene Transfer and the Ethics of First-in-Human Research: Lost in Translation.* (Cambridge University Press, 2010).
58. Kalluri, H., Kolli, C. S. & Banga, A. K. Characterization of microchannels created by metal microneedles: Formation and closure. *AAPS J* **13**, 473–481 (2011).
59. McConville, A., Hegarty, C. & Davis, J. Mini-Review: Assessing the potential impact of microneedle technologies on home healthcare applications. *Medicines (Basel)* **5**, (2018).
60. Park, J.-H., Allen, M. G. & Prausnitz, M. R. Biodegradable polymer microneedles: Fabrication, mechanics and transdermal drug delivery. *Journal of Controlled Release* **104**, 51–66 (2005).
61. Bal, S. M., Caussin, J., Pavel, S. & Bouwstra, J. A. In vivo assessment of safety of microneedle arrays in human skin. *European Journal of Pharmaceutical Sciences* **35**, 193–202 (2008).
62. Potts, R. O., Tamada, J. A. & Tierney, M. J. Glucose monitoring by reverse iontophoresis. *Diabetes/Metabolism Research and Reviews* **18**, S49–S53 (2002).
63. Kim, J., Campbell, A. S. & Wang, J. Wearable non-invasive epidermal glucose sensors: A review. *Talanta* **177**, 163–170 (2018).

64. Emaminejad, S. *et al.* Autonomous sweat extraction and analysis applied to cystic fibrosis and glucose monitoring using a fully integrated wearable platform. *Proceedings of the National Academy of Sciences of the United States of America* **114**, 4625–4630 (2017).
65. Roustit, M., Blaise, S. & Cracowski, J.-L. Trials and tribulations of skin iontophoresis in therapeutics. *British Journal of Clinical Pharmacology* **77**, 63–71 (2014).
66. Halgamuge, M. N., Skafidas, E. & Davis, D. A meta-analysis of in vitro exposures to weak radiofrequency radiation exposure from mobile phones (1990–2015). *Environmental Research* **184**, 109227 (2020).
67. Ulrich, C. M., Demiris, G., Kennedy, R. & Rothwell, E. The ethics of sensor technology use in clinical research. *Nursing Outlook* **68**, 720–726 (2020).
68. Torrente-Rodríguez, R. M. *et al.* Investigation of cortisol dynamics in human sweat using a graphene-based wireless mhealth system. *Matter* **2**, 921–937 (2020).
69. Sedighi Maman, Z., Alamdar Yazdi, M. A., Cavuoto, L. A. & Megahed, F. M. A data-driven approach to modeling physical fatigue in the workplace using wearable sensors. *Applied Ergonomics* **65**, 515–529 (2017).
70. Wolf, S. M. *et al.* Managing incidental findings in human subjects research: analysis and recommendations. *The Journal of Law, Medicine & Ethics* **36**, 219–248 (2008).
71. Søraa, R. A. & Fosch-Villaronga, E. Exoskeletons for all: The interplay between exoskeletons, inclusion, gender, and intersectionality. *Paladyn, Journal of Behavioral Robotics* **11**, 217–227 (2020).
72. Colvonen, P. J., DeYoung, P. N., Bosompra, N.-O. A. & Owens, R. L. Limiting racial disparities and bias for wearable devices in health science research. *Sleep* **43**, (2020).
73. Digital Health Consumer Survey 2020 | Accenture. <https://www.accenture.com/us-en/insights/health/why-consumer-digital-health-adoption-stalling>.
74. Nebeker, C. *et al.* Ethical and regulatory challenges of research using pervasive sensing and other emerging technologies: IRB perspectives. *AJOB Empirical Bioethics* **8**, 266–276 (2017).
75. Piwek, L., Ellis, D. A., Andrews, S. & Joinson, A. The rise of consumer health wearables: promises and barriers. *PLOS Medicine* **13**, e1001953 (2016).

76. Lewis, D. Why many countries failed at COVID contact-tracing — but some got it right. *Nature* **588**, 384–387 (2020).
77. Kadam, R. A. Informed consent process: A step further towards making it meaningful! *Perspectives in Clinical Research* **8**, 107–112 (2017).
78. Al-Turjman, F. & Baali, I. Machine learning for wearable IoT-based applications: A survey. *Transactions on Emerging Telecommunications Technologies* **33**, e3635 (2022).
79. Mohr, D. C., Zhang, M. & Schueller, S. M. Personal sensing: understanding mental health using ubiquitous sensors and machine learning. *Annual Review of Clinical Psychology* **13**, 23–47 (2017).
80. De Arriba-Pérez, F., Caeiro-Rodríguez, M. & Santos-Gago, J. M. Collection and processing of data from wrist wearable devices in heterogeneous and multiple-user scenarios. *Sensors* **16**, 1538 (2016).
81. Fitbit Legal Privacy Policy. <https://www.fitbit.com/global/us/legal/privacy-policy>.
82. Berger, M. *et al.* Cortisol awakening response and acute stress reactivity in first nations people. *Scientific Reports* **7**, 41760 (2017).
83. Vythilingam, M. *et al.* Low early morning plasma cortisol in posttraumatic stress disorder is associated with co-morbid depression but not with enhanced glucocorticoid feedback inhibition. *Psychoneuroendocrinology* **35**, 442–450 (2010).
84. Sherman, B. M. & Korenman, S. G. Hormonal characteristics of the human menstrual cycle throughout reproductive life. *Journal of Clinical Investigation* **55**, 699–706 (1975).
85. Sonner, Z. *et al.* The microfluidics of the eccrine sweat gland, including biomarker partitioning, transport, and biosensing implications. *Biomicrofluidics* **9**, 031301 (2015).
86. De Meyer, T., Muyldermans, S. & Depicker, A. Nanobody-based products as research and diagnostic tools. *Trends in Biotechnology* **32**, 263–270 (2014).
87. Muyldermans, S. Nanobodies: Natural single-domain antibodies. *Annual Review of Biochemistry* **82**, 775–797 (2013).
88. Dumoulin, M. *et al.* Single-domain antibody fragments with high conformational stability. *Protein Science* **11**, 500–515 (2002).

89. Zhang, J. *et al.* Molecular recognition using corona phase complexes made of synthetic polymers adsorbed on carbon nanotubes. *Nature Nanotechnology* **8**, 959–968 (2013).